

# On the Kinetics of Materials of Geophysical Interest

Thesis by  
Matthew Gregory Newman

In Partial Fulfillment of the Requirements for the  
degree of  
Doctor of Philosophy

CALIFORNIA INSTITUTE OF TECHNOLOGY  
Pasadena, California

2018  
Defended August 31, 2017

© 2018

Matthew Gregory Newman  
ORCID: 0000-0003-2752-0121

All rights reserved

## ACKNOWLEDGEMENTS

I would like to express my sincere gratitude to the army of people who made this research effort possible. I begin by thanking the members of my thesis committee: Dan Meiron, Guruswami (Ravi) Ravichandran, Kaushik Bhattacharya, and Richard Kraus.

I owe a huge debt of gratitude to Richard Kraus for his daily advising. Rick has been a wonderful mentor and friend since I got into the dynamic compression field as an undergraduate student at Harvard. His unwaivering support throughout my Ph.D persisted on both the most mundane days of data analysis and the most intense days of experiments. Thank you for your sharing your scientific insights and expertise. I am a better scientist because of Rick's thoughtful advising. Thank you to both Rick and Alise Kraus (and their cat, Tuna) for your hospitality in hosting me during my time in Livermore.

I need to thank my academic advisor, Ravi, for his unwaivering support over the years. He has taught me many important lessons, not the least of which being that patience is a critical attribute of a scientist (and he possesses patience in spades). Thank you for your kindness and dedication to teaching.

Over the course of my Ph.D I was fortunate to work with many brilliant scientists. I would like to thank my collaborators from Caltech, Princeton, and Lawrence Livermore National Laboratory for their guidance: Paul Asimow for our rigorous discussions on thermodynamics; Zach Sternberger for his help with the radiation hydrodynamics code HYADES; Tom Duffy, June Wicks, and Sally Tracy for sharing their expertise in diffraction, high pressure experiments, and planetary science; Minta Akin and Joel Bernier for their support of the plate impact experiments; and Richard Kraus, Ray Smith, Jon Eggert, Federica Coppari, and many others in the high energy density group at LLNL for sharing their expertise in the hydrodynamic design of laser driven compression experiments, velocimetry analysis, and diffraction analysis.

The large-scale experiments I have performed would not have been possible without the help of numerous laboratory technicians at the Omega laser facility, Omega EP laser facility, and Dynamic Compression Sector. I would also like to acknowledge the hard work of the LLNL target fabrication team. In particular, I would like to thank Carol Davis, Jim Emig, and Eric Strang.

The Ravi/Kaushik group past and present has been a wonderful resource over the years. I have thoroughly enjoyed the glimpses into each of your research projects at our weekly meetings. It was a pleasure to work alongside each of you. Thank you for keeping me sane and thank you for your friendship.

Finally, I would like to acknowledge funding through the LLNL LDRD-15ERD012 and NLUF grant DE-NA0002720.

## ABSTRACT

Knowledge of the equation of state and phase diagram of magnesium silicates and light iron alloys is important for understanding the thermal evolution and interior structure of terrestrial planets. Dynamic compression techniques are the primary viable methods to create the temperature and pressure conditions that are relevant to Earth and super-Earth (1-10 Earth mass) sized planets. However, due to the kinetic constraints imposed by the timescale of dynamic compression experiments, the nature of the state within the dynamically compressed sample (whether equilibrium or metastable) is uncertain. Here, we present the results of a series of dynamic compression experiments performed on both laser driven compression and plate impact facilities to study the nanosecond to microsecond response of forsterite and iron silicide. In situ x-ray diffraction measurements are used to probe the crystal structure of solid phases and test for the presence of melt, from which we investigate the decomposition of forsterite and iron silicide into compositionally distinct phases at high pressure. For forsterite, we do not observe chemical segregation in the solid phase, however the presence of melt speeds up the kinetics and allows chemical segregation to occur on nanosecond timescales. For iron silicide, our results show a textured solid phase upon shock compression to pressures ranging from 166(14) to 282(24) GPa consistent with cubic and *hcp* structures in coexistence. Above 313(29) GPa, the intense and textured solid diffraction peaks give way to a diffuse scattering feature and loss of texture, consistent with melting along the Hugoniot.

## TABLE OF CONTENTS

Acknowledgements . . . . .	iii
Abstract . . . . .	v
Table of Contents . . . . .	vi
List of Illustrations . . . . .	vii
List of Tables . . . . .	xix
Chapter I: Introduction . . . . .	1
Chapter II: In situ observation of shock induced phase transitions in forsterite	5
2.1 Introduction . . . . .	5
2.2 Methods . . . . .	7
2.3 Results . . . . .	10
2.4 Conclusions . . . . .	12
Chapter III: Decomposition of Forsterite into MgO and Silica Rich Liquid on Nanosecond Timescales . . . . .	28
3.1 Introduction . . . . .	28
3.2 Methods . . . . .	30
3.3 Results . . . . .	34
3.4 Discussion . . . . .	36
3.5 Conclusions . . . . .	37
Chapter IV: Compression of Iron Silicide at Earth Core Conditions on Nanosecond Timescales . . . . .	62
4.1 Introduction . . . . .	62
4.2 Materials and Methods . . . . .	64
4.3 Results . . . . .	67
4.4 Discussion . . . . .	68
4.5 Conclusions . . . . .	70
Chapter V: Conclusions and Future Work . . . . .	85
Bibliography . . . . .	88

## LIST OF ILLUSTRATIONS

<i>Number</i>	<i>Page</i>
2.1 <b>Qualitative equilibrium phase diagram for the MgSiO<sub>3</sub>-MgO system.</b> This phase diagram shows that at all pressures above 23 GPa there are no thermodynamically stable single component crystal structures of forsterite composition. At the pressures and temperatures relevant to this study, forsterite will decompose to bridgmanite (Bd) and periclase (Pe) in equilibrium. . . . .	14
2.2 <b>A reconstructed computed tomography slice of a forsterite sample.</b> Computed tomographic analysis was conducted to determine the porosity of the forsterite samples and search for internal voids/cracks. The “deepest” crack approaches closer to the sample center than any other observed CT images. Samples were oriented in the DCS target chamber so that the x-ray beam path avoids cracks where possible. Voxel size is 6 $\mu\text{m}$ . . . . .	15
2.3 <b>Electron backscatter diffraction (EBSD) characterization of forsterite polycrystalline samples.</b> Electron backscatter diffraction was conducted to determine the grain size, orientation, and composition of a characteristic forsterite sample. Top: Grain map of forsterite sample indicating a characteristic grain size of $\sim 10 \mu\text{m}$ . All identified grains were indexed as forsterite, with no evidence of periclase or bridgmanite by comparing the observed diffraction pattern to the theoretical one for these structures. Bottom: Pole figure illustrating that the observed grain orientations are approximately random. . . . .	16
2.4 <b>Forsterite Hugoniot data used to determine the shock pressure and density.</b> Plot of the available data of the forsterite Hugoniot in pressure versus density space (top) and shock velocity versus particle velocity (bottom). For shot 084 (below 50 GPa) we used the linear $U_S$ -up relation $U_S = 6.43 + 1.06u_p$ and for shot 085 (above 50 GPa) we used $U_S = 6.46 + 0.905u_p$ to determine the shock state through impedance matching. This work attributes the change in density observed on the Hugoniot above 50 GPa to a phase transition from the forsterite structure to the metastable forsterite III structure. . . . .	17

- 2.5 **Timing of plate impact experiment.** Photon doppler velocimetry (PDV) lineouts of the true interface velocity between the forsterite sample and LiF window. The initial velocity plateau corresponds to shock breakout into the LiF window, while the subsequent velocity plateau corresponds to release to 0 pressure from the LiF free surface. The asterisks correspond to the timing of the x-ray source, indicating that in each experiment we observed one frame prior to shock breakout into the LiF window and one frame prior to release to 0 pressure. . . . . 18
- 2.6 **Beam configuration for in situ x-ray diffraction measurements.** The sample is rotated by  $28^\circ$  with respect to the beam normal so that the beam path does not probe laterally released states. The path of the beam penetrates the lexan sabot, LiF window, quartz driver, forsterite sample, and forsterite window. The driver and window materials are chosen to minimize x-ray attenuation. Diffracted x-rays are collected every 153.4 ns on an LSO scintillator coupled to a four frame imaging system. . . . . 19
- 2.7 **Diffraction data for shocked forsterite.** Diffraction data is de-warped into the diffraction coordinates  $2\theta$ - $\phi$ . The powder peaks correspond to diffraction from the shocked polycrystalline forsterite. The masked out regions (black) correspond to single-crystal like diffraction from the LiF window and do not represent diffraction from the forsterite sample. Top: diffraction pattern for forsterite shocked to 44.6(7.0) GPa. Bottom: diffraction pattern for forsterite shocked to 73.4(9.0) GPa. . . . . 20

- 2.8 **X-ray diffraction lineout for forsterite shocked to 44.6(7.0) GPa and released to 38.4(8.0) GPa.** Experimental lineout (red) compared to the theoretical lineout (black) for a mixture of shocked and released forsterite and forsterite III. The red blue and green data points indicate diffraction peaks for ambient forsterite, compressed forsterite, and compressed forsterite III respectively with a threshold of 10%. The lattice parameters for forsterite and forsterite III are determined by power law fit to the isothermal diamond anvil cell data. Therefore the theoretical diffraction assumes that temperature does not distort the ratios of the lattice parameters. The ratio of forsterite to forsterite III is determined to be 3 to 1 by fitting the theoretical lineout to the data to give the correct relative intensity of the (112) forsterite peak and the (131) forsterite III peak. . . . . 21
- 2.9 **X-ray diffraction lineout for forsterite shocked to 73.4(9.0) GPa and released to 66.16(10.0) GPa.** Progression of experimental lineouts (red) compared to the theoretical lineouts (black) of the forsterite III structure. The red and green data points indicate diffraction peaks for ambient forsterite and compressed forsterite III with a threshold of 10%. . . . . 22
- 2.10 **Comparison of observed diffraction to expected diffraction from periclase.** Diffraction from the periclase structure at the pressures and temperatures relevant to the forsterite Hugoniot are compared to the diffraction data observed in shot 084 frame 2 (bottom) and shot 085 frame 2 (top). The asterisks (bottom) correspond to diffraction peaks not already indexed as diffraction from shock compressed forsterite. . . . . 23
- 2.11 **Comparison of expected density to density inferred from the diffraction pattern.** The density of periclase, forsterite, and forsterite III are compared to the expected values based upon the previously measured forsterite Hugoniot and the 3000 K periclase isotherm from equations of state (Tange, Nishihara, and Tsuchiya, 2009; Wu et al., 2008). The density required to fit the periclase structure is well outside the uncertainty in the periclase isotherm while the forsterite structures are in good agreement with the Hugoniot density. . . . . 24

- 2.12 **Lineouts fit to the diffraction data for shot 084 frame 2 (top) and shot 085 frame 2 (bottom).** Lattice parameters were fit to the observed diffraction data (Table 2.3) using the Hugoniot density and ambient temperature crystal structure from Finkelstein as an initial guess. The resulting fits are slightly more dense than expected from the Hugoniot bulk density, but well within uncertainties ( $< 3\%$ ). . . . 25
- 3.1 Schematic illustration of the equilibrium phase boundaries in temperature versus composition space for a snapshot in pressure (De Koker, Karki, and Stixrude, 2013). For a forsterite composition, the sub-solidus phase assemblage is expected to be post-perovskite ( $\text{MgSiO}_3$ ) plus periclase (B1  $\text{MgO}$ ). Forsterite is believed to be silica poor relative to the eutectic composition, indicating a sub-liquidus phase assemblage of periclase plus silica-rich liquid. . . . . 39
- 3.2 **Experimental setup.** Top: Schematic diagram of the diffraction detector (PXRDIIP box) where x-rays are collected on image plates which line the sides of a  $5 \times 5 \times 7.5 \text{ cm}^3$  box. The solid red line shows the straight through x-ray path and the dashed line shows the path of x-rays scattered by the sample. The VISAR path is down range of the sample. Bottom: Schematic diagram of the target packages for shock and ramp experiments. The VISAR is incident upon the forsterite/LiF interface. A 75 or 150  $\mu\text{m}$  thick Ta pinhole with 300  $\mu\text{m}$  diameter aperture is used to collimate the x-rays and calibrate the detector geometry. . . . . 40

- 3.3 **Timing of shock compression experiment for shot 21922.** Top: representative laser pulse shape for the beams that drives the sample (left axis) and the beams that drive the x-ray backlighter (right axis). The ramping of intensity in the laser drive pulse shape compensates for adiabatic cooling due to expansion of the plasma plume which would otherwise generate a decaying shock. The steepening of the laser pulse relative to the ideal laser pulse shape (black) starting at 15 ns is responsible for the late time unsteadiness observed in the VISAR profile. Bottom: representative VISAR profile for shock compression experiments. The initial steady velocity plateau is used in the impedance match calculation to determine the shock pressure in the sample. The slight increase in particle velocity at 27 ns is confirmed by hydrodynamic simulations to be due to an inadvertent steepening in the laser pulse shape. The decrease in particle velocity at 28.5 ns is due to a release wave from the ablation surface. The axis range of the VISAR trace starts when the x-ray backlighter beams turn off to show relative timing. . . . . 41
- 3.4 **Characteristics Diagram for shock-ramp experiments.** Bottom: Characteristics plot showing the wave interactions for the shock-ramp experiments calculated using the radiation hydrodynamics code HYADES (Larsen and Lane, 1994). The complete target assembly of Be ablator, forsterite sample, and LiF window is simulated. Top: Wave interactions for just the forsterite region (enclosed in red). The x-ray source is timed to probe the forsterite after the ramp wave has transited the sample. . . . . 42

- 3.5 **Timing of ramp compression experiment for shot 24313.** Top: representative composite laser pulse for shock-ramp experiments. Three 10 ns laser beams are stacked sequentially in time to produce the composite shock and ramp pulse (left axis). The single 3-ns laser pulse that illuminates the Cu foil and thereby generates the x-ray source is plotted on the right axis. Bottom: Measured velocity at the interface between the forsterite sample and LiF window. The ramp wave enters the LiF at  $\sim 23.5$  ns and gradually ramps to the maximum velocity over a period of  $\sim 2.5$  ns, indicating shockless compression of the forsterite sample. The x-ray source is timed so that the sample is probed after the ramp wave has transited the sample. The decrease in velocity observed at 27 ns is due to release associated with laser turn off. . . . . 43
- 3.6 **Thermodynamic path for the shock-melt ramp-resolidification experiments.** The forsterite sample is first shocked to a point on the Hugoniot between the solidus and the liquidus, determined from single shock measurements (state 1). Subsequently, the sample partially releases at constant entropy into a LiF window, a process which further drives the sample towards the liquidus (state 2). Finally, the sample is shocklessly compressed back across the liquidus where it is probed with x-rays (state 3). . . . . 44
- 3.7 **Forsterite Hugoniot between 90 GPa and 140 GPa.** Selected  $U_S - u_p$  data for forsterite in the solid high pressure phase region (top) and the partial melt regime (bottom) (Mosenfelder, Asimow, and Ahrens, 2007; Jackson and Ahrens, 1979; Wett and Ahrens, 1983). To account for the large disparity in the errors associated with each data point, the data are linearly fit using a total least squares approach that includes uncertainties in both the particle and shock velocity (Krystek and Anton, 2007; Ruoff, 1967). The linear fits are used to infer the shock pressure in the sample from the LiF interface velocity through the standard impedance matching technique (Zeldovich and Raizer, 1965). . . . . 45

- 3.8 Diffraction data collected for shock compression to 125 GPa. The raw image files are dewarped into  $\phi - 2\theta$  space. Diffraction identified as coming from the shock sample is boxed in red. In each experiment, we observe three distinct Bragg peaks at  $64^\circ$  that correspond to crystal planes rotated  $33^\circ$  with respect to one another. This indicates that the microstructure induced by shock compression is consistent in each experiment and may suggest twinning. . . . . 46
- 3.9 The observed d-spacing is plotted as a function of Hugoniot pressure and compared to the expected diffraction peak positions for periclase at the relevant thermodynamic condition (Tange, Nishihara, and Tsuchiya, 2009; Wu et al., 2008). The line width denotes the relative intensity of the diffraction peaks; however due to the texture of the sample relative peak intensities or the absence of a diffraction peak cannot be used to rule out a structure. The peaks that we interpreted as solid diffraction from the shocked sample are plotted as red circles. The observed diffraction peaks do not match the expected peak location for periclase, and so we rule out periclase as a structure. 47
- 3.10 The observed d-spacing is plotted as a function of Hugoniot pressure and compared to the expected diffraction peaks for bridgmanite at the relevant thermodynamic condition (Tange, Kuwayama, et al., 2012; Fiquet, Andrault, et al., 1998; Fiquet, Dewaele, et al., 2000). Diffraction peaks are plotted if they fall above a threshold intensity of 25% (left) and 5% (right) of the most intense diffraction peak for the bridgmanite structure. The peaks interpreted as solid diffraction from the shocked sample are plotted as red circles. Diffraction is not expected at 2.2 and 125 GPa for the bridgmanite structure, so we rule it out as a candidate. . . . . 48
- 3.11 The observed d-spacing is plotted as a function of Hugoniot pressure and compared to the expected diffraction peaks for post-perovskite at the relevant thermodynamic condition Sakai, Dekura, and Hirao, 2016; Murakami et al., 2004. Diffraction peaks are plotted if they fall above a threshold intensity of 25% (left) and 5% (right) of the most intense diffraction peak for the post-perovskite structure. The peaks interpreted as solid diffraction from the shocked sample are plotted as red circles. Diffraction is not expected at 2.2 and 125 GPa for the post-perovskite structure, so we rule it out as a candidate. . . . . 48

- 3.12 **Diffraction data for partially molten forsterite.** Raw (top) and processed (bottom) diffraction data for forsterite shocked into the partial melt regime. In this Hugoniot region, we observe two features associated with diffraction from the forsterite sample; a sharp peak which we assign to periclase (red arrow) and a broad peak characteristic of diffuse scattering from a liquid (blue arrow). In this illustration, we show the raw diffraction data (top), a lineout of the de-warped diffraction data (middle), and the de-warped diffraction data (bottom). 49
- 3.13 Raw (top) and processed (bottom) diffraction data for shock compression to 214 GPa. The processed diffraction data has been dewarped in to  $\phi - 2\theta$  space and background subtracted. In this Hugoniot region, we only observe diffuse liquid scattering. . . . . 50
- 3.14 The observed d-spacing is plotted as a function of Hugoniot pressure and compared to the expected diffraction peaks for periclase at the relevant thermodynamic condition Fiquet, Andrault, et al., 1998; Fiquet, Dewaele, et al., 2000. The peaks interpreted as solid diffraction based on peak width are plotted as red circles. . . . . 51
- 3.15 The observed d-spacing is plotted as a function of Hugoniot pressure and compared to the expected diffraction peaks for post-perovskite at the relevant thermodynamic condition Sakai, Ohtani, et al., 2011; Murakami et al., 2004. While the peak we observe does match a diffraction peak of post-perovskite, we rule out this structure because under powder diffraction we do not observe any of the other post-perovskite peaks. . . . . 52
- 3.16 The observed d-spacing is plotted as a function of Hugoniot pressure and compared to the expected diffraction peaks for forsterite with a threshold intensity greater than 25% at the Hugoniot density. We rule out the forsterite structure because we do not observe the more intense forsterite peaks expected at roughly 2.1 and 1.5 . . . . . 53
- 3.17 The observed d-spacing is plotted as a function of Hugoniot pressure and compared to the expected diffraction peaks for forsterite III with a threshold intensity greater than 25% at the forsterite Hugoniot density (Finkelstein et al., 2014). We rule out the forsterite III structure because under powder diffraction we do not observe any of the most intense forsterite III diffraction peaks. . . . . 54

- 3.18 The observed d-spacing is plotted as a function of ramp pressure and compared to the expected diffraction peaks for periclase at the relevant thermodynamic condition. . . . . 55
- 3.19 Raw (top) and processed (bottom) diffraction data for ramp compression to 284(28) GPa. The processed diffraction data has been dewarped in to  $\phi - 2\theta$  space and background subtracted. Peaks indexed as periclase are indicated by blue arrows. . . . . 56
- 3.20 Plot of log grain diameter normalized by the lattice parameter of MgO as a function of log time (Syono, Goto, Takei, et al., 1981; H. Fei, 2013; De Koker, Stixrude, and Karki, 2008; Farver, Yund, and Rubie, 1994). The region shaded in red corresponds to grain sizes less than one lattice parameter of MgO and the region shaded in blue corresponds to the timescale of the experiments performed in this work. The black data points are lower bounds on the grain size for B1 MgO in the partial melt region of the Hugoniot calculated from the Scherrer equation. . . . . 57
- 4.1 **Timing of shock compression experiment.** Panel (a) shows a characteristic EP laser pulse shape from shot 22564 for the beam that drives the sample (left axis) and EP laser pulse shape for the beam which illuminates the Cu or Fe foil used as an x-ray source (right axis). The ramping of intensity in the laser drive pulse shape compensates for adiabatic cooling due to expansion of the plasma plume which would otherwise generate a decaying shock. Panel (b) shows a characteristic VISAR trace from shot 22564 for shock compression experiments. The wave velocity following shock breakout is used in the impedance match calculation to determine the shock pressure in the sample. The decrease in particle velocity at 12 ns is due to the laser shut off. The difference in velocity observed in VISAR 1 and VISAR 2 is consistent with the assumed phase uncertainty of 5%. The x-ray source laser (panel (a)) turns off prior to the shock releasing into the LiF (panel (b)) at 10 ns so that release states are not probed by x-rays. . . . . 74

- 4.2 **Electron Backscatter Diffraction (EBSD) characterization of the Fe-15Si starting material.** Grain map of a characteristic Fe-15Si sample indicating a grain size on the order of  $500 \mu\text{m}$ . The  $300 \mu\text{m}$  pinhole aperture is shown as a black circle (in an arbitrary location) for relative scale which indicates that the sample is highly textured under the pinhole aperture. . . . . 75
- 4.3 **Experimental setup and target geometry.** Top: Schematic diagram of the diffraction detector (PXRDIPO box) where x-rays are detected on image plates that line five sides of a  $5 \times 5 \times 7.5 \text{ cm}^3$  box. Solid red lines show the direct beam x-ray path and the dashed red line shows schematically the path of reflected x-rays from the shocked sample. The path of the VISAR laser is down range of the sample. Bottom: Schematic diagram of the target package consisting of an Fe-15Si foil sandwiched between a kapton ablator and LiF window held together by a thin ( $< 1 \mu\text{m}$  thick) layer of epoxy. The VISAR is incident upon the Fe-15Si/LiF interface. A  $150 \mu\text{m}$  thick W pinhole with  $300 \mu\text{m}$  diameter aperture is used to collimate the x-rays and calibrate the detector geometry. . . . . 76
- 4.4 **Iron Silicide Hugoniot Parameters.** Top: power law fit to the linear Hugoniot parameters (C and S) as a function of composition in weight percent. The fit was used to determine the Hugoniot parameters for iron silicide at 15 weight percent silicon. We assumed a 5% uncertainty in the fit parameters determined from the mean residual squared error of the power law fit. Bottom: linear fit to the ambient density as a function of composition in weight percent. The density measured in this work (plotted as an asterisk) shows good agreement to the power law fit to available data. . . . . 77

- 4.5 **X-ray diffraction patterns for solid samples.** Characteristic x-ray diffraction data for samples shocked into the solid Hugoniot regime. Each peak is attributed to either diffraction from the sample, W pinhole, Al layer, or LiF single-crystal like peaks. Top: Raw diffraction data for shot 81664. The peaks assigned to the *hcp* and *bcc* structures are indicated in red and blue respectively. The curves labeled with green, yellow, and red points correspond to powder diffraction from the W pinhole used to calibrate the detector geometry and de-warp the image into  $2\theta - \phi$  space. The diffraction signatures encircled in cyan come from LiF single-crystal like diffraction and indicated in green come from polycrystalline Al. Left: De-warped image plates. Right: Composite lineout showing the integrated  $\phi$  data as a function of d-spacing. The black correspond to individual lineouts taken over each individual diffraction peak and the red curve corresponds to the summation of each curve. . . . . 78
- 4.6 **X-ray Diffraction patterns for molten samples.** At 313(29) GPa we observe shock melting indicated by the loss of texture associated with crystallographic orientation and the onset of liquid diffuse scattering indicated in blue on the diffraction panels and lineout. Top: Raw diffraction data where the peaks encircled in cyan correspond to single crystal diffraction from the LiF window, the intense powder peaks correspond to diffraction from the W pinhole, and the diffuse signature corresponds to diffraction from the molten Fe-15Si. . . . . 79
- 4.7 **d-spacing versus pressure** Observed d-spacing versus pressure are plotted against their theoretical values for *hcp* with an ideal *c/a* ratio and ordered cubic structures at the Fe-15Si Hugoniot density. Relative expected peak intensities are indicated by line width. The in situ x-ray diffraction data are consistent with a cubic (plotted in black) and *hcp* (plotted in red) structure in coexistence from 166(14) GPa to 282(24) GPa. . . . . 80
- 4.8 **d-spacing versus pressure for  $\text{Ly}_\alpha$  and  $\text{He}_\alpha$  energies** Observed d-spacing versus pressure assuming that peaks previously indexed as *bcc* are actually  $\text{Ly}_\alpha$  diffraction from the  $(011)_{hcp}$  plane. . . . . 80

- 4.9 **Calculated Hugoniot temperatures for Fe-15Si.** Hugoniot temperatures for Fe-15Si calculated using a 3rd order Birch-Murnaghan equation of state and Debye and electronic model of the heat capacity (Fischer, Campbell, Caracas, Reaman, Heinz, et al., 2014; Brown and McQueen, 1986). The highest pressure where we observe solid diffraction and the lowest pressure where we observe only liquid scattering are 282(24) GPa and 313(29) GPa respectively. The upper bound corresponds to the limit where there is no latent heat associated with melting and no electronic contribution to the heat capacity. The lower bound includes a latent heat and electronic heat capacity taken to be equivalent to pure iron. We find that incipient melting observed at 282(24) GPa corresponds to melting point depression relative to the melting temperature of pure iron, which is expected due to entropy of mixing (Ma et al., 2004). The melt boundary from literature for Fe-16Si is plotted in solid black and extrapolation of the data to higher pressure is plotted as a dashed black line. . . . . 81

## LIST OF TABLES

<i>Number</i>	<i>Page</i>
2.1 <b>Shock States Achieved In Each Experiment.</b> Tabulation of the shock and release pressures and density determined from the measured interface velocity from PDV. The densities are used to compare theoretical diffraction from the forsterite and forsterite III structures to the observed diffraction pattern. . . . .	13
2.2 <b>Relative mass percent of states probed by x-rays.</b> Tabulation of the sample conditions determined from the x-ray probe time relative to shock breakout into LiF (column 2) and known shock velocities and sound speeds in forsterite (Duffy and Ahrens, 1992; Brown, Furnish, and Boness, 1987). X-rays timed before shock breakout probe both shocked and unshocked forsterite states, while x-rays timed after shock breakout probe both shock states and partially released states. . . . .	13
2.3 <b>Lattice parameters fit to the diffraction data.</b> Lattice parameters for the forsterite and forsterite III structures observed in shots 084 and 085 respectively. . . . .	13
3.1 <b>Shock States Achieved In Each Experiment.</b> Tabulation of the measured interface velocity from VISAR and the shock pressure from the impedance match calculation. The uncertainty in the interface velocity includes 5% uncertainty in VISAR phase, the uncertainty associated with wave unsteadiness, and the uncertainty in the velocity correction due to the LiF index of refraction. . . . .	38
3.2 Textured Diffraction Angles . . . . .	38
3.3 Relative Crystal Plane Angles . . . . .	39

- 4.1 **Summary of experimental data.** Tabulation of the laser drive energy, measured interface velocity from VISAR, the shock pressure from the impedance match calculation, and observed d-spacing for experiments on the omega extended pulse laser (EP) and the omega 60 beam laser ( $\omega$ ). The uncertainty in the interface velocity includes 5% uncertainty in VISAR phase as well as the uncertainty associated with wave unsteadiness. D-spacings are determined by Gaussian fit to lineouts of the de-warped image plates. Each peak was assigned to a crystal plane in either the *bcc* or *hcp* structure. Due to the texture of the sample, absence of a diffraction peak is not evidence for absence of the structure. The dominant source of error in the d-spacing is the uncertainty in the location along the pinhole from where the diffraction is occurring. This introduces an error of roughly  $0.1^\circ$  in the  $2\theta$  diffraction angle, which we use as our reported error (Rygg et al., 2012). . . . . 72
- 4.2 **Orientation relationship for *bcc* and *hcp* structures.** Tabulation of the textured diffraction data that indicates an orientation relationship between the *bcc* and *hcp* phases. Columns 2 and 3 denote the polar and azimuthal angles where diffraction from the  $(011)_{bcc}$  crystal plane was observed. Columns 4 and 5 denote the polar and azimuthal angles where diffraction from the  $(011)_{hcp}$  crystal plane was observed. Column 5 tabulates the calculated angle between the  $(011)_{bcc}$  and  $(011)_{hcp}$  crystal planes implied by the observed diffraction angles. The planes are nearly parallel, consistent with Burgers correspondence between *bcc* and *hcp* structures. . . . . 73

*Chapter 1*

## INTRODUCTION

Modeling the interior structure and thermal evolution of rocky planets requires knowledge of the equation of state and phase diagram of planetary materials at thermodynamic conditions that are relevant to planetary interiors and planetary formation processes. There has been wide interest in the multi-component melting behavior of magnesium silicates and iron alloys as model systems for understanding the dynamics of planetary mantles and cores, respectively (De Koker, Stixrude, and Karki, 2008; De Koker, Karki, and Stixrude, 2013; Adjaud, Steinle-Neumann, and Jahn, 2011).  $\text{Mg}_2\text{SiO}_4$  forsterite is close to the bulk silicate Earth composition and has been studied extensively at the conditions relevant to the Earth's mantle (De Koker, Stixrude, and Karki, 2008; Adjaud, Steinle-Neumann, and Jahn, 2011). Pure iron or iron-nickel alloys do not reproduce the density required by geophysical observations, and so an alloy of iron and silicon (iron silicide) has been considered as a potential candidate for the core composition (Birch, 1952; McDonough, 2003). Previous studies of  $\text{Mg}_2\text{SiO}_4$ , forsterite and iron silicides illuminate the interplay between thermodynamics and planetary processes.

Both forsterite and iron silicide exhibit complicated thermodynamic behavior as according to the Gibbs-Duhem relation, the number of phases that can exist in equilibrium increases with each material component in the system. For forsterite at the conditions relevant to the Earth's lower mantle, there is no stable solid structure with  $\text{Mg}_2\text{SiO}_4$  composition (De Koker, Karki, and Stixrude, 2013; Presnall et al., 1998). Achieving equilibrium at lower mantle conditions from an initially homogeneous forsterite composition necessarily requires decomposition into the sub-solidus phase assemblage of periclase ( $\text{MgO}$ ) and perovskite ( $\text{MgSiO}_3$ ) or the sub-liquidus phase assemblage of periclase and silica rich liquid. This phase separation is potentially important, as the density contrast between periclase and liquid phases induced by phase separation in magnesium silicates could drive chemical stratification of planetary mantles during magma ocean crystallization (Solomatov, 2007).

Similarly, for iron silicides at core conditions, silicon is insoluble with iron and no stable structure with silicon composition greater than 7.9% has been observed (Fischer, Campbell, Reaman, et al., 2013; Fischer, Campbell, Caracas, et al., 2014;

Lin et al., 2002; Lin, 2009). Light element rejection (incongruent melting) upon solidification at the inner core boundary has been hypothesized to contribute to the buoyant instability responsible for convection of the Earth's outer core which in turn generates the Earth's magnetosphere. Therefore, for both forsterite and iron silicide, achieving equilibrium at the extreme pressures and temperatures relevant to planetary interiors requires the creation of heterogeneous domains from the originally homogeneous material, a process we refer to as chemical segregation.

For most single component systems, the kinetics associated with phase transitions have been attributed to the timescale for homogeneous nucleation (S.-N Luo and Ahrens, 2004). Single-component transitions may occur rapidly through pathways to equilibrium which only require local deformation of the material (Hennig, 2005). In contrast, for multi-component systems that may chemically segregate, the kinetics may be controlled by the ionic diffusivity of the homogeneous solution from which the heterogeneous domains are precipitated (Porter, Easterling, and Sherif, 2009). Given this constraint, the equilibrium phase diagram does not give the complete physical picture for materials that may phase segregate. For example, under 300 K compression of forsterite to 90 GPa, a series of compounds with  $\text{Mg}_2\text{SiO}_4$  composition have been shown to remain metastable well into the region where chemical segregation should occur (Finkelstein et al., 2014).

Historically, dynamic compression techniques have been used to probe the pressure and temperature conditions deep within the Earth and other planets (Jackson and Ahrens, 1979; Wett and Ahrens, 1983; Mosenfelder, Asimow, and Ahrens, 2007; Lyzenga and Ahrens, 1980; S-N Luo, Akins, and Asimow, 2004; Brown, Furnish, and Boness, 1987; Brown and McQueen, 1986). However, for the study of multi-component materials, it is important to consider the fact that we are using nanosecond to microsecond timescale experiments to infer the behavior of natural processes that occur over the thousand year timescale. Broadly, dynamic compression techniques come in two flavors: uniaxial plate impact and laser driven compression. In plate impact experiments, the pressure state of the sample is induced by impact with a projectile. The ultimate pressure achieved is limited by the impedance and velocity of the projectile. The two stage light-gas gun at the Dynamic Compression Sector is capable of launching projectiles up to  $6 \text{ km s}^{-1}$  generating pressures on the order of hundreds of GPa. The amount of time that the sample is subjected to the shock state is limited by the thickness of the sample, which in turn is limited by the time it takes for free surface waves to release the sample to ambient pressure. A typical

timescale for plate impact induced compression may range from  $10^2$  ns to  $10^3$  ns.

In laser driven compression experiments, the sample pressure is limited by the intensity of the laser beam and the efficiency with which laser energy can be converted to pressure in the ablation plasma. At the Omega laser facility, lasers can be used to generate pressures in excess of 1 TPa. However, the duration of the experiment is limited by the pulse duration of the laser which may range from roughly 1 ns to 10 ns.

Historically, material response under dynamic compression has been probed using measurements of the wave profile or wave speeds. However, recently, in-situ x-ray diffraction measurements have started to become more common in dynamic compression science. Powder X-ray diffraction measurements provide a method to record the high-pressure phase or phases of the compressed material. Solid structures are readily identified through comparison of the observed diffraction pattern to candidate crystal structures. Liquid phases may be inferred from loss of texture associated with crystallographic orientation and onset of diffuse scattering attributed to the loss of the strict order of a crystalline solid.

Combined, plate impact and laser platforms allow us to probe material response across three orders of magnitude in both pressure and time. To our knowledge, prior to this work, there have been no direct investigations into the kinetics of chemical segregation at high pressures and temperatures.

For solid-solid phase transitions, chemical segregation will be kinetically limited by solid state diffusion, which may occur as volume diffusion or as diffusion along grain boundaries. In chapter 1, we present the results of uniaxial plate impact experiments, where my collaborators and I used in situ x-ray diffraction measurements to determine the microsecond response of forsterite shocked to pressures of up to 75 GPa. These measurements demonstrate the persistence of metastable forsterite compounds at the elevated temperatures and pressures on the forsterite Hugoniot and thereby bound the solid state diffusivity of  $\text{Mg}_2\text{SiO}_4$  as the equilibrium phase assemblage does not nucleate on the microsecond timescale of these experiments.

For materials dynamically compressed to a partially molten state, the path to equilibrium may proceed more rapidly. In chapter 2, we present the results of laser driven dynamic compression experiments on forsterite driven into the partially molten regime. Results demonstrate that by progressing from the liquid state to the solid state, dynamic experiments may be used to probe equilibrium properties even in

materials that chemically segregate.

In chapter 3, we discuss the results of a series of laser driven shock compression experiments on an iron silicide alloy with 15 weight percent silicon. Iron silicide alloys of varying composition have been studied extensively in uni-axial plate impact experiments, but these results show the first in situ measurement of the crystal structure and melting upon shock loading (Matassov, 1977; Funtikov, 2007; Balchan and Cowan, 1966; Kormer and Funtikov, 1965). Motivated by the results of this initial effort, we suggest future experiments and diagnostic developments that would be valuable for measuring chemical segregation and incongruent melting in dynamic experiments.

## IN SITU OBSERVATION OF SHOCK INDUCED PHASE TRANSITIONS IN FORSTERITE

### 2.1 Introduction

Knowledge of the equation of state and phase diagram of the MgO-MgSiO<sub>3</sub> thermodynamic system is important for modeling the interior structure and dynamics of the Earth's mantle (Asimow, 2017; Y. Fei et al., 2004). Mg<sub>2</sub>SiO<sub>4</sub> forsterite has been studied extensively by the high pressure community over a wide range of thermodynamic conditions to understand partial melting and potential chemical stratification of the mantle (Adjaud, Steinle-Neumann, and Jahn, 2011; De Koker, Stixrude, and Karki, 2008). Figure 2.1 shows that at the pressures relevant to the Earth's lower mantle, there is no stable compound with composition Mg<sub>2</sub>SiO<sub>4</sub>. Achieving an equilibrium state from an initially homogeneous forsterite crystal necessarily involves decomposition into at least two compounds with different composition and hence creation of heterogeneous domains from the originally homogeneous material, a process that we refer to as chemical segregation.

Chemical segregation in magnesium silicates is well established by heated static high pressure experiments and further supported by first-principles calculations. First-principles molecular dynamics simulations support chemical segregation of forsterite into a sub-solidus phase assemblage of periclase and bridgmanite (De Koker, Karki, and Stixrude, 2013). As a single component, the bridgmanite structure is stable to 125 GPa, where a phase change to a post-perovskite phase (CaIrO<sub>3</sub> structure) occurs (Murakami et al., 2004; Oganov and Ono, 2004). Similarly, the periclase structure remains stable to 600 GPa, where a phase change from the B1 structure to the B2 structure occurs (Coppari et al., 2013). Chemical segregation in Mg<sub>2</sub>SiO<sub>4</sub> has been observed at pressures above 23 GPa from detailed equilibrium experiments in heated multi-anvil presses (Presnall et al., 1998). However, under 300 K compression, a series of compounds with Mg<sub>2</sub>SiO<sub>4</sub> composition have been shown

---

This chapter is in preparation for submission with Minta C. Akin, Joel V. Bernier, Richard G. Kraus, Paul D. Asimow, Jed L. Mosenfelder, Amanda Dillman, Sally Lee, Barbara Lavina, Darren C. Pagan, Ryan Crum, and Jonathan Lind.

to remain metastable to 90 GPa, well into the region where chemical segregation to the equilibrium phase assemblage is expected to occur (Finkelstein et al., 2014).

Uniaxial plate impact experiments provide a platform to measure the high-pressure and high-temperature equation of state of materials. Therefore, plate impact experiments facilitate the study of geologic materials at the elevated pressures and temperatures that are directly relevant to the conditions in the Earth's lower mantle. Previous experiments have delineated several phase regions on the forsterite Hugoniot on the basis of density variations, sound speed measurements, and shock temperature measurements (Mosenfelder, Asimow, and Ahrens, 2007; Lyzenga and Ahrens, 1980; Brown, Furnish, and Boness, 1987); however, no direct in situ observations of the phase or phases behind the shock front have been made. Therefore, the nature of the state behind the shock front (metastable or equilibrium) remains unidentified. This question is particularly pertinent to forsterite, where access to the equilibrium phase assemblage may be kinetically inhibited due to the timescale required for chemical separation, which is limited by the ionic diffusivity of the solid solution from which the equilibrium phase assemblage is precipitated. To nucleate nanometer sized grains (the smallest grains that may reasonably be called stable (Hawreliak et al., 2007; Gleason et al., 2015)) on the characteristic microsecond timescale of plate impact experiments would require an ionic diffusivity of  $1 \text{ nm}^2 \mu\text{s}^{-1}$ , which is 5 orders of magnitude larger than the ionic diffusivity expected for bulk solid forsterite (H. Fei, 2013). Therefore, a reconstructive phase transformation is unlikely on the basis of volume diffusion under experimental shock conditions. However, crystallization of the equilibrium phase assemblage may be possible from other mechanisms such as diffusion along grain boundaries (where the diffusivity may be as much as 9 orders of magnitude larger than the volume diffusion) or liquid diffusion activated by localized melting (De Koker, Stixrude, and Karki, 2008; H. Fei, 2013).

Shock recovery experiments, which look for signatures of the shock state in samples recovered to ambient conditions, show disparate results. Samples shocked to 78 GPa and recovered at ambient conditions by Syono et al. suggest that the nature of the so called "Mixed-Phase" Hugoniot region between 50 GPa and 120 GPa is incomplete transformation to the equilibrium periclase and bridgmanite phase assemblage supported by transmission electron microscopic observation of periclase and  $\text{MgSiO}_3$  glass (Syono, Goto, Takei, et al., 1981). In contrast, recovery of samples shocked to pressures up to 75 GPa by Jeanloz, 1980 show no reconstructive phase

transition (Jeanloz, 1980).

In this paper, we present in situ powder x-ray diffraction observations of the crystal structure of forsterite samples shocked to 44.6(6) GPa and 73.4(7) GPa. Our results demonstrate that chemical segregation of forsterite does not occur on dynamic experimental timescales but rather highly non-equilibrium states persist to 73.4(7) GPa on the forsterite Hugoniot.

## 2.2 Methods

### Sample Synthesis and Characterization

The forsterite samples were synthesized by hot pressing finely grained forsterite powder at temperatures between 1200 °C and 1250 °C and a nominal pressure of 3 GPa (Mosenfelder, Deligne, et al., 2006; Mosenfelder, Asimow, and Ahrens, 2007). The resulting forsterite polycrystalline rod had nearly zero porosity as determined from computed tomography measurements indicating a bulk density very near the crystal density of 3.227 g cc<sup>-1</sup>. The forsterite rod was cut into 5 discs of approximate 2 mm thickness and polished flat.

To quantify the amount of cracking that occurred as a result of the synthesis process, four of the five cut samples were characterized at GSECARS (sector 13) at the Advanced Photon Source, Argonne National Lab (APS). High resolution images (Figure 2.2) were collected for computed tomographic analysis to determine the presence of internal void space, with a voxel size of 6 μm. Internal cracks were observed near the edges of three of the four samples, with the deepest crack approximately 2 mm from the edge. The forsterite samples were oriented in the chamber at the Dynamic Compression Sector (DCS) of APS so that the cracks were not in the path of the x-ray beam.

To quantify the composition and distribution of grain size and orientation, a characteristic forsterite sample was analyzed by electron backscatter diffraction (EBSD). The measurements show polycrystalline forsterite composed of randomly oriented grains with an approximate mean grain size of 10 μm as shown in Figure 2.3. All indexed grains were identified as forsterite by comparing the observed diffraction pattern to the theoretical one for forsterite, with no evidence of periclase or bridgmanite in the forsterite samples. Scaling the volume of the forsterite sample by the approximate grain volume suggests each forsterite sample is composed of on the order of 10<sup>8</sup> randomly oriented grains. Static x-ray diffraction images of the ambient forsterite taken under the quasi-monochromatic x-ray source further demon-

strate that there were no strongly preferred grain orientations in the samples and no measurable amount of periclase in the starting material. To quantify the amount of periclase that may be in the ambient forsterite sample, we take the lowest intensity observed forsterite peak as a bound on the resolution of the diffraction diagnostic. This methodology implies that the starting sample is composed of less than 0.05 volume percent periclase as the quantity of periclase where the most intense periclase diffraction peak is expected to be less intense than the diffraction threshold.

### **Experimental Geometry**

The nominal target assembly consisted of a 2 mm thick forsterite sample sandwiched between a 100  $\mu\text{m}$  thick quartz driver plate and 1 mm lithium fluoride (LiF) window. The downstream face of the forsterite sample is coated with 150 nm of Al to improve reflectivity for velocimetry measurements. The LiF window is used because it is well impedance matched to forsterite and therefore generates a shallow release from the shock state. This is important so that the range of pressures probed by x-rays once the shock exits the sample is minimized.

The targets were impacted by a 4 mm thick LiF single crystal flyer plate mounted in a Lexan sabot. Single crystal LiF was used as a flyer since it is low-Z (to avoid x-ray attenuation) and the single crystal LiF diffraction signature will be easy to separate from the polycrystalline forsterite diffraction signature. The sabot was launched by the two-stage light gas gun at DCS (12.5 mm bore diameter) that is capable of generating projectile velocities up to 6 km s<sup>-1</sup>.

### **Pressure Determination**

Photon Doppler Velocimetry (PDV) was used to monitor the flyer velocity as well as the particle velocity at the interface between the forsterite sample and LiF window. The PDV system records the beat frequency of time averaged light intensity which is related to the surface velocity of the reflector (Strand et al., 2006). The apparent particle velocity in the LiF was converted to the true interface velocity using the measured index of refraction for LiF (Rigg et al., 2014). The pressure in the shock state was determined through the standard impedance matching technique using the known Hugoniot of forsterite (Figure 2.4) and LiF (Mosenfelder, Asimow, and Ahrens, 2007; Rigg et al., 2014; Jackson and Ahrens, 1979; Wett and Ahrens, 1983; Syono, Goto, Sato, et al., 1981; Marsh, 1980). PDV lineouts of the forsterite/LiF interface velocity corrected for the index of refraction of LiF are shown in Figure 2.5 and the pressure states achieved in each experiment are tabulated in Table 2.1.

### **In Situ X-ray Diffraction**

A narrow-band ( $\sim 0.01\%$  Bandwidth) 23 keV light source is used for precision powder x-ray diffraction measurements. The quasi-monochromatic source generates single-pulse x-ray diffraction images of 100 ps duration. Diffracted photons are detected on an LSO (lutetium oxyorthosilicate) scintillator coupled to four PIMAX cameras capable of recording four frames with an interframe spacing of 153.4 ns per plate impact experiment.

The experimental setup used to collect diffraction images is shown in Figure 2.6. The axis of the gun was rotated by  $28^\circ$  relative to the normal of the x-ray beam, such that the path of the beam penetrates the target assembly at  $62^\circ$ . The angle of the gun axis with respect to the x-ray beam is chosen so that as the sample accelerates along the gun axis, the path of the beam stays ahead of lateral release waves. Therefore, laterally released states in the forsterite are not probed by diffraction. As the x-ray beam path penetrates the flyer, it must be composed of low-Z materials, which inherently limits the pressures that can be induced by plate impact.

Prior to each plate impact experiment, polycrystalline Si was placed in the DCS target chamber and used to calibrate the precise detector geometry. The Si calibration is used to de-warp the diffraction data from raw spatial coordinates into the diffraction coordinates,  $\phi$  versus  $2\theta$ , where polycrystalline diffraction data project onto lines of constant  $2\theta$ . Contour images of the diffraction pattern are integrated with respect to  $\phi$  to produce diffraction lineouts (intensity as a function of  $2\theta$ ). Intense single-crystal like diffraction peaks associated with diffraction from the single crystal LiF window are masked out of the contour image so that they are not integrated into the diffraction lineout.

For diffraction images of the forsterite sample, the Si calibration is corrected to account for the change in apparent sample-to-detector distance caused by the finite sample thickness. A diffraction image of the ambient forsterite poly-crystal is used to approximate the uncertainty in the  $2\theta$  diffraction angle by comparing the observed forsterite diffraction angles to the theoretical diffraction angles. The calculated residual squared error implies uncertainties in the  $2\theta$  diffraction angle of 1%. The calibration for driven forsterite samples is further corrected to account for movement of the sample center of mass along the gun axis using the known particle velocity in the shock state.

To determine the thermodynamic state of the sample during each pulse of the x-ray source, the timing of the synchrotron relative to the observation of shock breakout

into the LiF is recorded on an oscilloscope (additional timing corrections are applied to account for known system delays). In both shots, the first frame was observed prior to breakout into the LiF so that a portion of the sample was shocked and the remainder unshocked. The proportion (by mass) of shocked and unshocked material was calculated using the known shock velocity and sample thickness. The second frame was observed after breakout into the LiF, so that a portion of the sample was shocked and the remainder partially released into LiF. The proportion of shocked and partially released material was calculated using the sound velocity in forsterite, sample thickness, and Hugoniot compression (Brown, Furnish, and Boness, 1987; Duffy and Ahrens, 1992). The sample states probed during the first two x-ray pulses are tabulated in Table 2.2.

### 2.3 Results

Full density polycrystalline forsterite was shock compressed to pressures of 44.6(6) GPa and 73.4(7) GPa. At 44.6(6) GPa we recorded two diffraction images prior to release to ambient pressure, which showed diffraction peaks consistent with forsterite compressed to the Hugoniot density. The processed diffraction image for frame 2 (where the sample was predominantly in the shock state) are shown in Figure 2.7. Figure 2.8 shows the progression of the observed diffraction, where each frame is separated in time by 153.4 ns. The observed lineouts are compared to the theoretical lineouts for the mixture of crystal structures and thermodynamic states that are presumed to exist in each frame. Lattice parameters for the forsterite and forsterite III structures are taken from power law fit to the 300 K isothermal data to determine the lattice parameter as a function of volume (Finkelstein et al., 2014). Two peaks not identified as compressed forsterite are indexed as diffraction from the (131) and (132) planes of the forsterite III structure. The density of the forsterite III structure inferred from the diffraction peaks is roughly 10 percent more dense than the forsterite structure, consistent with previous observations of the equation of state of forsterite and forsterite III (Finkelstein et al., 2014). Matching the relative intensity of the (112) forsterite peak and (131) forsterite III peak would suggest a mixture of 3 parts forsterite to 1 part forsterite III. Therefore, the error we make by using the Hugoniot density to index the forsterite diffraction peaks is small (on the order of 2%) since the mixture is composed mostly of forsterite.

Upon shock compression to 74.8 GPa, we observed diffraction consistent with complete transformation to the forsterite III structure, which suggests that the nature of the mixed phase region corresponds to a diffusion free phase transition to Forsterite

III. Figure 2.7 shows the processed diffraction data for frame 2 and 2.9 shows the progression of the observed diffraction lineouts compared to the theoretical diffraction from the forsterite III structure at the relevant density.

A comparison of the observed diffraction to the expected diffraction for periclase is shown in Figure 2.10. We fit lattice parameters to the observed diffraction peaks using the Hugoniot density as an initial guess for the forsterite structures and the periclase 3000 K isotherm as an initial guess for periclase. The 3000 K isotherm was chosen as that represents a reasonable estimate of the temperature on the forsterite Hugoniot at these pressures based upon the available data (Luo, Akins, and Asimow, 2004; De Koker and Stixrude, 2009). The resultant densities showed good agreement (<3% error) to the forsterite structures and poor agreement to periclase (>15% error) as shown in Figure 2.11. The lineouts fit to the forsterite structure are plotted in Figure 2.12 and the lattice parameters are tabulated in Table 2.3.

Our results show that the previously described “low pressure” Hugoniot regime corresponds to compression of the forsterite lattice and that the nature of the density collapse at 50 GPa is a deformational phase change to the metastable forsterite III structure. The deformation seems to correspond to stretches of the principle a, b, and c forsterite lattice parameters by  $\frac{1}{2}$ , 2, and 1 to produce the forsterite III c, a, and b lattice parameters accompanied by a volume collapse of  $\sim 10\%$ . We do not observe the equilibrium phase assemblage of periclase and bridgmanite in the diffraction pattern, consistent with the shock recovery results of Jeanloz et al., 1980 but in disagreement with the recovery experiments of Syono et al., 1981. This suggests that MgO crystallization may not have occurred in the shock state or that additional heat was generated due to the geometry of the recovery capsule speeding up diffusion.

Our result confirms that crystallization of periclase is not feasible under the microsecond timescales of the experiment, which provides insight into the nature of the shock state. First, this indicates localized melting is not activated by the shock process at these pressures as periclase would readily nucleate based on reasonable liquid diffusivities (De Koker, Stixrude, and Karki, 2008). Second, this work bounds the grain boundary diffusivity of forsterite below  $1 \text{ nm}^2 \mu\text{s}^{-1}$  at the elevated pressures and temperatures probed in these experiments.

## 2.4 Conclusions

This work provides the first in situ observation of forsterite under uniaxial plate impact conditions. We found that solid state decomposition into the equilibrium phase assemblage (periclase and bridgmanite) is not possible under the kinetic constraints imposed by the experiment, but rather metastable structures persist at the elevated Hugoniot pressures and temperatures. The structures that we observed are in good agreement with the structures observed at ambient temperature in diamond anvil cells (Finkelstein et al., 2014). Absence of the periclase structure suggests that localized melting does not occur in the material processed by the shock and that the grain boundary diffusivity of forsterite at these conditions is less than previously theorized based on extrapolations from data at lower pressure (H. Fei, 2013). Future work observing the crystal structure or structures of forsterite in situ at higher pressure would be valuable to determine the nature of the density change along the Hugoniot observed at 120 GPa.

Plate impact experiments provide a platform to observe the properties of geological materials at the pressure and temperatures that are relevant to the deep interior of the Earth. However, the results of this paper illustrate that kinetics and not equilibrium can dictate the observed equation of state and material properties on microsecond timescales for multi-component systems that may phase segregate.

Shot	$P_{\text{Shock}}$ (GPa)	$\rho_{\text{Shock}}$ ( $\text{g cm}^{-3}$ )	$P_{\text{Release}}$ (GPa)	$\rho_{\text{Release}}$ ( $\text{g cm}^{-3}$ )
084	44.6(7.0)	4.06(0.2)	38.4(8.0)	3.96(0.4)
085	73.4(9.0)	4.57(0.2)	66.2(10.0)	4.46(0.4)

Table 2.1: **Shock States Achieved In Each Experiment.** Tabulation of the shock and release pressures and density determined from the measured interface velocity from PDV. The densities are used to compare theoretical diffraction from the forsterite and forsterite III structures to the observed diffraction pattern.

Shot	X-ray time (ns)	Ambient Fo	Shocked Fo	Partially Released Fo
084	-103.6	64.4	35.6	0
084	49.8	0	76.8	23.2
085	-128.9	44.8	55.2	0
085	24.5	0	53.9	46.1

Table 2.2: **Relative mass percent of states probed by x-rays.** Tabulation of the sample conditions determined from the x-ray probe time relative to shock breakout into LiF (column 2) and known shock velocities and sound speeds in forsterite (Duffy and Ahrens, 1992; Brown, Furnish, and Boness, 1987). X-rays timed before shock breakout probe both shocked and unshocked forsterite states, while x-rays timed after shock breakout probe both shock states and partially released states.

Shot	Structure	a	b	c	V
084	Fo	4.4917	9.0967	5.5875	228.30
085	Fo III	2.6415	8.5829	8.7457	198.28

Table 2.3: **Lattice parameters fit to the diffraction data.** Lattice parameters for the forsterite and forsterite III structures observed in shots 084 and 085 respectively.

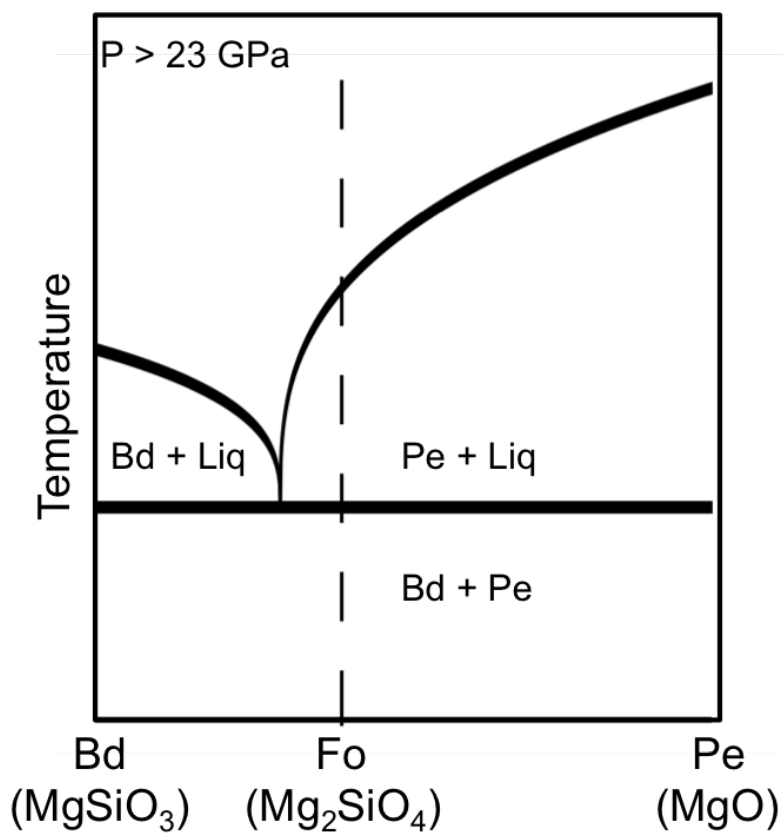


Figure 2.1: **Qualitative equilibrium phase diagram for the  $\text{MgSiO}_3$ - $\text{MgO}$  system.** This phase diagram shows that at all pressures above 23 GPa there are no thermodynamically stable single component crystal structures of forsterite composition. At the pressures and temperatures relevant to this study, forsterite will decompose to bridgmanite (Bd) and periclase (Pe) in equilibrium.

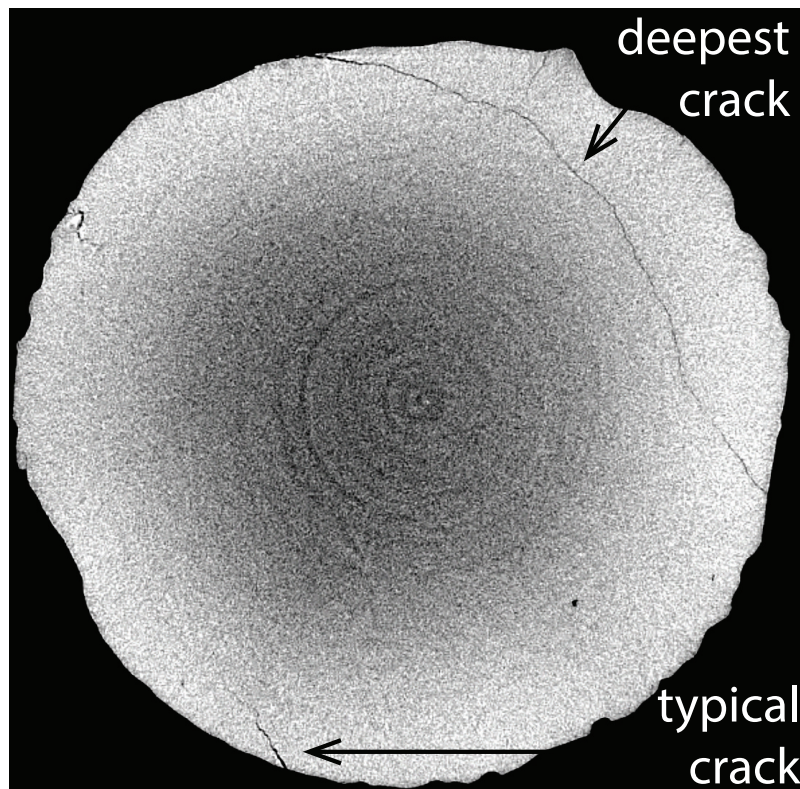


Figure 2.2: **A reconstructed computed tomography slice of a forsterite sample.** Computed tomographic analysis was conducted to determine the porosity of the forsterite samples and search for internal voids/cracks. The “deepest” crack approaches closer to the sample center than any other observed CT images. Samples were oriented in the DCS target chamber so that the x-ray beam path avoids cracks where possible. Voxel size is  $6\ \mu\text{m}$ .

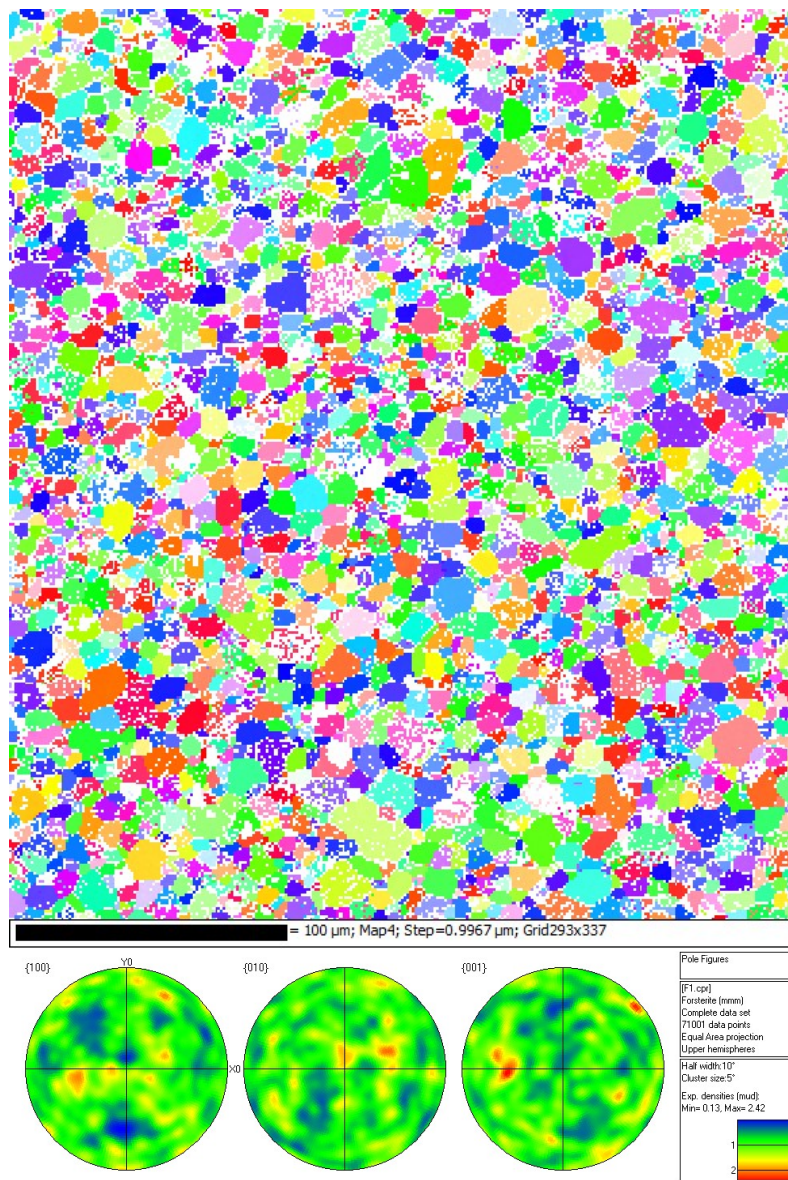


Figure 2.3: **Electron backscatter diffraction (EBSD) characterization of forsterite polycrystalline samples.** Electron backscatter diffraction was conducted to determine the grain size, orientation, and composition of a characteristic forsterite sample. Top: Grain map of forsterite sample indicating a characteristic grain size of  $\sim 10 \mu\text{m}$ . All identified grains were indexed as forsterite, with no evidence of periclase or bridgmanite by comparing the observed diffraction pattern to the theoretical one for these structures. Bottom: Pole figure illustrating that the observed grain orientations are approximately random.

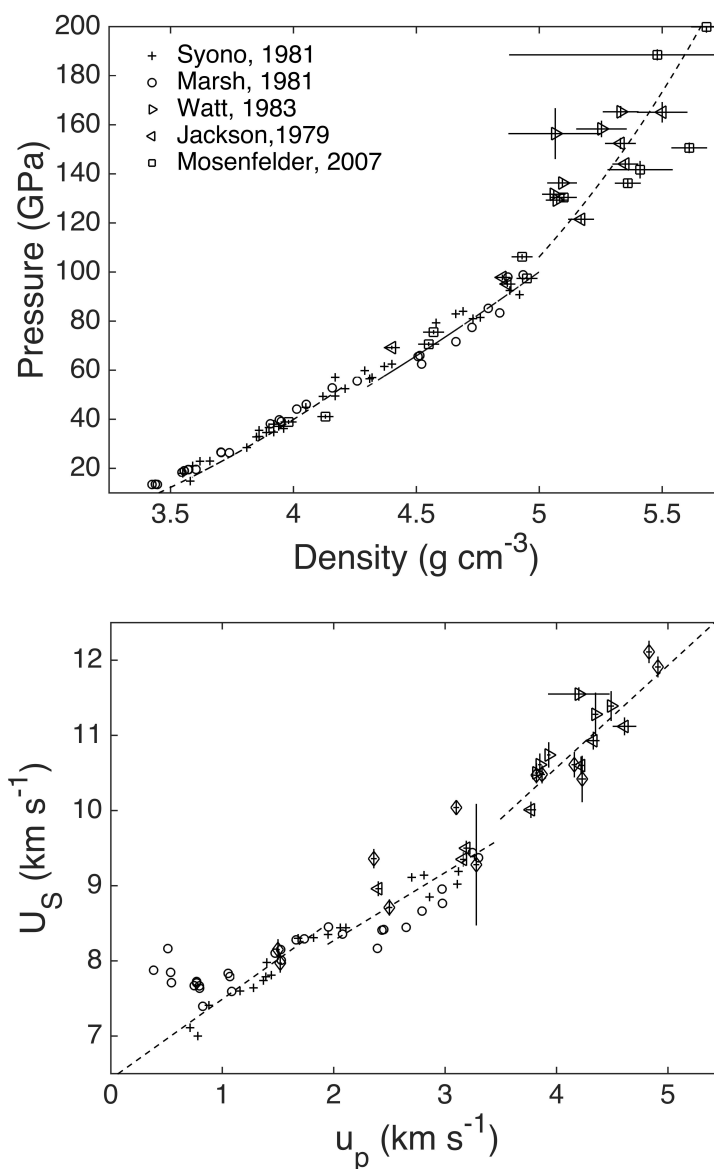


Figure 2.4: **Forsterite Hugoniot data used to determine the shock pressure and density.** Plot of the available data of the forsterite Hugoniot in pressure versus density space (top) and shock velocity versus particle velocity (bottom). For shot 084 (below 50 GPa) we used the linear  $U_S$ -up relation  $U_S = 6.43 + 1.06u_p$  and for shot 085 (above 50 GPa) we used  $U_S = 6.46 + 0.905u_p$  to determine the shock state through impedance matching. This work attributes the change in density observed on the Hugoniot above 50 GPa to a phase transition from the forsterite structure to the metastable forsterite III structure.

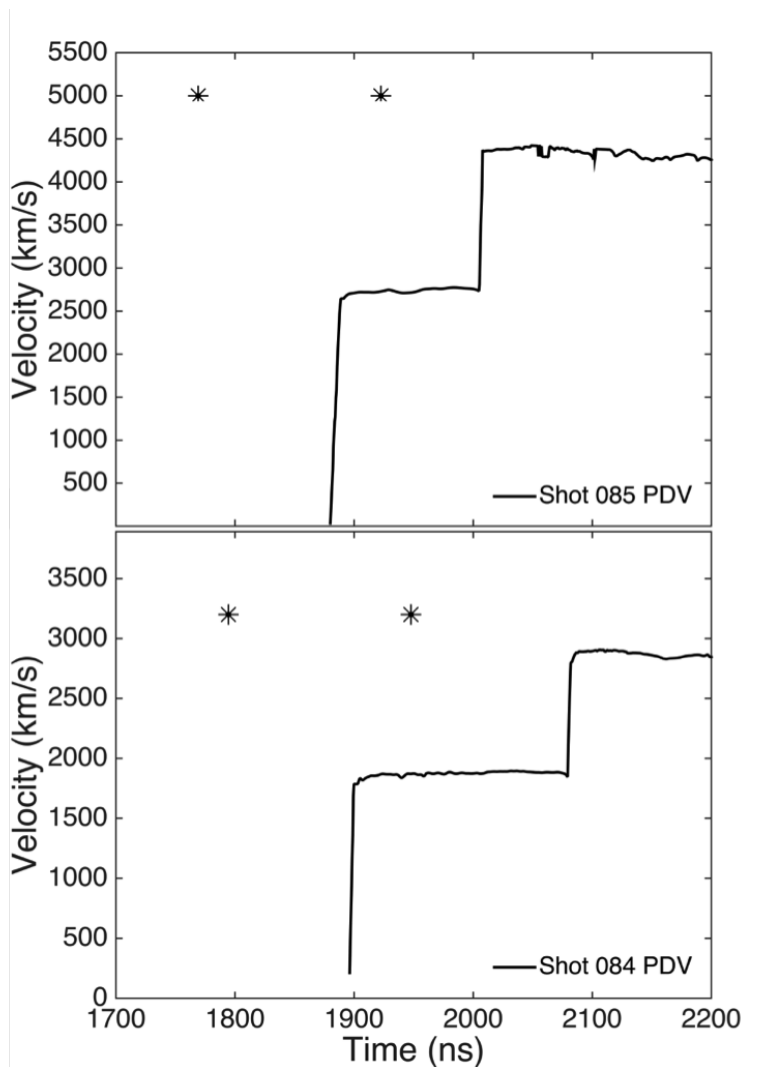


Figure 2.5: **Timing of plate impact experiment.** Photon doppler velocimetry (PDV) lineouts of the true interface velocity between the forsterite sample and LiF window. The initial velocity plateau corresponds to shock breakout into the LiF window, while the subsequent velocity plateau corresponds to release to 0 pressure from the LiF free surface. The asterisks correspond to the timing of the x-ray source, indicating that in each experiment we observed one frame prior to shock breakout into the LiF window and one frame prior to release to 0 pressure.

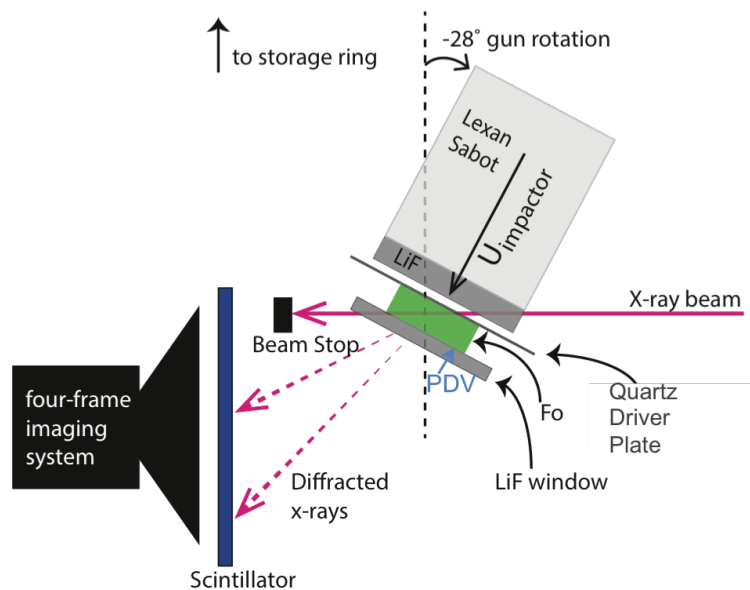


Figure 2.6: **Beam configuration for in situ x-ray diffraction measurements.** The sample is rotated by  $28^\circ$  with respect to the beam normal so that the beam path does not probe laterally released states. The path of the beam penetrates the lexan sabot, LiF window, quartz driver, forsterite sample, and forsterite window. The driver and window materials are chosen to minimize x-ray attenuation. Diffracted x-rays are collected every 153.4 ns on an LSO scintillator coupled to a four frame imaging system.

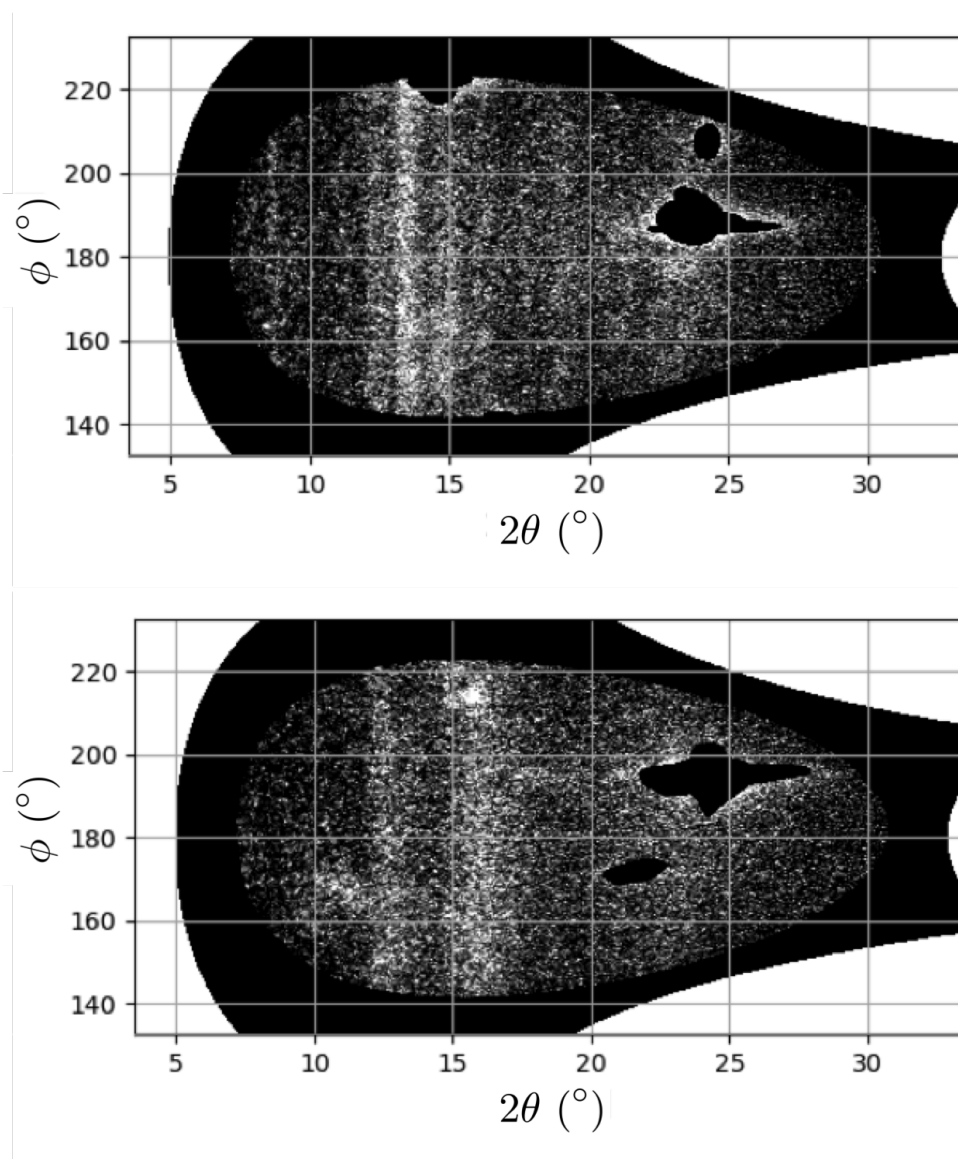


Figure 2.7: **Diffraction data for shocked forsterite.** Diffraction data is dewarped into the diffraction coordinates  $2\theta$ - $\phi$ . The powder peaks correspond to diffraction from the shocked polycrystalline forsterite. The masked out regions (black) correspond to single-crystal like diffraction from the LiF window and do not represent diffraction from the forsterite sample. Top: diffraction pattern for forsterite shocked to 44.6(7.0) GPa. Bottom: diffraction pattern for forsterite shocked to 73.4(9.0) GPa.

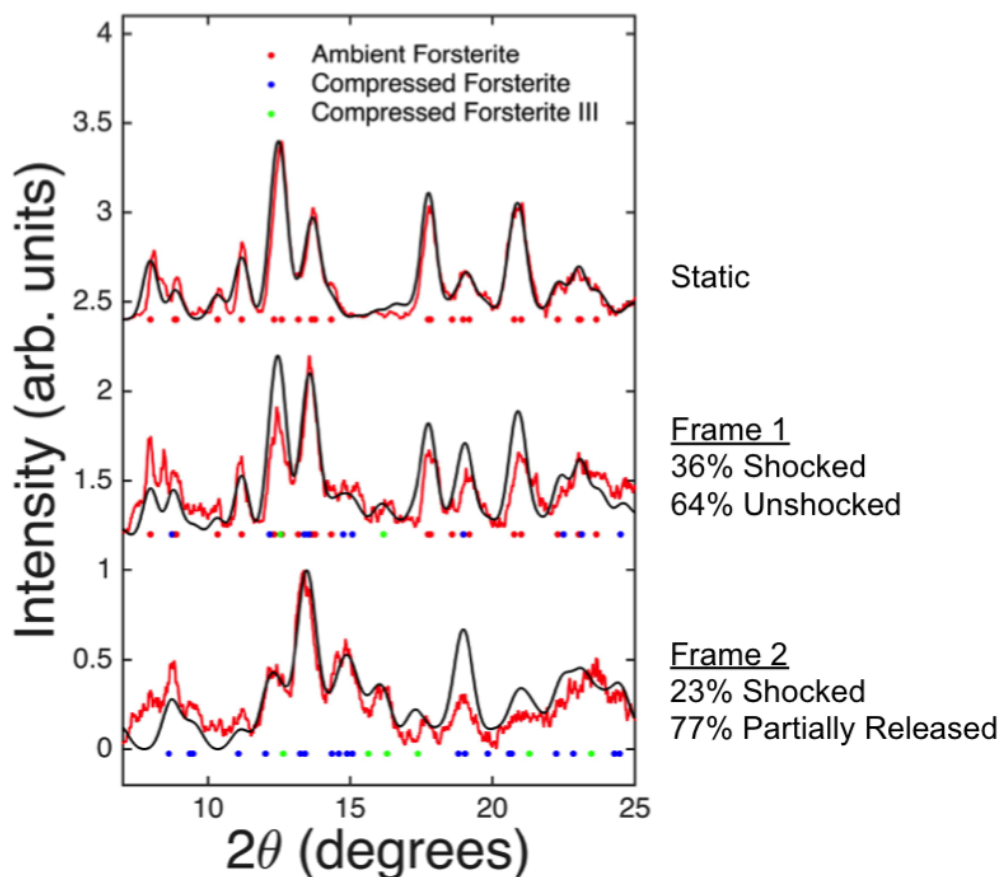


Figure 2.8: **X-ray diffraction lineout for forsterite shocked to 44.6(7.0) GPa and released to 38.4(8.0) GPa.** Experimental lineout (red) compared to the theoretical lineout (black) for a mixture of shocked and released forsterite and forsterite III. The red blue and green data points indicate diffraction peaks for ambient forsterite, compressed forsterite, and compressed forsterite III respectively with a threshold of 10%. The lattice parameters for forsterite and forsterite III are determined by power law fit to the isothermal diamond anvil cell data. Therefore the theoretical diffraction assumes that temperature does not distort the ratios of the lattice parameters. The ratio of forsterite to forsterite III is determined to be 3 to 1 by fitting the theoretical lineout to the data to give the correct relative intensity of the (112) forsterite peak and the (131) forsterite III peak.

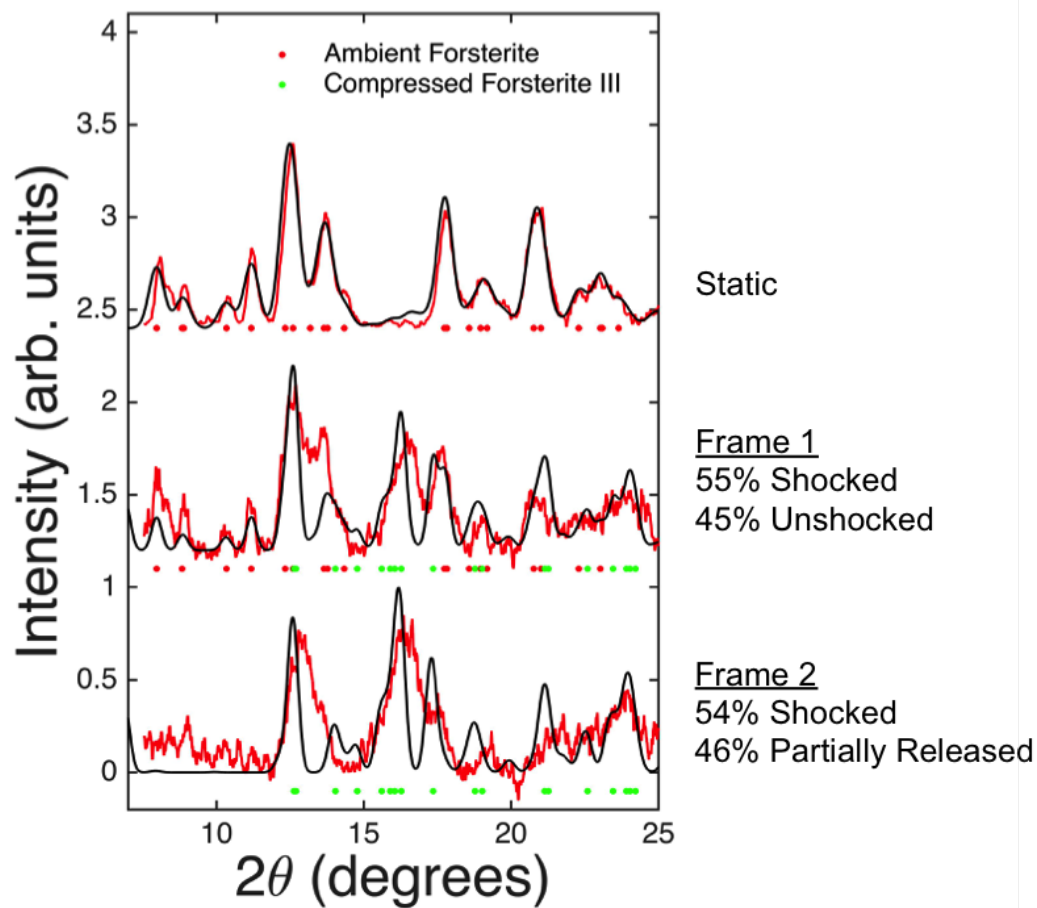


Figure 2.9: X-ray diffraction lineout for forsterite shocked to 73.4(9.0) GPa and released to 66.16(10.0) GPa. Progression of experimental lineouts (red) compared to the theoretical lineouts (black) of the forsterite III structure. The red and green data points indicate diffraction peaks for ambient forsterite and compressed forsterite III with a threshold of 10%.

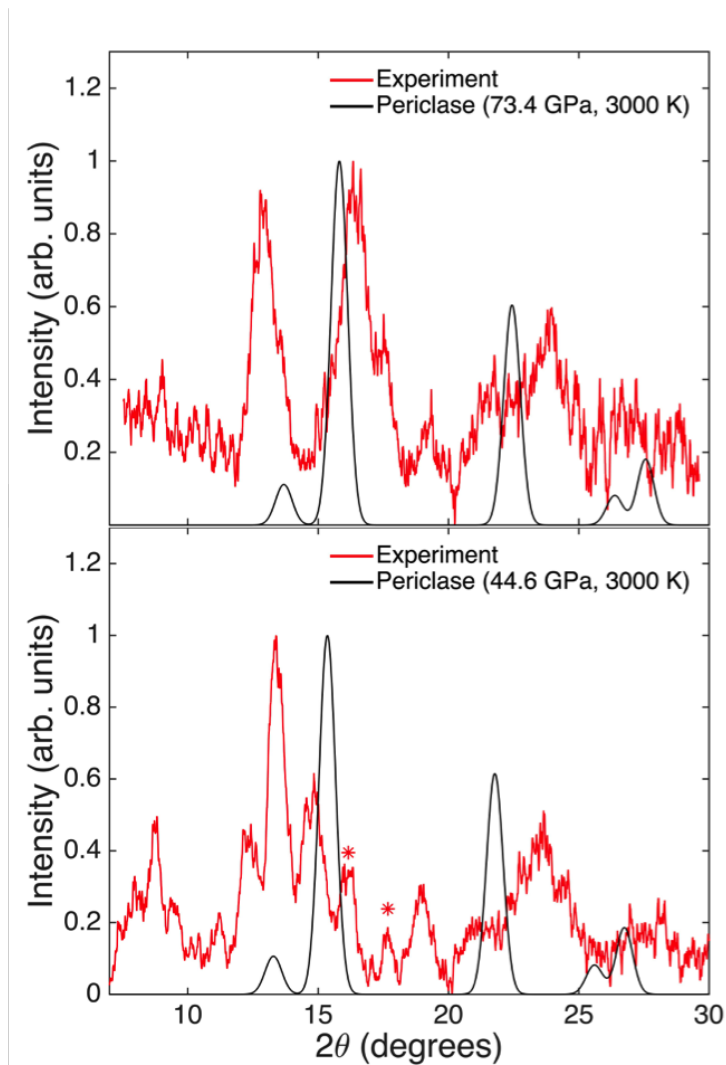


Figure 2.10: **Comparison of observed diffraction to expected diffraction from periclase.** Diffraction from the periclase structure at the pressures and temperatures relevant to the forsterite Hugoniot are compared to the diffraction data observed in shot 084 frame 2 (bottom) and shot 085 frame 2 (top). The asterisks (bottom) correspond to diffraction peaks not already indexed as diffraction from shock compressed forsterite.

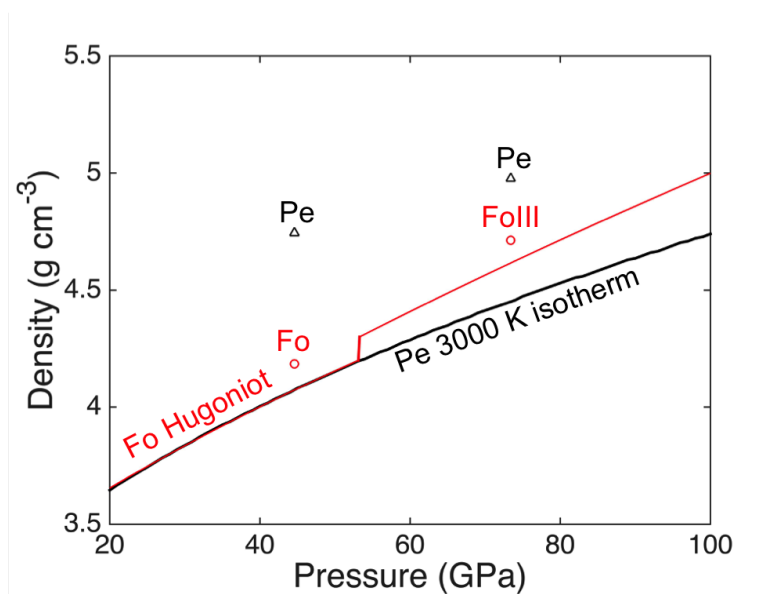


Figure 2.11: **Comparison of expected density to density inferred from the diffraction pattern.** The density of periclase, forsterite, and forsterite III are compared to the expected values based upon the previously measured forsterite Hugoniot and the 3000 K periclase isotherm from equations of state (Tange, Nishihara, and Tsuchiya, 2009; Wu et al., 2008). The density required to fit the periclase structure is well outside the uncertainty in the periclase isotherm while the forsterite structures are in good agreement with the Hugoniot density.

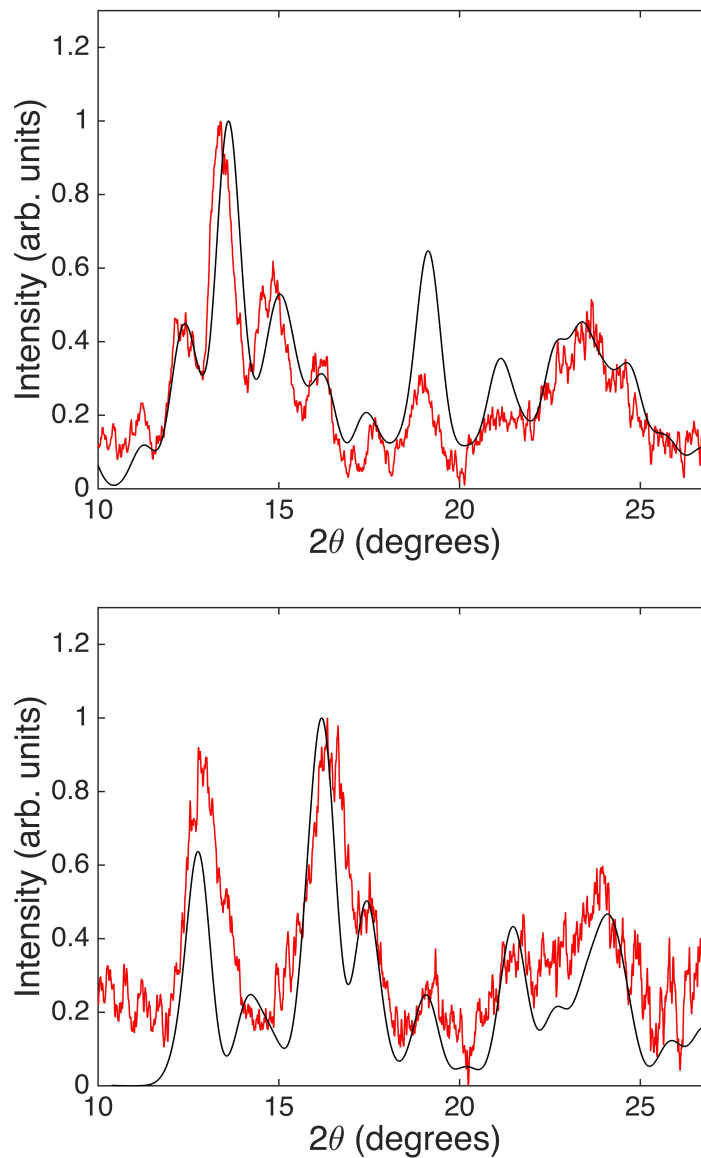


Figure 2.12: **Lineouts fit to the diffraction data for shot 084 frame 2 (top) and shot 085 frame 2 (bottom).** Lattice parameters were fit to the observed diffraction data (Table 2.3) using the Hugoniot density and ambient temperature crystal structure from Finkelstein as an initial guess. The resulting fits are slightly more dense than expected from the Hugoniot bulk density, but well within uncertainties ( $< 3\%$ ).

## References

- Adjaud, O., G. Steinle-Neumann, and S. Jahn (2011). “Transport properties of  $\text{Mg}_2\text{SiO}_4$  liquid at high pressure: Physical state of a magma ocean”. In: *Earth and Planetary Science Letters* 312, pp. 463–470.
- Asimow, P. (2017). “A measure of mantle melting”. In: *Science* 355, pp. 908–909.
- Brown, M., M. Furnish, and D. Boness (1987). “Sound velocities for San Carlos olivine”. In: *Shock Waves in Condensed Matter*, pp. 119–122.
- Coppiari, F. et al. (2013). “Experimental evidence for a phase transition in magnesium oxide at exoplanet pressures”. In: *Nature Geoscience* 6.11.
- De Koker, N., B. Karki, and L. Stixrude (2013). “Thermodynamics of the  $\text{MgO-SiO}_2$  liquid system in Earth’s lowermost mantle from first principles”. In: *Earth and Planetary Science Letters* 361, pp. 58–63.
- De Koker, N. and L. Stixrude (2009). “Self-consistent thermodynamic description of silicate liquids, with application to shock melting of  $\text{MgO}$  periclase and  $\text{MgSiO}_3$  perovskite”. In: *Geophysical Journal International* 178.1, pp. 162–179.
- De Koker, N., L. Stixrude, and B. Karki (2008). “Thermodynamics, structure, dynamics, and freezing of  $\text{Mg}_2\text{SiO}_4$  liquid at high pressure”. In: *Geochimica et Cosmochimica Acta* 72, pp. 1427–1441.
- Duffy, T. and T. Ahrens (1992). “Sound velocities at high pressure and temperature and their geophysical implications”. In: *Journal of Geophysical Research: Solid Earth* 97.B4, pp. 4503–4520.
- Fei, H. (2013). “Silicon and oxygen self-diffusion in forsterite and implications to upper-mantle rheology”. PhD thesis.
- Fei, Y. et al. (2004). “Experimentally determined postspinel transformation boundary in  $\text{Mg}_2\text{SiO}_4$  using  $\text{MgO}$  as an internal pressure standard and its geophysical implications”. In: *Journal of Geophysical Research: Solid Earth* 109.B2.
- Finkelstein, G. et al. (2014). “Phase transitions and equation of state of forsterite to 90 GPa from single-crystal X-ray diffraction and molecular modeling”. In: *American Mineralogist* 99.1, pp. 35–43.
- Gleason, A et al. (2015). “Ultrafast visualization of crystallization and grain growth in shock-compressed  $\text{SiO}_2$ ”. In: *Nature communications* 6.
- Hawreliak, J et al. (2007). “High pressure nano-crystalline microstructure of shock compressed single crystal iron”. In: *Physical Review B* 78.UCLL-JRNL-237258.
- Jackson, I. and T. Ahrens (1979). “Shock-wave compression of single crystal forsterite”. In: *Journal of Geophysical Research* 84, pp. 3039–3048.
- Jeanloz, R. (1980). “Shock effects in olivine and implications for Hugoniot data”. In: *Journal of Geophysical Research: Solid Earth* 85.B6, pp. 3163–3176.

- Luo, S-N, T. Akins J. and Ahrens, and P. Asimow (2004). "Shock-compressed Mg-SiO<sub>3</sub> glass, enstatite, olivine, and quartz: Optical emission, temperatures, and melting". In: *Journal of Geophysical Research: Solid Earth* 109.B5.
- Lyzenga, G. and T. Ahrens (1980). "Shock temperature measurements in Mg<sub>2</sub>SiO<sub>4</sub> and SiO<sub>2</sub> at high pressures". In: *Geophysical Research Letters* 7.2, pp. 141–144.
- Marsh, Stanley P (1980). *LASL shock Hugoniot data*. Vol. 5. Univ of California Press.
- Mosenfelder, J., P. Asimow, and T. Ahrens (2007). "Thermodynamic properties of Mg<sub>2</sub>SiO<sub>4</sub> liquid at ultra-high pressures from shock measurements to 200 GPa on forsterite and wadsleyite". In: *Journal of Geophysical Research: Solid Earth* 112.
- Mosenfelder, J., N. Deligne, et al. (2006). "Hydrogen incorporation in olivine from 2–12 GPa". In: *American Mineralogist* 91.2-3, pp. 285–294.
- Murakami, M. et al. (2004). "Post-perovskite phase transition in MgSiO<sub>3</sub>". In: *Science* 304.5672, pp. 855–858.
- Oganov, A. and S. Ono (2004). "Theoretical and experimental evidence for a post-perovskite phase of MgSiO<sub>3</sub> in Earth's D" layer". In: *Letters to Nature*, pp. 445–448.
- Presnall, D. et al. (1998). "Liquidus phase relations in the system MgO–MgSiO<sub>3</sub> at pressures up to 25 GPa—constraints on crystallization of a molten Hadean mantle". In: *Physics of the Earth and Planetary Interiors* 107.1, pp. 83–95.
- Rigg, P. et al. (2014). "Determining the refractive index of shocked [100] lithium fluoride to the limit of transmissibility". In: *Journal of Applied Physics* 116.
- Strand, O. et al. (2006). "Compact system for high-speed velocimetry using heterodyne techniques". In: *Review of Scientific Instruments* 77.8, p. 083108.
- Syono, Y., T. Goto, J.-I. Sato, et al. (1981). "Shock compression measurements of single-crystal forsterite in the pressure range 15–93 GPa". In: *Journal of Geophysical Research: Solid Earth* 86.B7, pp. 6181–6186.
- Syono, Y., T. Goto, H. Takei, et al. (1981). "Dissociation reaction in forsterite under shock compression". In: *Science* 214.4517, pp. 177–179.
- Tange, Y., Y. Nishihara, and T. Tsuchiya (2009). "Unified analyses for P-V-T equation of state of MgO: A solution for pressure-scale problems in high P-T experiments". In: *Journal of Geophysical Research: Solid Earth* 114.B3.
- Wett, J. and T. Ahrens (1983). "Shock compression of single-crystal forsterite". In: *Journal of Geophysical Research: Solid Earth* 88.B11, pp. 9500–9512.
- Wu, Z. et al. (2008). "Pressure-volume-temperature relations in MgO: An ultrahigh pressure-temperature scale for planetary sciences applications". In: *Journal of Geophysical Research: Solid Earth* 113.B6.

## DECOMPOSITION OF FORSTERITE INTO MGO AND SILICA RICH LIQUID ON NANOSECOND TIMESCALES

### 3.1 Introduction

Modeling the interior structure and thermal evolution of the Earth's mantle requires knowledge of the equation of state of mantle materials at the thermodynamic conditions that exist deep within the Earth (Asimow, 2017; Y. Fei et al., 2004; Shim, Duffy, and Shen, 2001).  $\text{Mg}_2\text{SiO}_4$  forsterite is relatively close to the bulk silicate Earth composition and has been studied extensively at high pressure (Mosenfelder, Asimow, and Ahrens, 2007; Syono, Goto, Takei, et al., 1981; Brown, Furnish, and Boness, 1987; De Koker, Karki, and Stixrude, 2013; Finkelstein et al., 2014; Lyzenga and Ahrens, 1980). A schematic phase diagram for the MgO-MgSiO<sub>3</sub> join is shown in Figure 3.1. First-principles molecular dynamics simulations indicate that forsterite is silica poor relative to the eutectic composition, and therefore a sub-liquidus phase assemblage of MgO in coexistence with silica rich liquid is expected for systems in equilibrium ( $x \text{ MgO (s)} + \text{Mg}_{2-x}\text{SiO}_{4-x} \text{ (l)}$ ) (De Koker, Karki, and Stixrude, 2013). Furthermore, melting point depression relative to pure MgO is expected due to the entropy of mixing within the liquid phase. This qualitative picture is expected to describe the MgO-MgSiO<sub>3</sub> system at pressures above 125 GPa, where bridgmanite transforms to post-perovskite, and below 300 GPa, where MgO transforms from the B1 rocksalt structure to the B2 cesium chloride structure. At these pressures, Figure 3.1 shows that there is no stable compound with  $\text{Mg}_2\text{SiO}_4$  composition. Therefore, achieving an equilibrium state from an initially homogeneous forsterite crystal necessarily involves decomposition into at least two compounds with different composition and hence creation of chemically heterogeneous domains from the originally homogeneous material, a process that we refer to as "chemical segregation". Chemical segregation in magnesium silicates is well-established at all pressures above 23 GPa from detailed static high pressure experiments (Shim, Duffy, and Shen, 2001; Presnall et al., 1998). Forsterite com-

---

This chapter is in preparation for submission with Richard G. Kraus, June K. Wicks, Raymond F. Smith, Thomas S. Duffy, Paul D. Asimow, and Jon H. Eggert.

position is shown to decompose to structures with MgO and MgSiO<sub>3</sub> composition, while MgSiO<sub>3</sub> is expected to stay a compound until 10 megabars and approximately 10,000 K (K. Umemoto, 2006).

To reach the pressure and temperature conditions of interest to the Earth's mantle, researchers have traditionally used shock compression via uniaxial plate impact experiments (Mosenfelder, Asimow, and Ahrens, 2007; Syono, Goto, Takei, et al., 1981; Brown, Furnish, and Boness, 1987; Furnish and Brown, 1986; Wett and Ahrens, 1983; Jackson and Ahrens, 1979; Jeanloz, 1980; Luo, Akins, and Asimow, 2004; Y. Syono, 1982). From these experiments, several phase regimes have been delineated on the basis of density variation and sound speed discontinuities. Data up to 50 GPa on the principal Hugoniot were interpreted by Syono et al. as metastable forsterite in a so-called low-pressure phase (LPP) regime (Syono, Goto, Sato, et al., 1981). A mixed phase (MP) has been proposed between 50 and 120 GPa, however the nature of this region is poorly understood. Analysis of recovered samples shocked to 90 GPa by Syono et al. show evidence of crystalline MgO and glassy material with MgSiO<sub>3</sub> composition interpreted as chemical segregation in the shock state (Y. Syono, 1982). In contrast, recovered samples shocked to 75 GPa by Jeanloz, 1980 showed no evidence of decomposition (Jeanloz, 1980). The data between 97 GPa and 130 GPa were interpreted by Mosenfelder, Asimow, and Ahrens, 2007 as a solid state high-pressure phase (HPP) region consistent with decomposition of forsterite to the equilibrium sub-solidus phase assemblage of periclase and bridgmanite (Mosenfelder, Asimow, and Ahrens, 2007). Sound velocity measurements indicate the onset of melting at 140 GPa as evidenced by a drop in the sound speed corresponding to the transition from the longitudinal sound speed of a solid to the slower bulk sound speed of a partial liquid (Brown, Furnish, and Boness, 1987).

While dynamic compression techniques have been used extensively to study silicate minerals, without direct evidence of the phase or phase assemblage behind the shock front, the long standing question regarding the nature of the state (equilibrium or metastable) behind the shock front remains unanswered. This question is especially pertinent for forsterite, as the expected decomposition to periclase plus bridgmanite in the high pressure phase region and periclase plus silica rich liquid in the partial melt region requires chemical segregation, which may be rate limited by the diffusivity of the solution from which the periclase is precipitated. The question is magnified in the case of laser driven dynamic compression experiments that have a

characteristic timescale two to three orders of magnitude shorter than plate impact experiments. On laser platforms, the duration of the experiment is limited by the nanosecond pulse duration of the laser rather than the flyer geometry for uniaxial plate impact experiments.

In this paper, we present results for single-crystal forsterite shocked to pressures from 115 GPa to 215 GPa, where we observe partial melting above 140 GPa and complete melting above 195 GPa. For nanometer sized grains and ionic diffusivities within the solid of  $10^{-6} \text{ nm}^2 \text{ ns}^{-1}$  we calculate a characteristic time of  $10^6 \text{ ns}$  for diffusion limited growth of a new phase, and therefore expect the sub-solidus phase assemblage of periclase and post-perovskite is unattainable on nanosecond timescales if solid state diffusion is the rate limiting process (H. Fei, 2013). For nanometer sized grains and liquid diffusivities of  $0.01 \text{ nm}^2 \text{ ns}^{-1}$  we calculate a characteristic time for diffusion limited growth of 1 ns, and so decomposition in the partial melt regime is possible (De Koker, Stixrude, and Karki, 2008).

### 3.2 Methods

Experiments were conducted at the Omega Extended Pulse (EP) Laser, Laboratory for Laser Energetics, University of Rochester. Omega EP is a four beam laser capable of delivering up to 5000 J per beam of up to 10 ns duration onto mm diameter targets (Meyerhofer et al., 2010). Laser drives were used to both dynamically compress forsterite targets and generate an x-ray source. Velocimetry measurements were used to infer the sample pressure through impedance matching.

#### Sample Preparation

The forsterite starting material (obtained from MolTech GmbH) was cut and polished from a single-crystal rod. For the experiments that probed states on the forsterite Hugoniot, a typical target package consists of a forsterite sample sandwiched between a kapton ablator (GoodFellow Corp.) and lithium fluoride (LiF) window and centered over a Ta pinhole with  $300 \mu\text{m}$  diameter aperture. For the experiments that probed resolidified states, Be was substituted for kapton as an ablator due to its faster sound speed which helps to prevent ramp compression waves steepening to shocks. The nominal target dimensions for each configuration are shown in Figure 3.2. For each experiment, there is a  $1 \mu\text{m}$  thick aluminum layer between the forsterite sample and LiF window to improve the interface reflectivity for VISAR measurements as well as a thin  $< 1 \mu\text{m}$  epoxy layer.

### **Laser Driven Compression**

To generate the shock state in the forsterite sample, laser energy was deposited onto a kapton ablator. Kapton is used as an ablator because it is relatively low-Z and therefore the x-ray emission spectrum from the ablation plasma is relatively soft, so it will be attenuated within the kapton ablator itself and will not heat the sample or contribute to background emission on the x-ray detector. The ablation process generates an expanding plasma which from conservation of momentum drives a shock in the opposite direction of the expansion. The ablation process continues through the duration of the laser pulse as the laser continuously adds energy to the plasma to compensate for adiabatic cooling due to expansion of the plasma plume (Swift and G. Kraus, 2008). In this study, we used a composite laser drive composed of two 10 ns beams stacked sequentially in time as shown in Figure 3.3. The first beam used a 2.0 mm diameter phase plate while the second used a 1.1 mm diameter phase plate. The purpose of the phase plates is to spatially smooth the beam to produce an even beam intensity over the area of the phase plate.

We also performed shock-melt ramp-resolidification studies, which consist of a three step process whereby the forsterite sample undergoes shock compression, isentropic release and shockless compression, similar to the approach of J. Nguyen, 2004. First, the sample was shocked to a state near the liquidus using a composite laser pulse consisting of two 10 ns, 1.1 mm beams stacked in series. The purpose of the initial shock is to heat the sample to a partially molten state. Second, the sample isentropically releases into a LiF window, whereby the pressure in the sample reduces by about 20%, a process that further favors melting. Third, the sample is shocklessly compressed back across the liquidus using a 10 ns, 1.1 mm tailored “ramped” laser pulse. We observe that the ramp does not steepen into a shock in the VISAR profile (Figure 3.5). The sample is probed with x-rays in the re-solidified state. A characteristics diagram showing the wave interactions for these experiments is shown in Figure 3.4. The composite laser pulse shape is shown in Figure 3.5. In measuring the transformation from liquid to solid, we are able to observe the partially molten equilibrium phase assemblage by following a pressure-temperature path that is kinetically constrained by the liquid diffusivity. The thermodynamic path of the sample is illustrated in Figure 3.6.

### **Pressure Determination**

The apparent particle velocity at the interface between the forsterite and the LiF was measured using a line imaging VISAR, which was converted to the true interface

velocity using the measured index of refraction for LiF (Rigg et al., 2014; Celliers et al., 2013). The interferometer records the fringe shift of reflected light to an accuracy of  $\pm 5\%$ . The ambiguity in velocity due to integer fringe shifts is resolved using two channels with different velocity sensitivities. The data are linearly fit using a total least squares approach that includes uncertainties in both the particle and shock velocity (Krystek and Anton, 2007; Ruoff, 1967). We fit the data in the range of 90 - 140 GPa and 140 - 200 GPa separately, on the basis of sound velocity measurements that indicate partial melt at 140 GPa (Brown, Furnish, and Boness, 1987). For the data between 90 GPa and 140 GPa, we find the following best fit and covariance matrix (Figure 3.7):

$$U_{S,HPP} = 2.61 + 1.91u_{p,HPP} \quad (3.1)$$

$$\sigma_{C_0,S}^2 = \begin{bmatrix} 1.98 & -0.44 \\ -0.44 & 0.10 \end{bmatrix} \quad (3.2)$$

$$\chi^2 = 0.03. \quad (3.3)$$

For the data above 140 GPa, we find the following best fit and covariance matrix (Figure 3.7):

$$U_{S,PM} = 4.39 + 1.58u_{p,PM} \quad (3.4)$$

$$\sigma_{C_0,S}^2 = \begin{bmatrix} 1.90 & -0.49 \\ -0.49 & 0.13 \end{bmatrix} \quad (3.5)$$

$$\chi^2 = 0.024. \quad (3.6)$$

At late times relative to the x-ray probe time, we observe a ramp in the velocity profile as shown in Figure 3.3 (bottom). The experiment was simulated using HYADES, a radiation hydrodynamics code, and the observed wave unsteadiness was identified as inadvertent steepening of the laser pulse readily seen in the discrepancy between the ideal laser pulse shape and the delivered laser pulse shape shown in Figure 3.3 (Larsen and Lane, 1994). The simulation showed that wave unsteadiness occurred sufficiently late in time such that the bulk of the experimental sample was in a uniform shock state during the x-ray probe time.

In the shock-melt ramp-resolidification experiments, the particle velocity was measured using VISAR at the interface between the forsterite sample and LiF window. The pressure in the sample following ramp compression was determined by matching the observed VISAR profile to hydrodynamic simulations of the experiment conducted using HYADES. A characteristic VISAR trace is shown in Figure 3.5

(bottom). The deviation of the simulated VISAR profile from the experimental VISAR profile is minimized by adjusting the ablator thickness to match the shock breakout time and the laser energy to match the shock and ramp wave amplitude. Adjusting the simulated ablator thickness is justified as the SESAME equation of state for Be is not a perfect fit to the Be Hugoniot suggesting systematic wave speed errors, which are accounted for by making small adjustments to the simulated ablator thickness. Adjusting the laser energy from the measured value is justified due to the uncertainty in the area of the laser spot as well as inaccuracies in the radiation hydrodynamics package within HYADES. This technique for determining the pressure is justified in that the LiF interface velocity robustly defines the peak pressure in the LiF itself. Due to the relatively long timescale of the shockless compression process, the forsterite is in pressure equilibrium with the LiF. Consequently, the pressure determination process is relatively insensitive to the equation of state of the forsterite, but is instead sensitive to the LiF equation of state, which is well constrained. Furthermore, we can tolerate large uncertainties in the ramp pressure (up to 15%) for the purpose of determining the sub-liquidus phase assemblage upon recrystallization.

### **In Situ X-ray Diffraction**

Powder x-ray diffraction is used to probe the crystal structure and melt transition of shocked forsterite. Diffraction in the shock compressed state is recorded using the Powder X-Ray Diffraction with Image Plates (PXRDIIP) diagnostic (Rygg et al., 2012). While the sample is compressed, illumination of a Cu foil generates quasi-monochromatic He $\alpha$  x-rays of 8.35 keV with a bandwidth of 2%. X-rays of ~3 ns duration were generated by focusing 2 beams with 2400 J each onto a 265  $\mu\text{m}$  diameter spot on a 2 mm  $\times$  2 mm  $\times$  12.5  $\mu\text{m}$  Cu foil. The emitted x-rays penetrate the entire target stack, and the scattered x-rays are collected on image plates which line a 5  $\times$  5  $\times$  7.5 cm<sup>3</sup> box surrounding the sample as illustrated in Figure 3.2. The d-spacing of the x-ray diffraction peaks and the known equation of state of periclase are used to interpret crystal structure, and the peak widths are used to calculate grain size from the Scherrer equation (Patterson, 1939). This provides an upper bound on the actual grain size, as other effects such as density gradients and instrument broadening may contribute to peak broadening (J Hawreliak et al., 2007; Gleason et al., 2015).

We compare our diffraction results to the expected diffraction signals from forsterite, forsterite III, bridgmanite, post-perovskite, and periclase (Tange, Kuwayama, et al.,

2012; Fiquet, Andrault, et al., 1998; Fiquet, Dewaele, et al., 2000; Sakai, Dekura, and Hirao, 2016; Murakami et al., 2004; Tange, Nishihara, and Tsuchiya, 2009; Wu et al., 2008). Due to decomposition of forsterite into a phase assemblage where the relative volume fraction is a free parameter, the bulk density of the material determined from the Hugoniot relations does not determine the density of the individual components of the system. Therefore, equations of state taken from literature are used with the experimental pressure and temperature as inputs to determine the lattice parameters for candidate structures.

### **3.3 Results**

We performed 12 shock compression experiments where we observed pressures ranging from 117(10) GPa to 214(19) GPa. The shock states achieved in each experiment are listed in Table 3.1.

#### **Hugoniot states within the Solid**

In the solid phase region, we observe a textured solid in samples shocked to 119(10) GPa. The dewarped and background subtracted image plates are shown in Figure 3.8. In each of the three experiments conducted in this region on the Hugoniot, we observe diffraction from three distinct crystallographic orientations, with crystal planes rotated  $33^\circ$  from each other as determined from the diffraction condition. The texture of the material is suggestive of twinning, where the observed relative crystal plane angles of  $\pm 33^\circ$  (Table 3.3) may correspond to the two twin solutions required from frame indifference. Furthermore, the high degree of texturing is inconsistent with a reconstructive phase change which is required for chemical segregation of forsterite into post-perovskite and periclase. While we have not assigned a crystal structure, the observed d-spacings are inconsistent with the expected diffraction peaks for the periclase, perovskite, and post perovskite candidate structures at the same temperature and pressure conditions as the forsterite Hugoniot. Figures 3.9-3.11 show the mismatch between the observed d-spacing and the predicted d-spacing for each candidate equilibrium structure (periclase, bridgmanite, and post-perovskite).

#### **Partial Melt Region**

In the partial melt region, we observe diffraction signatures consistent with diffuse liquid scattering in coexistence with a fine grained solid. Examples of the raw and processed image plates for partially molten and completely molten are shown in Fig-

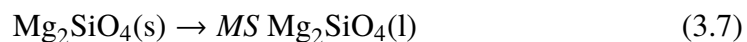
ures 3.12 and 3.13 respectively. We interpret the Hugoniot data in the pressure range from 147(12) GPa to 192(16) GPa as incongruent melting of forsterite into periclase and silica-rich liquid. We observe an untextured solid diffraction peak consistent with scattering from the (002) B1 plane of periclase as well as a broad peak which we interpret as diffuse liquid scattering. Absence of the expected (111) and (220) B1 diffraction peaks is not surprising because they are an order of magnitude less intense than the (002) diffraction peak. Furthermore, at the elevated temperatures induced by the shock, the (220) peak is likely to be further damped by the Debye-Waller factor. Figure 3.14 shows observed d-spacing as a function of pressure for the forsterite shock compression experiments compared to the expected values for periclase, while Figures 3.15 - 3.17 rule out other potential candidate structures. Expected d-spacings are determined by calculating the density of periclase (and other candidate structures) at the temperature and pressure on the forsterite Hugoniot using an equation of state (Tange, Nishihara, and Tsuchiya, 2009; Wu et al., 2008). This calculation assumes that each component of the phase assemblage is in thermal equilibrium, where thermal and pressure equilibrium should occur on the nanosecond timescale for nanometer sized grains (Tang and Dong, 2010; Osako, Ito, and Yoneda, 2004). The Hugoniot temperature is determined from ab-initio calculations of the periclase plus  $\text{MgSiO}_3$  liquid phase assemblage by De Koker, Stixrude, and Karki, 2008 as well as from pyrometry experiments published by Luo et al. (Luo, Akins, and Asimow, 2004; De Koker, Stixrude, and Karki, 2008). The uncertainty in density due to thermal expansion of periclase is small relative to the uncertainty in density calculated from the observed diffraction angle. Grain size of periclase calculated from the Scherrer equation was determined to be  $115 \pm 40$  nm across four observations. Loss of the (200) diffraction peak and persistence of liquid diffuse scattering (Figure 3.13) bounds the complete Hugoniot melting pressure between 192(16) GPa and 197(14) GPa.

We performed shock-melt resolidification experiments to further validate the sub-liquidus coexistence of periclase and silica rich liquid. In these experiments, the forsterite was shock compressed into the partial melt regime. The forsterite then partially releases into a LiF window through an isentropic process that thermodynamically favors the liquid phase. We then use a tailored laser pulse shape to shocklessly compress the sample through a process that thermodynamically favors crystallization of periclase. Upon solidification from liquid, we observe an intense polycrystalline diffraction peak consistent with diffraction from the B1 (200) crystal plane with possible diffraction from the B1 (111) crystal plane. The d-spacing as a

function of pressure showing good agreement with the periclase structure is shown in Figure 3.18. Examples of the raw and process image plates are shown in Figure 3.19.

### 3.4 Discussion

In the solid region of the Hugoniot, we do not observe any of the sub-solidus candidate structures expected in equilibrium (periclase, bridgmanite, or post-perovskite). This result shows that chemical decomposition of forsterite does not occur on nanosecond timescales for solid state diffusion which validates previous measurements of the solid state diffusivity of forsterite (H. Fei, 2013; Farver, Yund, and Rubie, 1994). Our measurement does not necessarily resolve the discrepancy in shock-recovery experiments by Syono and Jeanloz on plate impact timescales, which are 2 to 3 orders of magnitude longer (Syono, Goto, Takei, et al., 1981; Jeanloz, 1980). In the partial melt regime, we observe crystallization of periclase on nanosecond timescales. The measured grain sizes validate first principles calculations of the diffusivity of forsterite liquid at the same pressure and temperature conditions as shown in Figure 3.20 (De Koker, Stixrude, and Karki, 2008). The crystallization of periclase under the kinetic constraints imposed by the timescale of laser driven compression experiments suggests that the path to equilibrium is governed by the diffusivity of the liquid through a two step process of metastable forsterite melt followed by crystallization of periclase:



Our measurement of periclase in equilibrium with silica rich liquid is consistent with previous interpretations of existing shock data in the same pressure range. Our data is consistent with the interpretation of de Koker that the discrepancy in calculated ( $11.5 \text{ km s}^{-1}$ ) versus measured ( $10.8 \text{ km s}^{-1}$ ) sound speed on the forsterite Hugoniot at 168 GPa is due to a partially molten sample, where the reduction in sound speed is explained by mass transfer induced by the pressure perturbation (Mosenfelder, Asimow, and Ahrens, 2007; Syono, Goto, Takei, et al., 1981; De Koker and Stixrude, 2009). Our observation of partial melting explains the large apparent heat capacity in the shock temperature data of Luo as latent heat of melting (Luo, Akins, and Asimow, 2004; De Koker and Stixrude, 2009).

### 3.5 Conclusions

This work provides the first in situ observation of the decomposition of forsterite into periclase during a dynamic compression experiment and supports the equilibrium result that the eutectic composition for the MgO - SiO<sub>2</sub> join is between the forsterite (Mg<sub>2</sub>SiO<sub>4</sub>) and enstatite (MgSiO<sub>3</sub>) composition (De Koker and Stixrude, 2009). This result informs our understanding of the evolution of the Earth's mantle, and in particular how phase segregation in magnesium silicate melts likely present during the late stages of accretion may be imprinted on the chemical structure of the mantle today (Urey, 1955; Tonks and Melosh, 1993; Hanks and Anderson, 1969).

We found that chemical segregation in forsterite is not possible by solid state diffusion, but that equilibrium can be observed on nanosecond timescales if the process is rate limited by the diffusivity of the forsterite liquid. The crystallization of periclase under the kinetic constraints imposed by the timescale of laser driven compression experiments suggests that the path to equilibrium is a two step process of metastable forsterite melt followed by crystallization of MgO. In this way, we are able to determine both the equilibrium crystal structure from the diffraction pattern as well as suggest a path to equilibrium through consideration of the kinetic constraints. This study illustrates the key role that kinetics plays during dynamic experiments and provides an interesting case study in the conditions required for equilibrium on dynamic compression timescales for multicomponent materials that may phase segregate. Dynamic compression techniques make the extreme conditions that are relevant to the interior of super-Earth sized planetary bodies accessible in the laboratory. However, care must be taken when studying the phase diagram of multi-component systems so that chemical segregation can occur on nanosecond timescales.

Campaign	Shot	$U_{\text{int}}$ (km s <sup>-1</sup> )	P (GPa)
XRDEOSEP15A	21387	5.08(26)	183(15)
XRDEOSEP15A	21388	4.44(22)	147(12)
XRDEOSEP15B	21914	4.69(24)	160(13)
XRDEOSEP15B	21917	3.90(20)	117(10)
XRDEOSEP15B	21919	3.91(20)	118(10)
XRDEOSEP15B	21920	3.94(20)	119(10)
XRDEOSEP15B	21922	5.25(26)	192(16)
XRDEOSEP15B	21923	5.61(28)	214(19)
XRDEOSEP15B	21924	4.67(23)	159(13)
XRDEOSEP17B	25201	4.66(23)	159(13)
XRDEOSEP17B	25202	5.06(23)	181(14)
XRDEOSEP17B	25203	5.33(23)	197(14)

Table 3.1: **Shock States Achieved In Each Experiment.** Tabulation of the measured interface velocity from VISAR and the shock pressure from the impedance match calculation. The uncertainty in the interface velocity includes 5% uncertainty in VISAR phase, the uncertainty associated with wave unsteadiness, and the uncertainty in the velocity correction due to the LiF index of refraction.

Table 3.2: Textured Diffraction Angles

Shot	Peak	$2\theta$ (°)	$\phi$ (°)
21917	1	64.234	37.688
21917	2	63.333	-0.65
21917	3	63.694	-40.09
21919	1	64.324	39.189
21919	2	63.423	-0.45
21919	3	63.784	-37.0
21920	1	64.234	38.589
21920	2	63.243	-0.75
21920	3	63.243	-40.991

Table 3.3: Relative Crystal Plane Angles

Shot	$\angle_{1,2}$ (°)	$\angle_{2,3}$ (°)	$\angle_{1,3}$ (°)
21917	32.4(60)	33.3(62)	64.3(58)
21919	33.4(62)	30.9(62)	63.0(58)
21920	33.2(62)	34.1(62)	65.8(58)

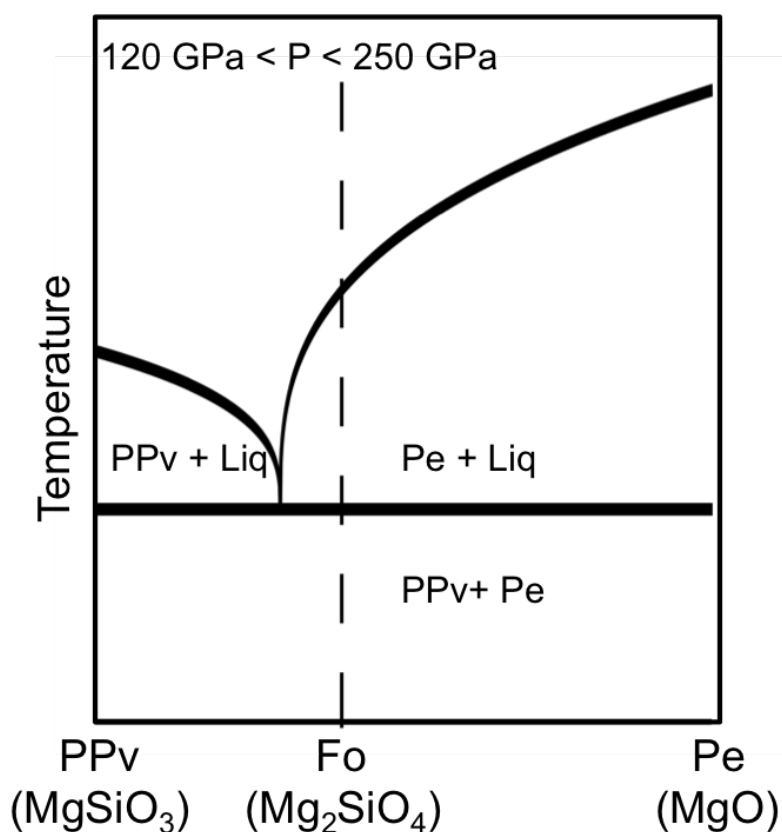


Figure 3.1: Schematic illustration of the equilibrium phase boundaries in temperature versus composition space for a snapshot in pressure (De Koker, Karki, and Stixrude, 2013). For a forsterite composition, the sub-solidus phase assemblage is expected to be post-perovskite ( $\text{MgSiO}_3$ ) plus periclase (B1  $\text{MgO}$ ). Forsterite is believed to be silica poor relative to the eutectic composition, indicating a sub-liquidus phase assemblage of periclase plus silica-rich liquid.

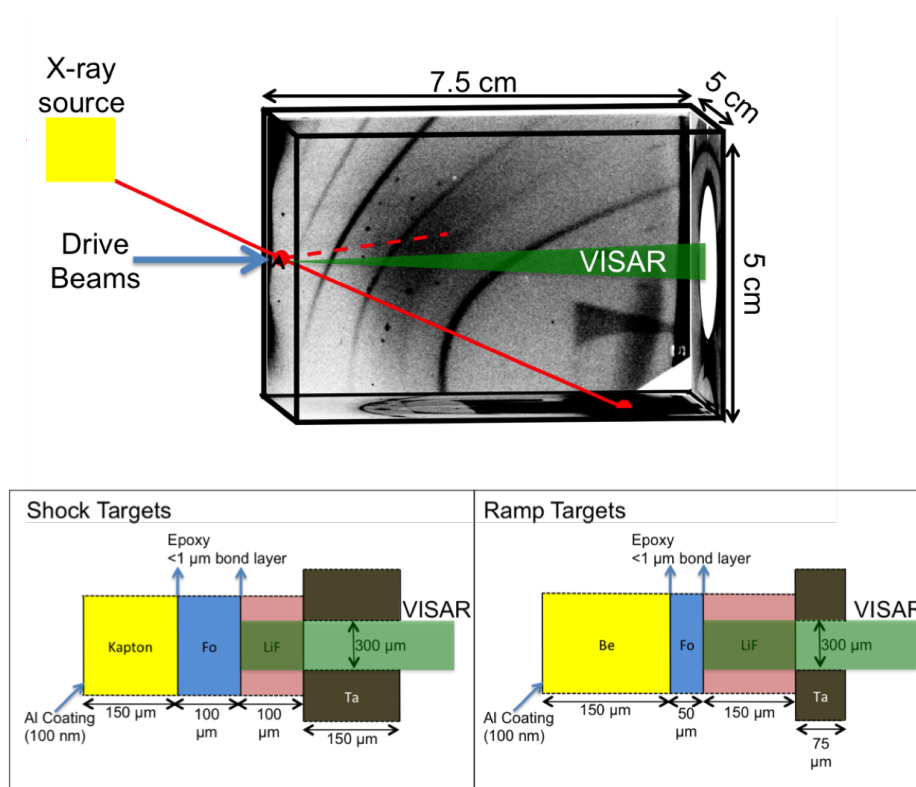
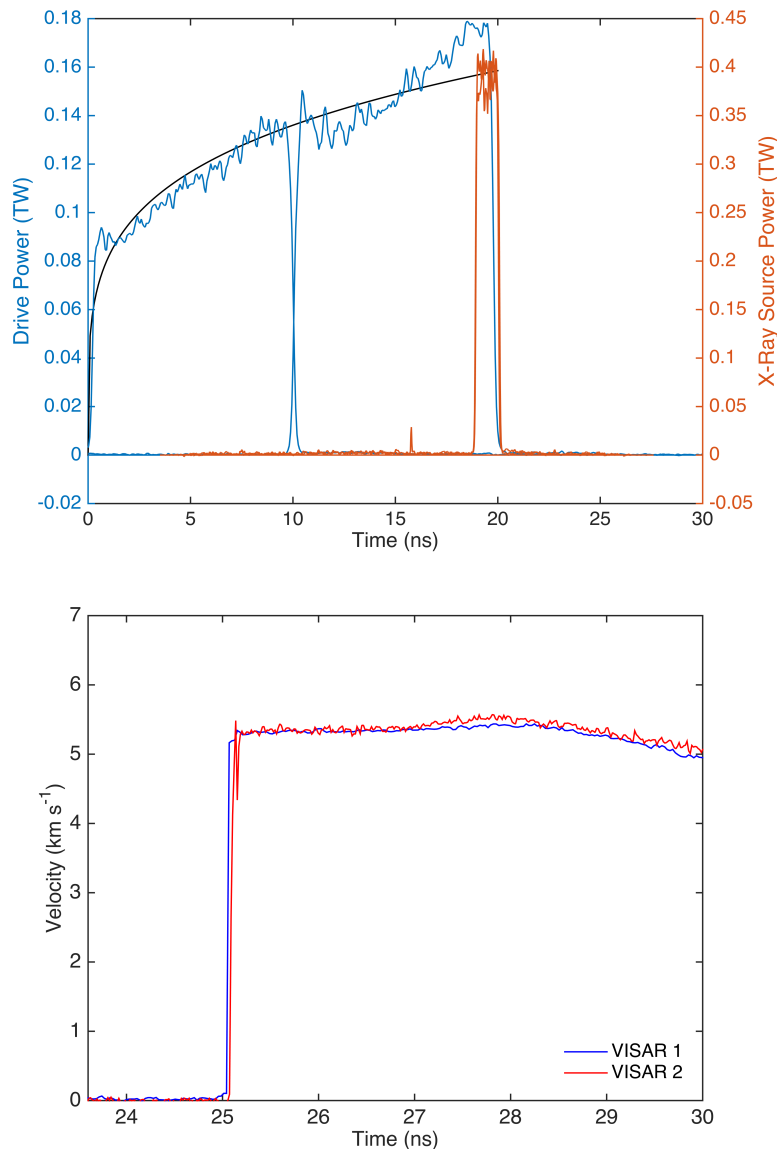


Figure 3.2: **Experimental setup.** Top: Schematic diagram of the diffraction detector (PXRDIIP box) where x-rays are collected on image plates which line the sides of a  $5 \times 5 \times 7.5 \text{ cm}^3$  box. The solid red line shows the straight through x-ray path and the dashed line shows the path of x-rays scattered by the sample. The VISAR path is down range of the sample. Bottom: Schematic diagram of the target packages for shock and ramp experiments. The VISAR is incident upon the forsterite/LiF interface. A 75 or 150  $\mu\text{m}$  thick Ta pinhole with 300  $\mu\text{m}$  diameter aperture is used to collimate the x-rays and calibrate the detector geometry.



**Figure 3.3: Timing of shock compression experiment for shot 21922.** Top: representative laser pulse shape for the beams that drives the sample (left axis) and the beams that drive the x-ray backlighter (right axis). The ramping of intensity in the laser drive pulse shape compensates for adiabatic cooling due to expansion of the plasma plume which would otherwise generate a decaying shock. The steepening of the laser pulse relative to the ideal laser pulse shape (black) starting at 15 ns is responsible for the late time unsteadiness observed in the VISAR profile. Bottom: representative VISAR profile for shock compression experiments. The initial steady velocity plateau is used in the impedance match calculation to determine the shock pressure in the sample. The slight increase in particle velocity at 27 ns is confirmed by hydrodynamic simulations to be due to an inadvertent steepening in the laser pulse shape. The decrease in particle velocity at 28.5 ns is due to a release wave from the ablation surface. The axis range of the VISAR trace starts when the x-ray backlighter beams turn off to show relative timing.

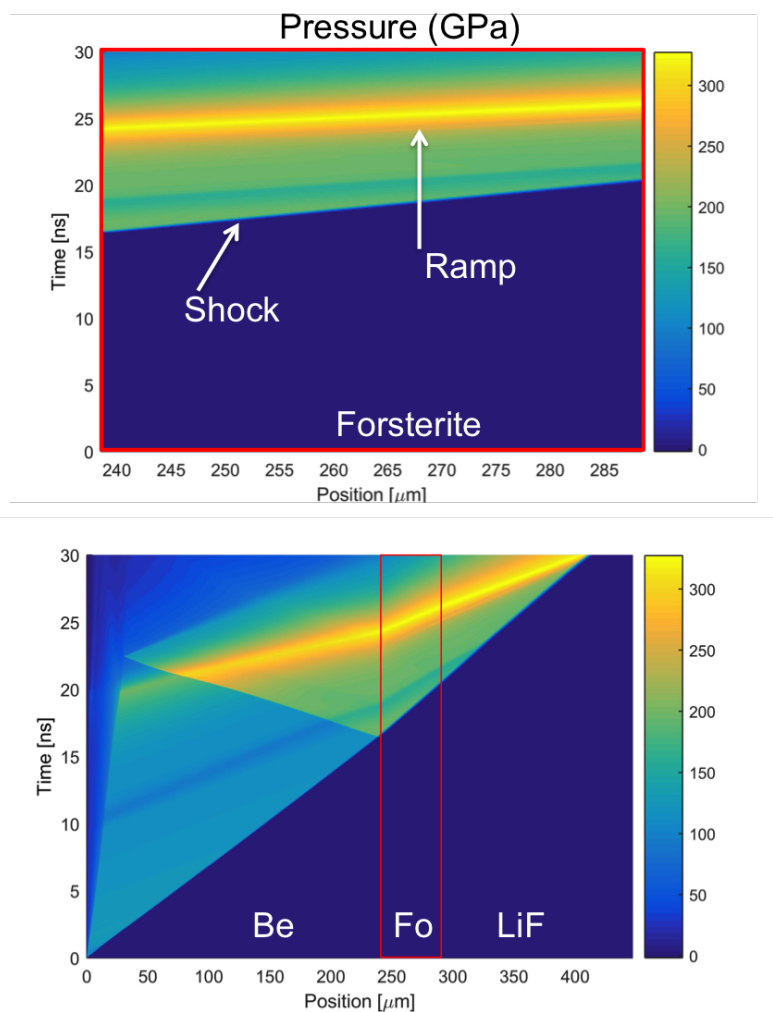


Figure 3.4: Characteristics Diagram for shock-ramp experiments. Bottom: Characteristics plot showing the wave interactions for the shock-ramp experiments calculated using the radiation hydrodynamics code HYADES (Larsen and Lane, 1994). The complete target assembly of Be ablator, forsterite sample, and LiF window is simulated. Top: Wave interactions for just the forsterite region (enclosed in red). The x-ray source is timed to probe the forsterite after the ramp wave has transited the sample.

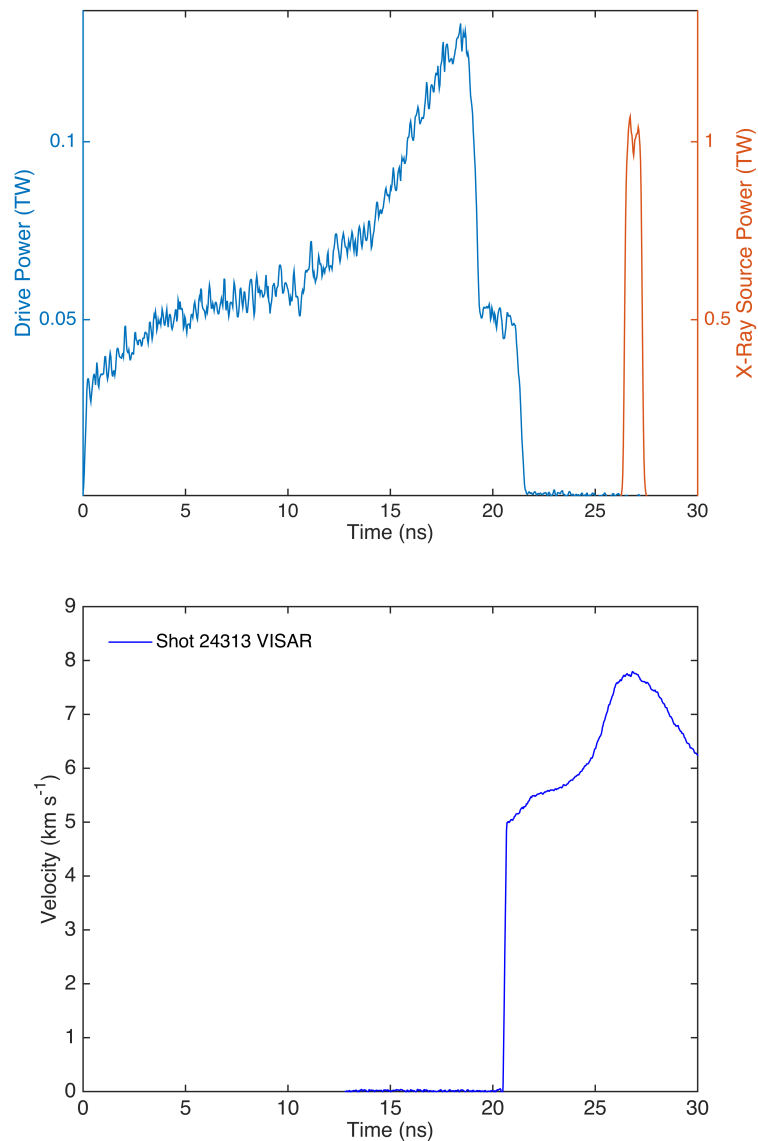


Figure 3.5: **Timing of ramp compression experiment for shot 24313.** Top: representative composite laser pulse for shock-ramp experiments. Three 10 ns laser beams are stacked sequentially in time to produce the composite shock and ramp pulse (left axis). The single 3-ns laser pulse that illuminates the Cu foil and thereby generates the x-ray source is plotted on the right axis. Bottom: Measured velocity at the interface between the forsterite sample and LiF window. The ramp wave enters the LiF at  $\sim 23.5$  ns and gradually ramps to the maximum velocity over a period of  $\sim 2.5$  ns, indicating shockless compression of the forsterite sample. The x-ray source is timed so that the sample is probed after the ramp wave has transited the sample. The decrease in velocity observed at 27 ns is due to release associated with laser turn off.

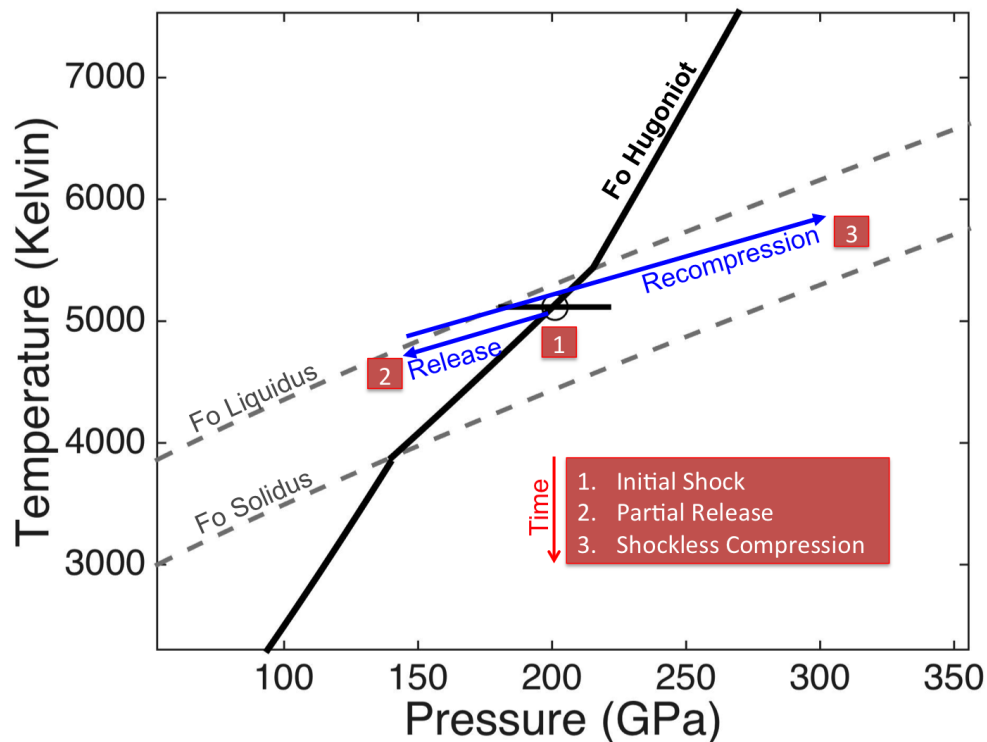


Figure 3.6: **Thermodynamic path for the shock-melt ramp-resolidification experiments.** The forsterite sample is first shocked to a point on the Hugoniot between the solidus and the liquidus, determined from single shock measurements (state 1). Subsequently, the sample partially releases at constant entropy into a LiF window, a process which further drives the sample towards the liquidus (state 2). Finally, the sample is shocklessly compressed back across the liquidus where it is probed with x-rays (state 3).

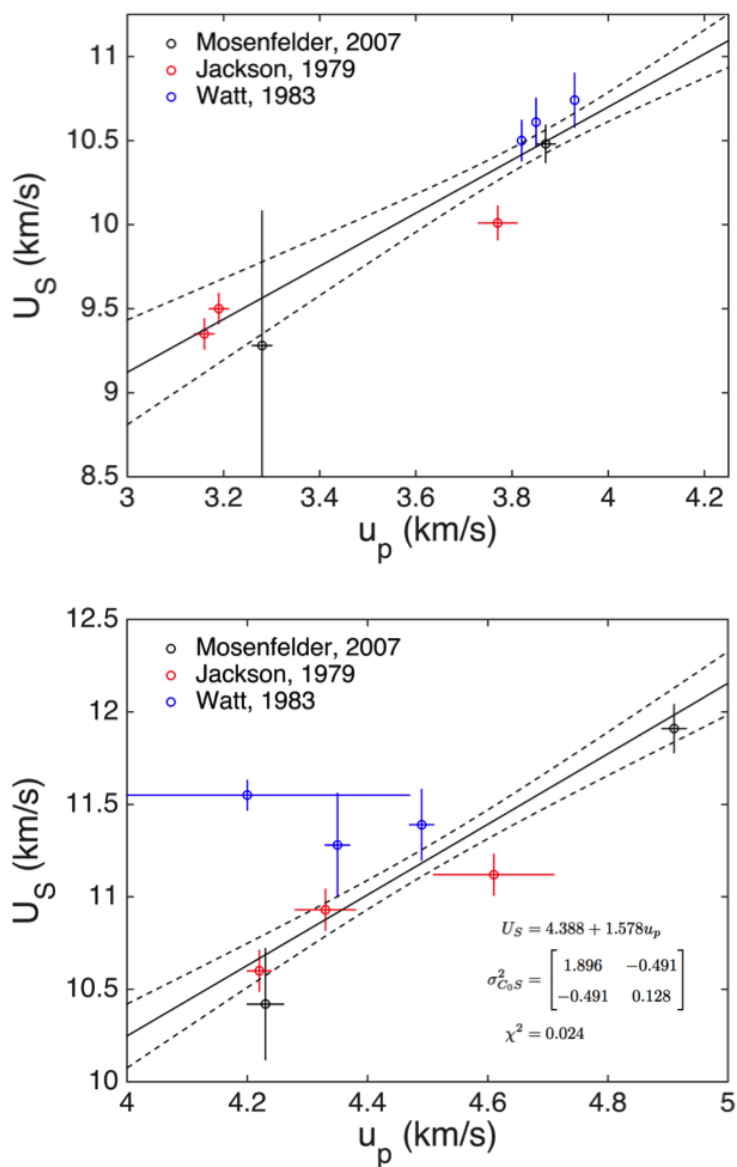


Figure 3.7: **Forsterite Hugoniot between 90 GPa and 140 GPa.** Selected  $U_S - u_p$  data for forsterite in the solid high pressure phase region (top) and the partial melt regime (bottom) (Mosenfelder, Asimow, and Ahrens, 2007; Jackson and Ahrens, 1979; Watt and Ahrens, 1983). To account for the large disparity in the errors associated with each data point, the data are linearly fit using a total least squares approach that includes uncertainties in both the particle and shock velocity (Krystek and Anton, 2007; Ruoff, 1967). The linear fits are used to infer the shock pressure in the sample from the LiF interface velocity through the standard impedance matching technique (Zeldovich and Raizer, 1965).

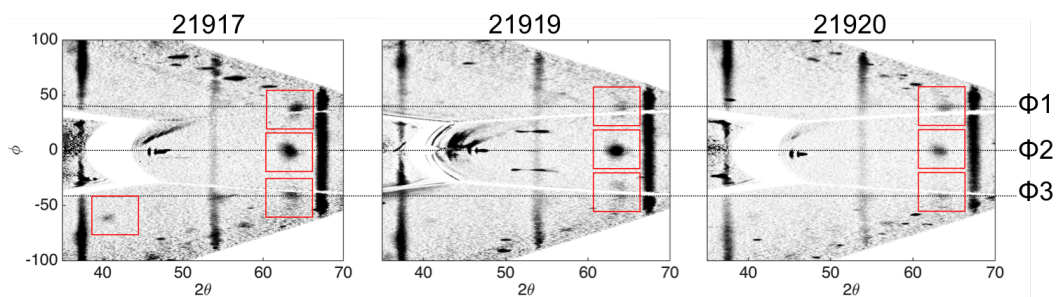


Figure 3.8: Diffraction data collected for shock compression to 125 GPa. The raw image files are dewarped into  $\phi - 2\theta$  space. Diffraction identified as coming from the shock sample is boxed in red. In each experiment, we observe three distinct Bragg peaks at  $64^\circ$  that correspond to crystal planes rotated  $33^\circ$  with respect to one another. This indicates that the microstructure induced by shock compression is consistent in each experiment and may suggest twinning.

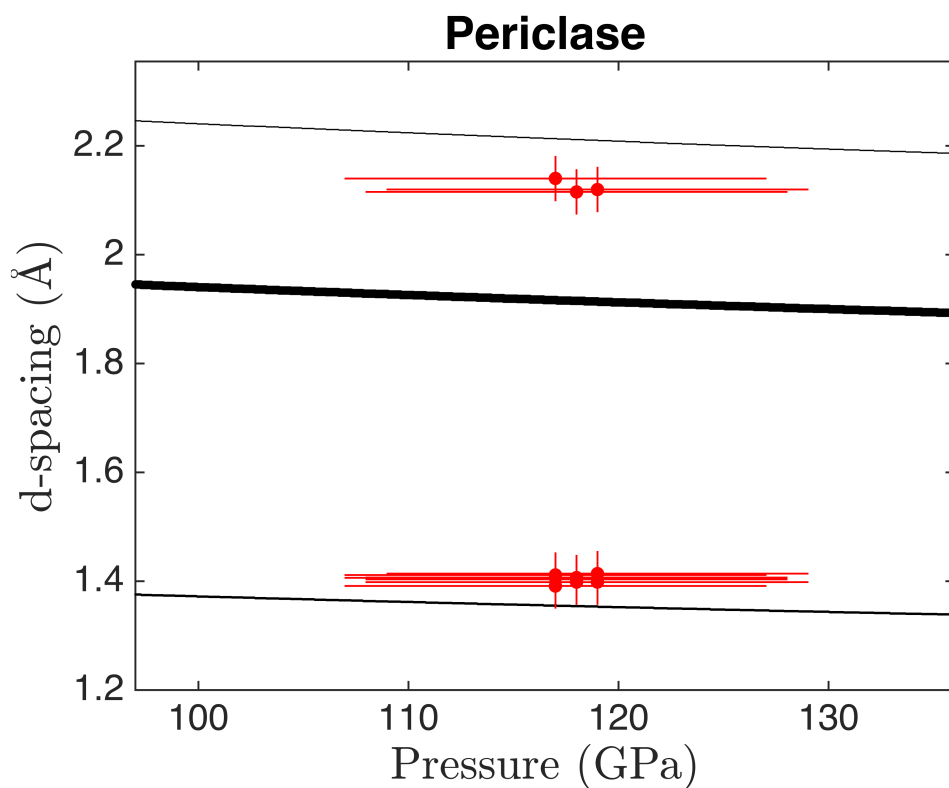


Figure 3.9: The observed d-spacing is plotted as a function of Hugoniot pressure and compared to the expected diffraction peak positions for periclase at the relevant thermodynamic condition (Tange, Nishihara, and Tsuchiya, 2009; Wu et al., 2008). The line width denotes the relative intensity of the diffraction peaks; however due to the texture of the sample relative peak intensities or the absence of a diffraction peak cannot be used to rule out a structure. The peaks that we interpreted as solid diffraction from the shocked sample are plotted as red circles. The observed diffraction peaks do not match the expected peak location for periclase, and so we rule out periclase as a structure.

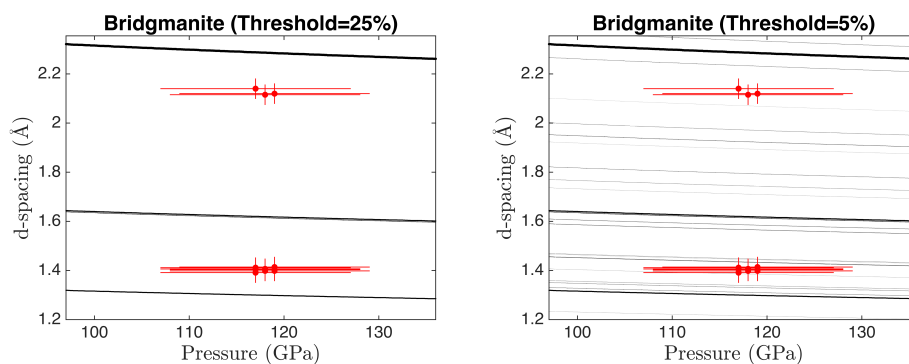


Figure 3.10: The observed d-spacing is plotted as a function of Hugoniot pressure and compared to the expected diffraction peaks for bridgmanite at the relevant thermodynamic condition (Tange, Kuwayama, et al., 2012; Fiquet, Andrault, et al., 1998; Fiquet, Dewaele, et al., 2000). Diffraction peaks are plotted if they fall above a threshold intensity of 25% (left) and 5% (right) of the most intense diffraction peak for the bridgmanite structure. The peaks interpreted as solid diffraction from the shocked sample are plotted as red circles. Diffraction is not expected at 2.2 Å and 125 GPa for the bridgmanite structure, so we rule it out as a candidate.

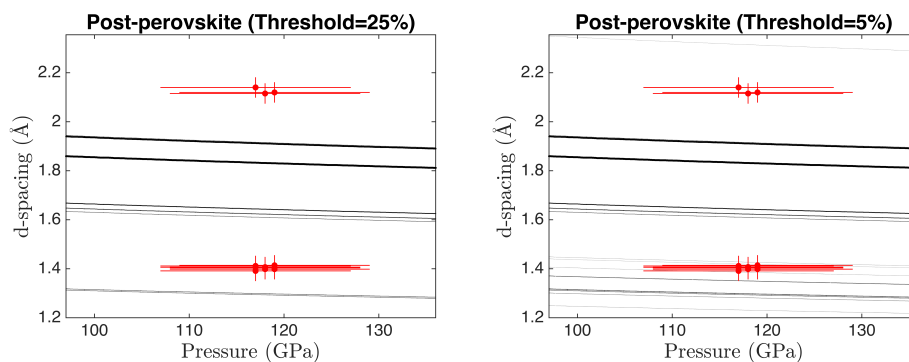


Figure 3.11: The observed d-spacing is plotted as a function of Hugoniot pressure and compared to the expected diffraction peaks for post-perovskite at the relevant thermodynamic condition Sakai, Dekura, and Hirao, 2016; Murakami et al., 2004. Diffraction peaks are plotted if they fall above a threshold intensity of 25% (left) and 5% (right) of the most intense diffraction peak for the post-perovskite structure. The peaks interpreted as solid diffraction from the shocked sample are plotted as red circles. Diffraction is not expected at 2.2 Å and 125 GPa for the post-perovskite structure, so we rule it out as a candidate.

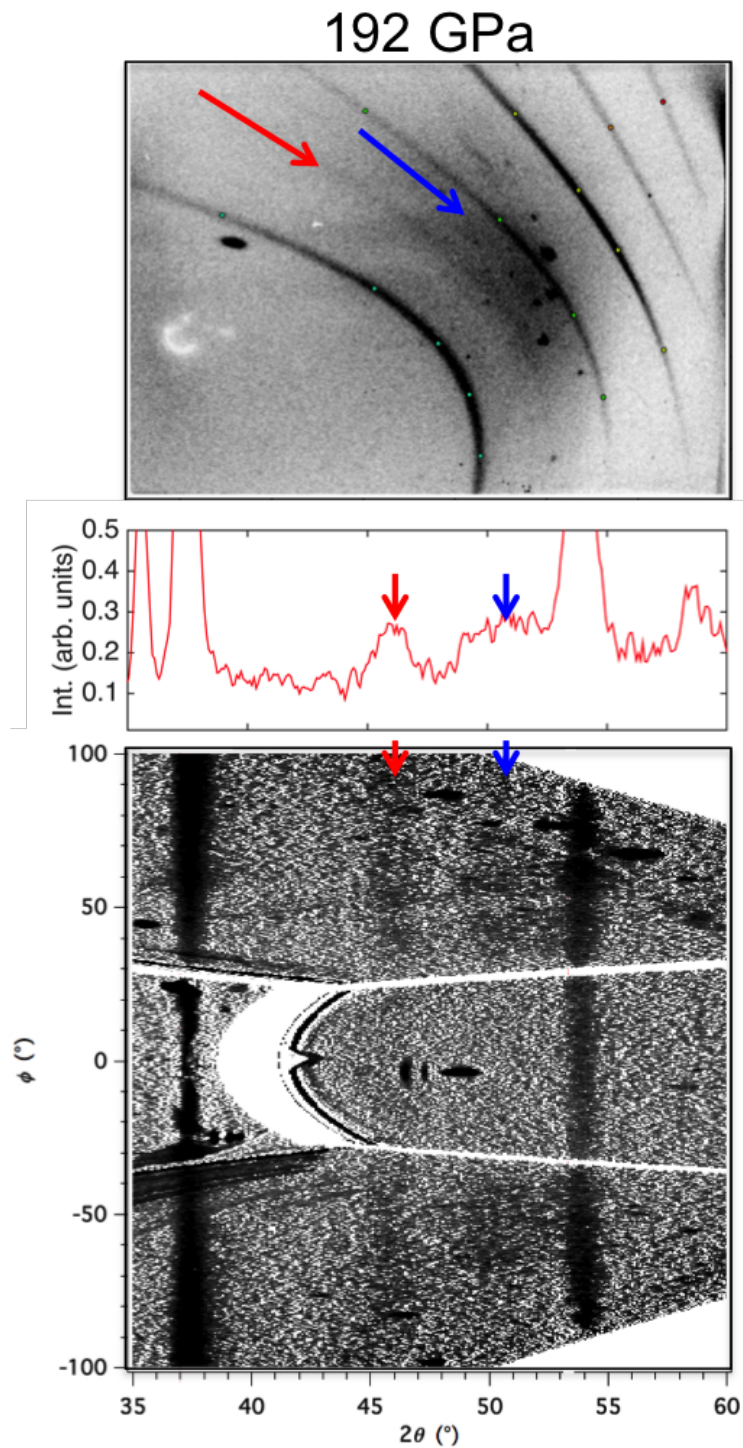


Figure 3.12: **Diffraction data for partially molten forsterite.** Raw (top) and processed (bottom) diffraction data for forsterite shocked into the partial melt regime. In this Hugoniot region, we observe two features associated with diffraction from the forsterite sample; a sharp peak which we assign to periclase (red arrow) and a broad peak characteristic of diffuse scattering from a liquid (blue arrow). In this illustration, we show the raw diffraction data (top), a lineout of the de-warped diffraction data (middle), and the de-warped diffraction data (bottom).

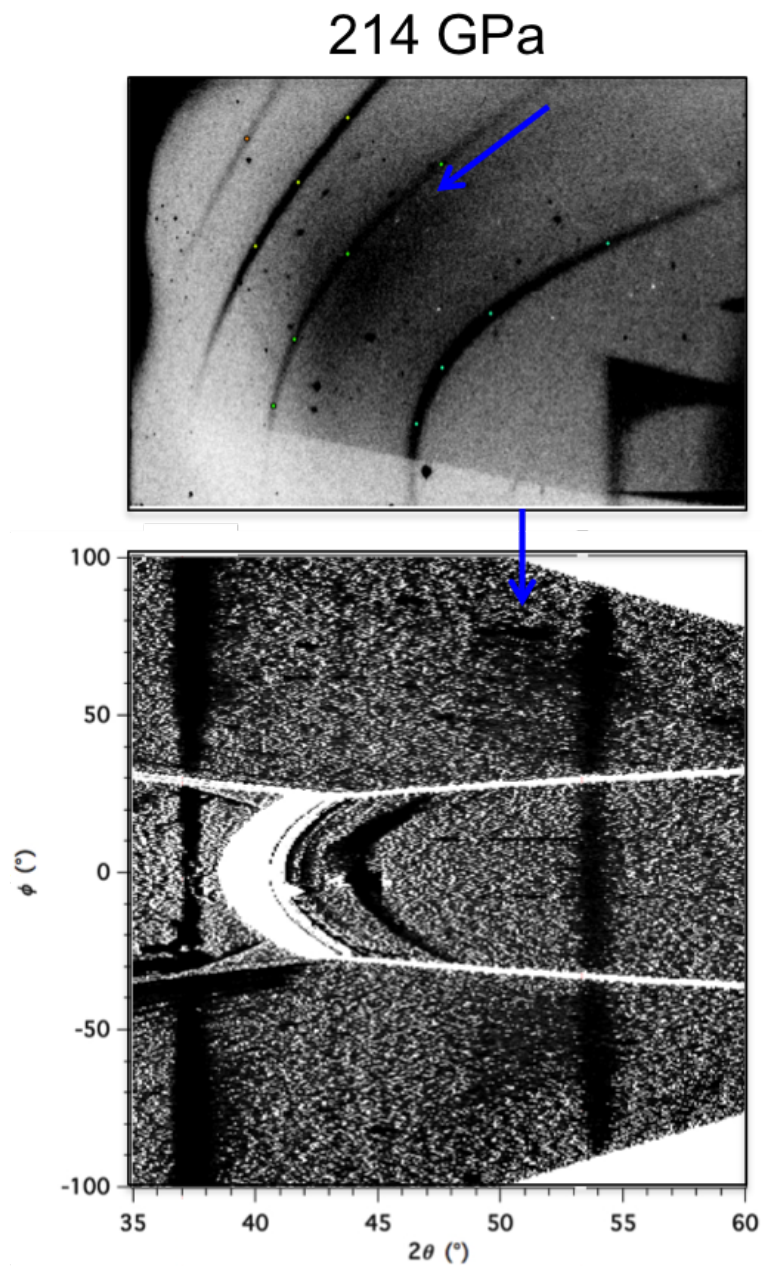


Figure 3.13: Raw (top) and processed (bottom) diffraction data for shock compression to 214 GPa. The processed diffraction data has been dewarped in to  $\phi - 2\theta$  space and background subtracted. In this Hugoniot region, we only observe diffuse liquid scattering.

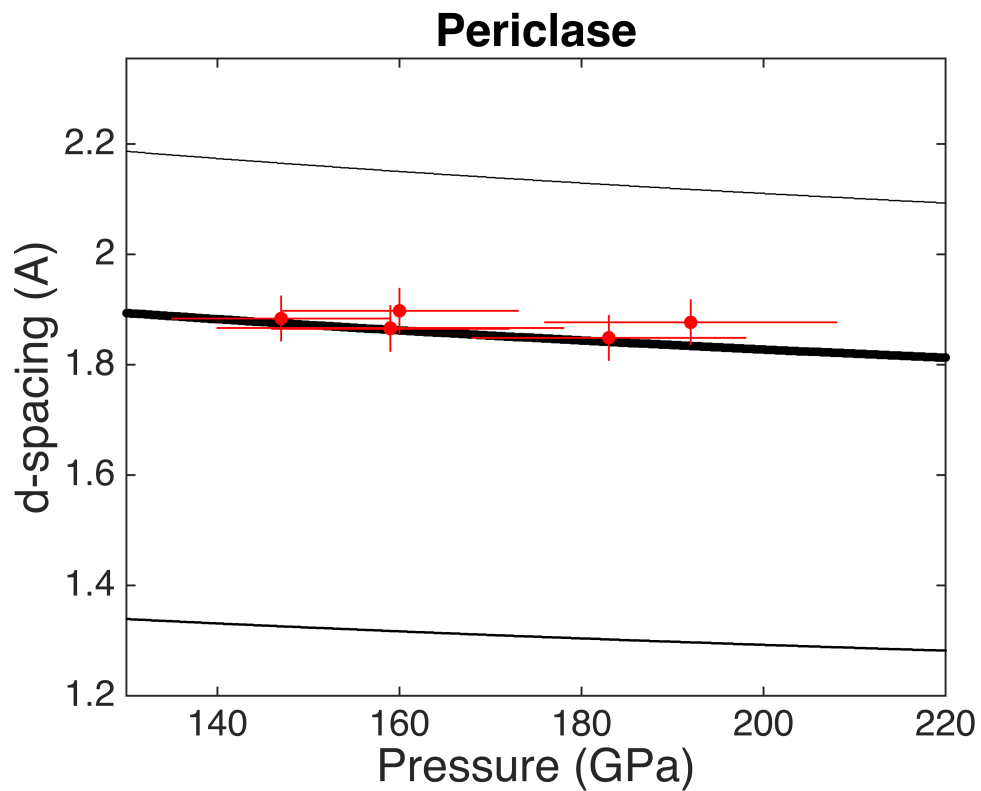


Figure 3.14: The observed d-spacing is plotted as a function of Hugoniot pressure and compared to the expected diffraction peaks for periclase at the relevant thermodynamic condition Fiquet, Andrault, et al., 1998; Fiquet, Dewaele, et al., 2000. The peaks interpreted as solid diffraction based on peak width are plotted as red circles.

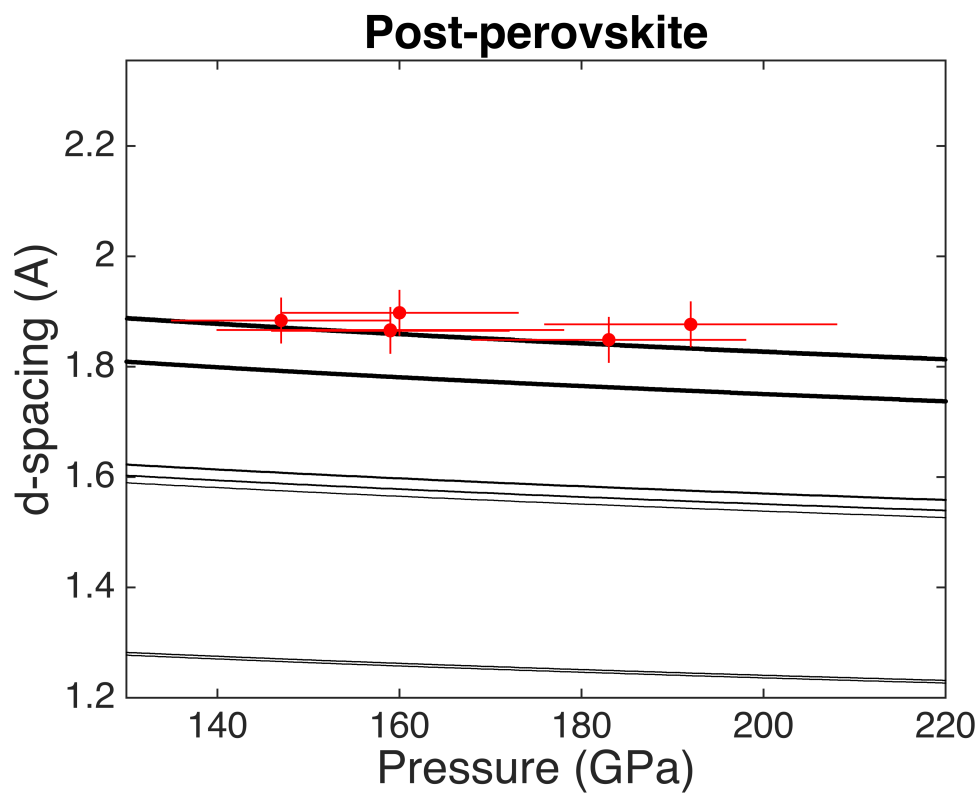


Figure 3.15: The observed d-spacing is plotted as a function of Hugoniot pressure and compared to the expected diffraction peaks for post-perovskite at the relevant thermodynamic condition Sakai, Ohtani, et al., 2011; Murakami et al., 2004. While the peak we observe does match a diffraction peak of post-perovskite, we rule out this structure because under powder diffraction we do not observe any of the other post-perovskite peaks.

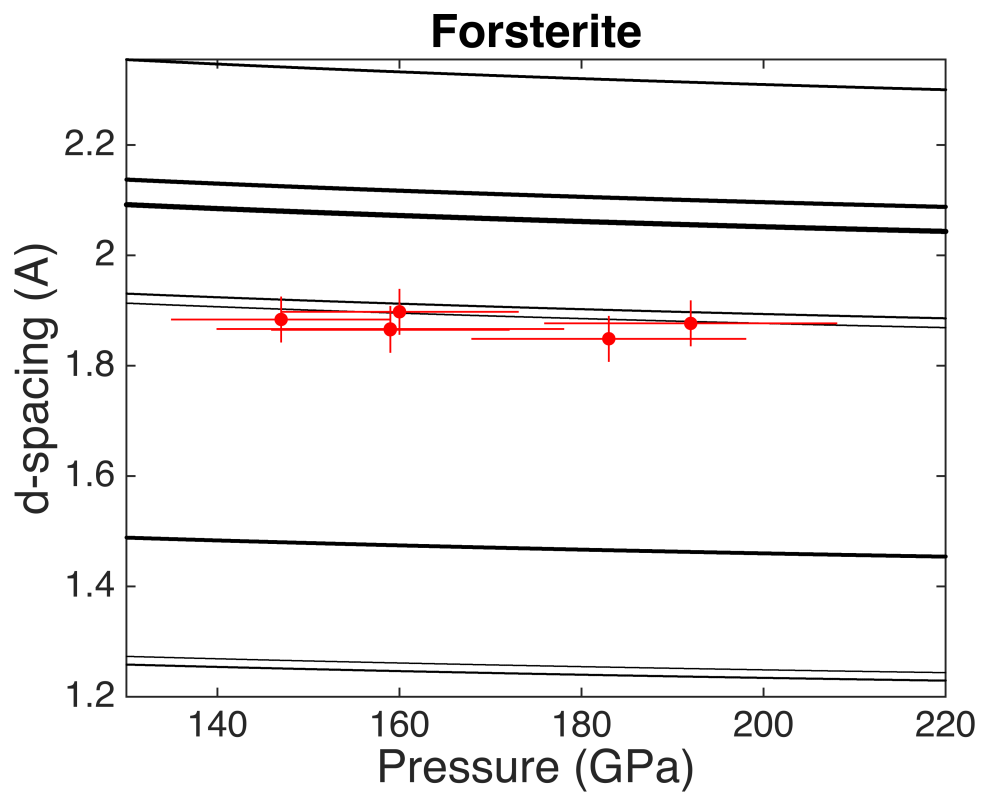


Figure 3.16: The observed d-spacing is plotted as a function of Hugoniot pressure and compared to the expected diffraction peaks for forsterite with a threshold intensity greater than 25% at the Hugoniot density. We rule out the forsterite structure because we do not observe the more intense forsterite peaks expected at roughly 2.1 and 1.5 .

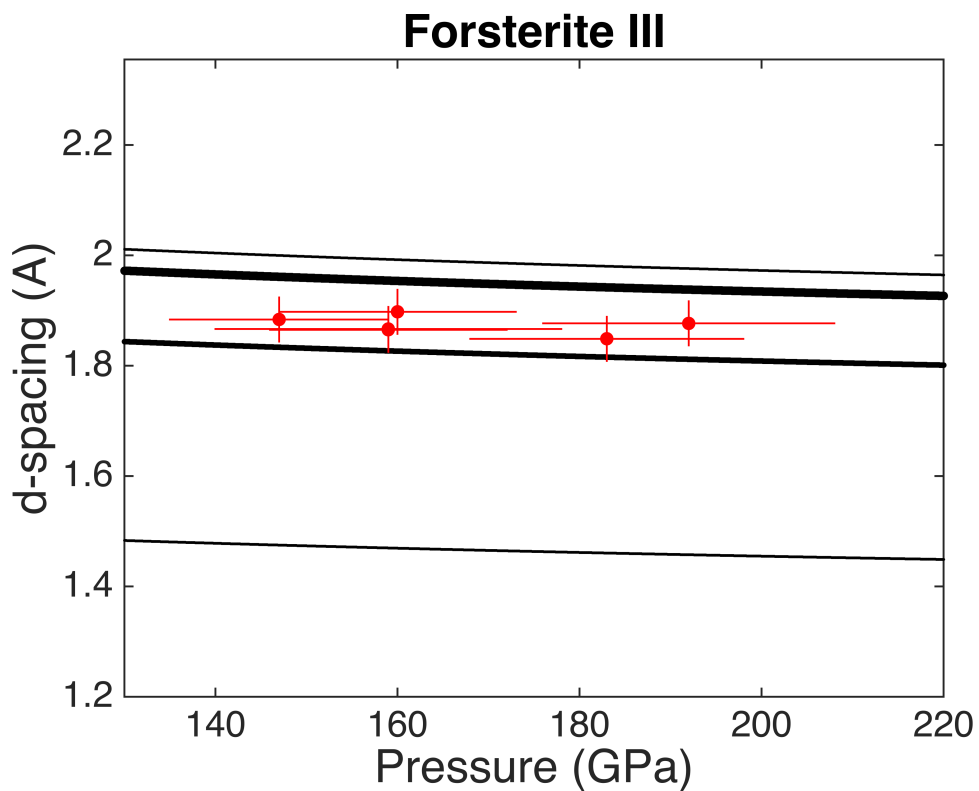


Figure 3.17: The observed d-spacing is plotted as a function of Hugoniot pressure and compared to the expected diffraction peaks for forsterite III with a threshold intensity greater than 25% at the forsterite Hugoniot density (Finkelstein et al., 2014). We rule out the forsterite III structure because under powder diffraction we do not observe any of the most intense forsterite III diffraction peaks.

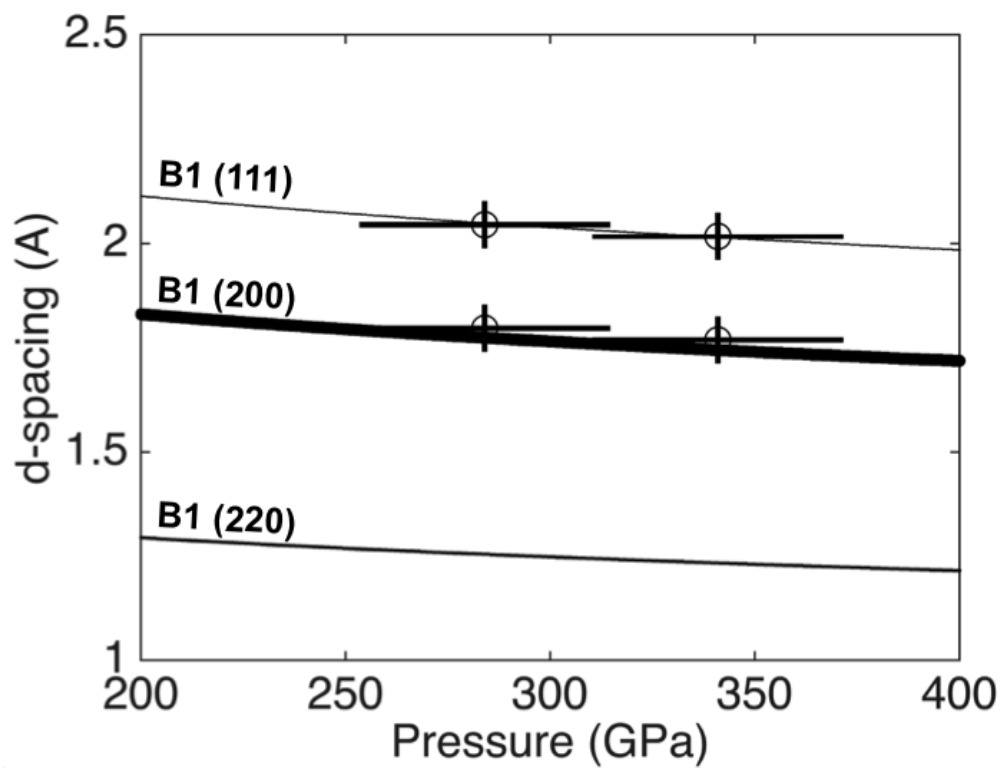


Figure 3.18: The observed d-spacing is plotted as a function of ramp pressure and compared to the expected diffraction peaks for periclase at the relevant thermodynamic condition.

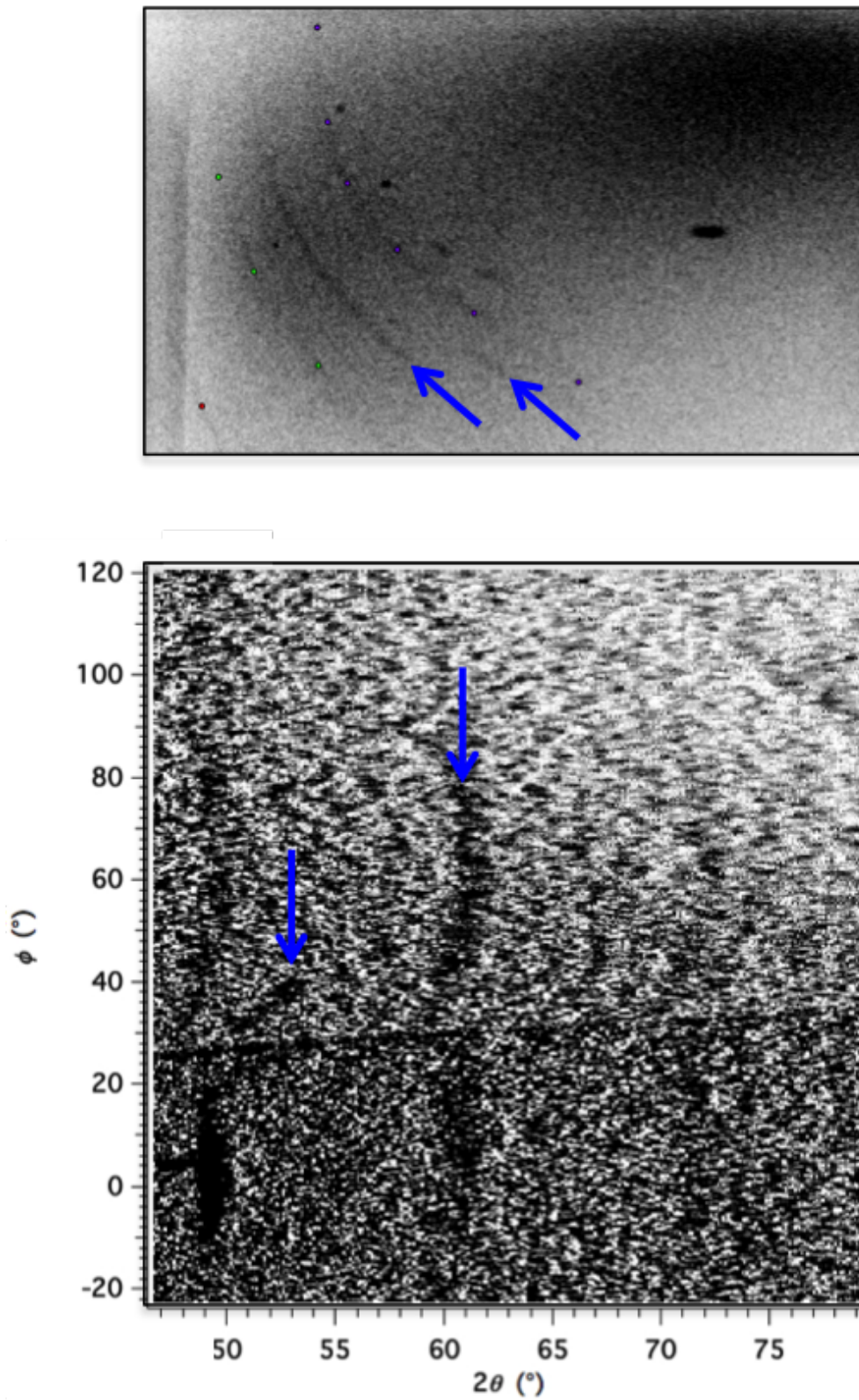


Figure 3.19: Raw (top) and processed (bottom) diffraction data for ramp compression to 284(28) GPa. The processed diffraction data has been dewarped in to  $\phi - 2\theta$  space and background subtracted. Peaks indexed as periclase are indicated by blue arrows.

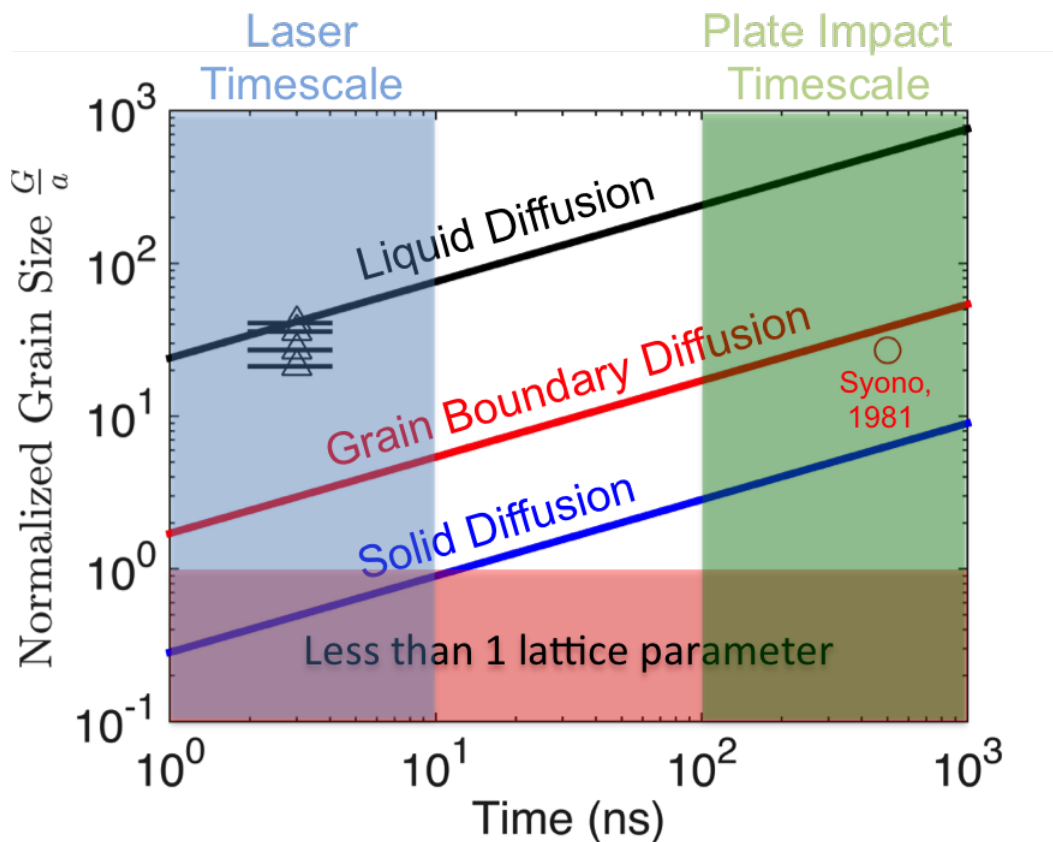


Figure 3.20: Plot of log grain diameter normalized by the lattice parameter of MgO as a function of log time (Syono, Goto, Takei, et al., 1981; H. Fei, 2013; De Koker, Stixrude, and Karki, 2008; Farver, Yund, and Rubie, 1994). The region shaded in red corresponds to grain sizes less than one lattice parameter of MgO and the region shaded in blue corresponds to the timescale of the experiments performed in this work. The black data points are lower bounds on the grain size for B1 MgO in the partial melt region of the Hugoniot calculated from the Scherrer equation.

## References

- Asimow, P. (2017). “A measure of mantle melting”. In: *Science* 355, pp. 908–909.
- Brown, M., M. Furnish, and D. Boness (1987). “Sound velocities for San Carlos olivine”. In: *Shock Waves in Condensed Matter*, pp. 119–122.
- Celliers, P. et al. (2013). “Line-imaging Velocimetry for Shock Diagnostics (VISAR)”. In: *CLEO: Applications and Technology*. Optical Society of America, ATu3M–2.
- De Koker, N., B. Karki, and L. Stixrude (2013). “Thermodynamics of the MgO-SiO<sub>2</sub> liquid system in Earth’s lowermost mantle from first principles”. In: *Earth and Planetary Science Letters* 361, pp. 58–63.
- De Koker, N. and L. Stixrude (2009). “Self-consistent thermodynamic description of silicate liquids, with application to shock melting of MgO periclase and MgSiO<sub>3</sub> perovskite”. In: *Geophysical Journal International* 178.1, pp. 162–179.
- De Koker, N., L. Stixrude, and B. Karki (2008). “Thermodynamics, structure, dynamics, and freezing of Mg<sub>2</sub>SiO<sub>4</sub> liquid at high pressure”. In: *Geochimica et Cosmochimica Acta* 72, pp. 1427–1441.
- Farver, J., R. Yund, and D. Rubie (1994). “Magnesium grain boundary diffusion in forsterite aggregates at 1000–1300 C and 0.1 MPa to 10 GPa”. In: *Journal of Geophysical Research: Solid Earth* 99.B10, pp. 19809–19819.
- Fei, H. (2013). “Silicon and oxygen self-diffusion in forsterite and implications to upper-mantle rheology”. PhD thesis.
- Fei, Y. et al. (2004). “Experimentally determined postspinel transformation boundary in Mg<sub>2</sub>SiO<sub>4</sub> using MgO as an internal pressure standard and its geophysical implications”. In: *Journal of Geophysical Research: Solid Earth* 109.B2.
- Finkelstein, G. et al. (2014). “Phase transitions and equation of state of forsterite to 90 GPa from single-crystal X-ray diffraction and molecular modeling”. In: *American Mineralogist* 99.1, pp. 35–43.
- Fiquet, G., D. Andrault, et al. (1998). “PVT equation of state of MgSiO<sub>3</sub> perovskite”. In: *Physics of the Earth and Planetary Interiors* 105.1-2, pp. 21–31.
- Fiquet, G., A. Dewaele, et al. (2000). “Thermoelastic properties and crystal structure of MgSiO<sub>3</sub> perovskite at lower mantle pressure and temperature conditions”. In: *Geophysical Research Letters* 27.1, pp. 21–24.
- Furnish, M. and M. Brown (1986). “Shock loading of single-crystal olivine in the 100–200 GPa range”. In: *Journal of Geophysical Research: Solid Earth* 91.B5, pp. 4723–4729.
- Gleason, A et al. (2015). “Ultrafast visualization of crystallization and grain growth in shock-compressed SiO<sub>2</sub>”. In: *Nature communications* 6.
- Hanks, T. and D. Anderson (1969). “The early thermal history of the Earth”. In: *Physics of the Earth and Planetary Interiors* 2.1, pp. 19–29.

- Hawreliak, J et al. (2007). “High pressure nano-crystalline microstructure of shock compressed single crystal iron”. In: *Physical Review B* 78.UCRL-JRNL-237258.
- J. Nguyen, et al. (2004). “Specifically prescribed dynamic thermodynamic paths and resolidification experiments”. In: vol. 706. 1. AIP, pp. 1225–1230.
- Jackson, I. and T. Ahrens (1979). “Shock-wave compression of single crystal forsterite”. In: *Journal of Geophysical Research* 84, pp. 3039–3048.
- Jeanloz, R. (1980). “Shock effects in olivine and implications for Hugoniot data”. In: *Journal of Geophysical Research: Solid Earth* 85.B6, pp. 3163–3176.
- K. Umemoto R.M. Wentzcovitch, P.B. Allen (2006). “Dissociation of MgSiO<sub>3</sub> in the cores of gas giants and terrestrial exoplanets”. In: *Science* 311.5763, pp. 983–986.
- Krystek, M. and M. Anton (2007). “A weighted total least-squares algorithm for fitting a straight line”. In: *Measurement Science and Technology* 18.11, p. 3438.
- Larsen, J. and S. Lane (1994). “HYADES—A plasma hydrodynamics code for dense plasma studies”. In: *Journal of Quantitative Spectroscopy and Radiative Transfer* 51, pp. 179–186.
- Luo, S-N, T. Akins J.and Ahrens, and P. Asimow (2004). “Shock-compressed Mg-SiO<sub>3</sub> glass, enstatite, olivine, and quartz: Optical emission, temperatures, and melting”. In: *Journal of Geophysical Research: Solid Earth* 109.B5.
- Lyzenga, G. and T. Ahrens (1980). “Shock temperature measurements in Mg<sub>2</sub>SiO<sub>4</sub> and SiO<sub>2</sub> at high pressures”. In: *Geophysical Research Letters* 7.2, pp. 141–144.
- Meyerhofer, D. et al. (2010). “Performance of and initial results from the OMEGA EP Laser System”. In: *Journal of Physics: Conference Series*. Vol. 244. 3.
- Mosenfelder, J., P. Asimow, and T. Ahrens (2007). “Thermodynamic properties of Mg<sub>2</sub>SiO<sub>4</sub> liquid at ultra-high pressures from shock measurements to 200 GPa on forsterite and wadsleyite”. In: *Journal of Geophysical Research: Solid Earth* 112.
- Murakami, M. et al. (2004). “Post-perovskite phase transition in MgSiO<sub>3</sub>”. In: *Science* 304.5672, pp. 855–858.
- Osako, M., E. Ito, and A. Yoneda (2004). “Simultaneous measurements of thermal conductivity and thermal diffusivity for garnet and olivine under high pressure”. In: *Physics of the Earth and Planetary Interiors* 143, pp. 311–320.
- Patterson, A. (1939). “The Scherrer formula for X-ray particle size determination”. In: *Physical review* 56.10, p. 978.
- Presnall, D. et al. (1998). “Liquidus phase relations in the system MgO–MgSiO<sub>3</sub> at pressures up to 25 GPa—constraints on crystallization of a molten Hadean mantle”. In: *Physics of the Earth and Planetary Interiors* 107.1, pp. 83–95.
- Rigg, P. et al. (2014). “Determining the refractive index of shocked [100] lithium fluoride to the limit of transmissibility”. In: *Journal of Applied Physics* 116.

- Ruoff, A. (1967). "Linear Shock-Velocity-Particle-Velocity Relationship". In: *Journal of Applied Physics* 38.13, pp. 4976–4980.
- Rygg, R. et al. (2012). "Powder diffraction from solids in the terapascal regime". In: *Review of Scientific Instruments* 83.
- Sakai, T., H. Dekura, and N. Hirao (2016). "Experimental and theoretical thermal equations of state of MgSiO<sub>3</sub> post-perovskite at multi-megabar pressures". In: *Scientific reports* 6, p. 22652.
- Sakai, T., E. Ohtani, et al. (2011). "Stability field of the hcp-structure for Fe, Fe-Ni, and Fe-Ni-Si alloys up to 3 Mbar". In: *Geophysical research letters* 38.9.
- Shim, S.-H., T. Duffy, and G. Shen (2001). "The post-spinel transformation in Mg<sub>2</sub>SiO<sub>4</sub> and its relation to the 660 km seismic discontinuity". In: *Nature* 411, pp. 571–574.
- Swift, D. and G. Kraus (2008). "Properties of plastic ablaters in laser-driven material dynamics experiments". In: *Physical Review E* 77.6.
- Syono, Y., T. Goto, J.-I. Sato, et al. (1981). "Shock compression measurements of single-crystal forsterite in the pressure range 15–93 GPa". In: *Journal of Geophysical Research: Solid Earth* 86.B7, pp. 6181–6186.
- Syono, Y., T. Goto, H. Takei, et al. (1981). "Dissociation reaction in forsterite under shock compression". In: *Science* 214.4517, pp. 177–179.
- Tang, X. and J. Dong (2010). "Lattice thermal conductivity of MgO at conditions of Earth's interior". In: *Proceedings of the National Academy of Sciences* 107.10, pp. 4539–4543.
- Tange, Y., Y. Kuwayama, et al. (2012). "P-V-T equation of state of MgSiO<sub>3</sub> perovskite based on the MgO pressure scale: A comprehensive reference for mineralogy of the lower mantle". In: *Journal of Geophysical Research: Solid Earth* 117.B6.
- Tange, Y., Y. Nishihara, and T. Tsuchiya (2009). "Unified analyses for P-V-T equation of state of MgO: A solution for pressure-scale problems in high P-T experiments". In: *Journal of Geophysical Research: Solid Earth* 114.B3.
- Tonks, W Brian and H Jay Melosh (1993). "Magma ocean formation due to giant impacts". In: *Journal of Geophysical Research: Planets* 98.E3, pp. 5319–5333.
- Urey, H. (1955). "The cosmic abundances of potassium, uranium, and thorium and the heat balances of the Earth, the Moon, and Mars". In: *Proceedings of the National Academy of Sciences* 41.3, pp. 127–144.
- Wett, J. and T. Ahrens (1983). "Shock compression of single-crystal forsterite". In: *Journal of Geophysical Research: Solid Earth* 88.B11, pp. 9500–9512.
- Wu, Z. et al. (2008). "Pressure-volume-temperature relations in MgO: An ultrahigh pressure-temperature scale for planetary sciences applications". In: *Journal of Geophysical Research: Solid Earth* 113.B6.

- Y. Syono, T. Goto (1982). "Behavior of single-crystal forsterite under dynamic compression". In: *High-Pressure Research in Geophysics* 12, pp. 563–578.
- Zeldovich, Y. and Y. Raizer (1965). *Physics of shock waves and high-temperature hydrodynamic phenomena*. Tech. rep. FOREIGN TECHNOLOGY DIV WRIGHT-PATTERSON AFB OH.

*Chapter 4*COMPRESSION OF IRON SILICIDE AT EARTH CORE  
CONDITIONS ON NANOSECOND TIMESCALES**4.1 Introduction**

Modeling the interior structure and dynamics of cores of terrestrial planets requires knowledge of the equation of state and phase diagram of the relevant geological materials at core thermodynamic conditions (Hirose, Labrosse, and Herlund, 2013; Morard et al., 2014). On the Earth pressures and temperatures range from 136 GPa and  $\sim 3500$  K at the core mantle boundary to 363 GPa and  $\sim 5500$  K in the inner core. From geophysical constraints obtained from seismic data, the core of the Earth is underdense compared to pure iron (Duffy, 2005; Birch, 1952; Birch, 1964; Poirier, 1994). Understanding how the addition of light alloying elements affects the phase diagram is essential to improving our understanding of the interior of the Earth. As examples, the melting temperature at the inner core boundary (ICB) provides an anchor point for the temperature profile of the Earth and light element rejection upon solidification at the ICB may be the driving source for convection in the outer core. Therefore, freezing point depression due to the entropy of mixing with a light element may dramatically alter models of the temperature profile of the Earth. In recent years, Fe-Si alloys of varying Si composition have been investigated to understand how the addition of light elements effects the phase diagram and melting behavior at core pressures (Lin, Campbell, et al., 2003; Hirao et al., 2004; Asanuma, Ohtani, Sakai, Terasaki, S Kamada, et al., 2008; Asanuma, Ohtani, Sakai, Terasaki, S. Kamada, Kondo, et al., 2010; Asanuma, Ohtani, Sakai, Terasaki, S. Kamada, Hirao, et al., 2011; Sakai et al., 2011; Fischer, Campbell, Reaman, et al., 2013; Fischer, Campbell, Caracas, Reaman, Dera, et al., 2012; Fischer, Campbell, Caracas, Reaman, Heinz, et al., 2014).

Pure iron has the *hcp* structure at Earth's inner core conditions, but the addition of silicon allows for more complicated behavior as the number of compositionally distinct phases that can exist in equilibrium increases with each material component

---

This chapter is in preparation for submission with Richard G. Kraus, June K. Wicks, Raymond F. Smith, Thomas S. Duffy, Paul D. Asimow, and Jon H. Eggert.

in the system (Tateno et al., 2010). Laser-heated diamond anvil cell (LDAC) experiments to 150 GPa by Fischer et al. show that at elevated pressure, the ambient  $D0_3$  structure of Fe with 16 wt% Si decomposes into an *hcp* structure and a *B2* (ordered *bcc*) structure (Fischer, Campbell, Caracas, Reaman, Dera, et al., 2012; Fischer, Campbell, Reaman, et al., 2013; Fischer, Campbell, Caracas, Reaman, Heinz, et al., 2014). LDAC recovery experiments on iron with 7.9 weight percent silicon (Fe-7.9Si) show iron segregation, indicating that the *hcp* and *bcc* structures have distinct iron concentrations (Tateno et al., 2010). Iron segregation is further supported by ab-initio evolutionary structure calculations which show that iron silicides ranging in composition from  $\text{Fe}_3\text{Si}$  to  $\text{FeSi}_3$  are unstable to decomposition into  $\text{Fe}+\text{FeSi}$  or  $\text{FeSi}+\text{Si}$  (Zhang and Oganov, 2010). Accordingly, the decomposition of iron silicides into an iron rich *hcp* structure and correspondingly iron-poor *B2* structure is likely a slow process, rate limited by the ionic diffusivity of the solution from which the equilibrium phase assemblage is precipitated. This reaction is necessarily reconstructive, requiring nucleation and growth of new crystals as there is no martensitic pathway to generate compositionally distinct structures (Bhadeshia, 2001; Balluffi, Allen, and Carter, 2005).

These reactions are expected to be slow as they may be rate limited by the solid diffusivity. For growth of nanocrystalline grains (the smallest grains observed during recrystallization of single component materials on nanosecond timescales) and characteristic ionic diffusivities within metals of  $10^{-13} \text{ m}^2 \text{ s}^{-1}$  at temperatures up to 4000 K, the time required for diffusion limited growth of compositionally distinct structures is on the order of  $10^4$  ns based upon dimensional scaling of the diffusivity (Yunker and Van Orman, 2007; J Hawreliak et al., 2007; Gleason et al., 2015). LDAC studies are ideal to measure equilibrium states in systems that undergo chemical segregation because the timescale of the experiment is considerably larger than the timescale for decomposition to occur. While the long timescale of diamond anvil cell platforms is useful for observing slow phenomena, this quality simultaneously makes LDAC measurements sensitive to chemical contamination due to other components in the cell.

Laser-driven compression experiments provide a platform to study iron silicon alloys at the pressures and temperatures that are relevant to the phenomena that occur in the deep interior of the earth, but are subject to the kinetic constraint imposed by the nanosecond duration of the laser pulse. Therefore, laser driven platforms provide insight into the short timescale response of thermodynamic systems that

may undergo chemical segregation. This kinetic response may manifest as single component metastable phases accessible through martensitic pathways or multi-component phases indicating equilibrium is accessible through processes considerably faster than solid diffusion in iron silicide. Importantly, the short duration of the experiment eliminates the problems associated with chemical contamination. As a first step to understanding the path to equilibrium for materials that may undergo decomposition to compositionally distinct structure, we performed laser driven shock compression experiments on an iron silicon alloy with 15 weight percent silicon (Fe-15Si).

## **4.2 Materials and Methods**

### **Laser Driven Shock Compression**

Experiments were carried out at the Omega Laser Facility, which includes a 60-beam laser with up to 500 J per beam (Omega) as well as a 4-beam laser with up to 5000 J per beam (Omega-EP). To generate shock states in the Fe-15Si sample, laser energy was focused to a diameter of 1.8 mm (EP) or 0.8 mm (Omega) onto a kapton ablator. The drive energies used for each shot are reproduced in Table 4.1. Kapton is used as an ablator because it is relatively low  $Z$  and therefore the x-ray emission spectrum from the ablation plasma is relatively soft, allowing it to be attenuated by the ablator itself and not heat the sample or contribute to background noise on the x-ray detector. The ablation process generates an expanding plasma which from conservation of momentum drives a shock in the opposite direction of the expansion (Swift and G. Kraus, 2008). The ablation process continues through the duration of the laser pulse which is up to 4 ns on Omega and 10 ns on EP. The laser energy is ramped upward with time (see Figure 4.1) to compensate for adiabatic cooling due to the expansion of the plasma plume (Swift and G. Kraus, 2008). The intensity of the laser pulse was varied in each shot to generate the range of shock pressures observed in this study and listed in Table 4.1.

### **Target Package**

The Fe-15Si starting material (obtained from ACI Alloys) was characterized by energy-dispersive x-ray spectroscopy (EDS) and found to be chemically homogeneous with a silicon composition of 14.4(2) weight percent. Electron backscatter diffraction (EBSD) measurements indicated randomly oriented grains with a characteristic grain size of 500  $\mu\text{m}$  (Figure 4.2). The ambient crystal density of 7.168  $\text{g cm}^{-3}$  was determined from x-ray diffraction measurements and the bulk density of

7.154(2) g cm<sup>-3</sup> was determined from Archimedean measurements.

The target package consisted of a thin Fe-15Si foil sandwiched between a kapton ablator (GoodFellow Corp.) and lithium fluoride (LiF) window and centered over a W pinhole with a 300 μm diameter aperture as shown in Figure 4.3. For the experiments on EP the nominal target dimensions were 75 μm thick kapton, 20 μm thick Fe-15Si, 100 μm thick LiF, and 150 μm thick W pinhole. For the experiments on Omega the nominal target dimensions were 37.5 μm thick kapton, 15 μm thick Fe-15Si, 100 μm thick LiF, and 75 μm thick W pinhole. The W pinhole is used to collimate the x-rays as well as to calibrate the image plate detector geometry. The pinhole thickness was reduced for the Omega experiments to expand the  $\phi$  coverage of the x-ray detector. The dimensions of the ablator were optimized for each platform so that release from the ablation surface due to the laser shut off does not reach the sample before the end of the x-ray probe time. For each experiment, there is a 1-2 μm thick aluminum layer between the Fe-15Si sample and LiF window to improve the interface reflectivity for VISAR measurements. Thin (< 1 μm) epoxy layers are used to connect the kapton, forsterite, and LiF.

### Pressure Determination

A line imaging velocity interferometry (VISAR) was used to monitor the particle velocity at the interface between the Fe-15Si sample and LiF window (Celliers et al., 2013). The interferometer records the fringe shift of reflected coherent light to an accuracy of ±5%. The ambiguity in velocity due to integer fringe shifts is resolved using two channels with different velocity sensitivities. The apparent particle velocity (averaged over the 300 μm field of view) was converted to the true interface velocity using the measured index of refraction for LiF (Rigg et al., 2014). The pressure in the shock state was determined through the standard impedance matching technique using the known Hugoniot of LiF and Fe-15Si and the interface velocity recorded by VISAR (Raizer 2002; Rigg et al., 2014; Barker and Hollenbach, 1972). The linear Hugoniot parameters ( $U_S = 5.0(3) + 1.37(7)u_p$ ) for Fe-15Si were interpolated from a power law fit to the available iron silicide data at varying silicon compositions as shown in Figure 4.4 (Marsh, 1980; Matassov, 1977; Funtikov, 2007; Balchan and Cowan, 1966; Kormer and Funtikov, 1965). The power law fit to the data between 2.5 and 25 wt% is found to be:

$$C \text{ (km s}^{-1}\text{)} = 2.880w^{0.205} \quad (4.1)$$

$$S = 2.064w^{-0.152}, \quad (4.2)$$

$$\rho_0 \text{ (g cm}^{-3}\text{)} = -0.324w^{1.116} + 7.784 \text{ g cm}^{-3}, \quad (4.3)$$

where  $C$  and  $S$  are the linear  $U_s - u_p$  Hugoniot parameters,  $\rho_0$  is the ambient density, and  $w$  is the silicon composition in weight percent. The mean of the residual sum of squares for the power law fit to the  $C$  and  $S$  data is  $0.02 \text{ km}^2 \text{ s}^{-2}$  and  $0.01$  respectively, indicating an uncertainty of roughly 5%.

The uncertainty in the shock pressure was determined by propagation of the measurement errors through the impedance match calculation. Contributions to the uncertainty in pressure include the 5% error in VISAR phase measurement, the temporal variance in interface velocity due to wave unsteadiness, and a  $1-\sigma$  uncertainty in the LiF and Fe-15Si Hugoniot parameters and ambient density.

### **In Situ x-ray Diffraction**

Powder x-ray diffraction is used to probe the crystal structure and melt transition of shocked Fe-15Si. Diffraction in the shock-compressed state is recorded using the Powder X-Ray Diffraction with Image Plates (PXRDIIP) diagnostic (Rygg et al., 2012). While the sample is compressed, illumination of an Fe or Cu foil generates quasi-monochromatic  $\text{He}_\alpha$  x-rays at 6.685 keV (Fe foil) or 8.38 keV (Cu foil) with bandwidths of 2%. For experiments conducted on EP, x-rays of  $\sim 1$  ns duration were generated by focusing 1 beam with 900 J onto a  $200 \mu\text{m}$  diameter spot on a  $2 \text{ mm} \times 2 \text{ mm} \times 12.5 \mu\text{m}$  Cu or Fe foil. For experiments conducted on Omega, x-rays of  $\sim 0.5$  ns duration were generated by focusing 16 beams with 125 J per beam onto a  $400 \mu\text{m}$  diameter spot on a  $2 \text{ mm} \times 2 \text{ mm} \times 12.5 \mu\text{m}$  Fe foil. The emitted x-rays pass through the target stack, and the scattered x-rays are collected on image plates which line a  $5 \times 5 \times 7.5 \text{ cm}^3$  box surrounding the sample as illustrated in Figure 4.3. Satellite peaks including  $\text{He}_\beta$  and  $\text{He}_\gamma$  and x-rays generated by the plasma background are suppressed by  $12.5 \mu\text{m}$  thick Fe or Cu filters and  $25 \mu\text{m}$  thick kapton filters which cover each image plate.

The raw and processed data from representative experiments are shown in Figures 4.5 and 4.6 respectively. On the raw image plates, the diffraction peaks from the W pinhole appear warped due to the geometry of the detector, as the intersection of the diffraction cones scattered by the pinhole and the planes of the side of the box is a conic section. Using the known diffraction angles for W and the nominal geometry of the detector, the diffraction data is de-warped from its raw spatial coordinates into the more appropriate diffraction coordinates,  $\phi$  versus  $2\theta$ , where  $2\theta$  is the scattering angle and  $\phi$  is the azimuthal angle about the incident X-ray beam.

In these coordinates, powder-like diffraction peaks project onto lines of constant  $2\theta$ . Since the shocked portion of the Fe-15Si sample is spatially offset from the tungsten by the thickness of the pinhole, the LiF window, and the unshocked Fe-15Si, diffraction from the shocked Fe-15Si will appear systematically shifted to lower  $2\theta$ . To correct this systematic error, the  $2\theta$  angle is re-calculated using the known offset between the sample and the pinhole.

The dominant source of error in  $2\theta$  is the uncertainty in the location along the pinhole from which diffraction is occurring. This uncertainty is quantified using the observed Bragg rings from the un-shocked 1  $\mu\text{m}$  Al layer which is just upstream of the Fe-15Si sample. By comparing the observed Al diffraction to the theoretical diffraction from Al, we find that the centroid of a  $2\theta$  diffraction peak can be resolved with a precision of  $\pm 0.1^\circ$ . The features observed on the image plates are attributed to diffraction from the sample, pinhole, or single-crystal-like reflections from the LiF window. The diffraction angles,  $2\theta$ , for the shocked sample were determined by Gaussian fit to a lineout of the de-warped image plate data.

Density gradients in the sample induced by wave unsteadiness may contribute to broadening of the sample diffraction peaks. To quantify the effect of unsteadiness in the wave profile, we simulated the experiment using the radiation hydrodynamics code HYADES (Larsen and Lane, 1994). The pressure distribution in the sample that is generated as a result of wave unsteadiness amounts to  $\pm 2\%$  variation in density. Density gradients of this magnitude introduce negligible peak broadening relative to the instrument broadening from the finite pinhole aperture and the energy bandwidth of the x-ray source.

### 4.3 Results

We observed two distinct Hugoniot regimes: textured crystalline solid to 282(24) GPa and shock melting at 313(29) GPa and above. Up to 282(24) GPa, we observe diffraction consistent with an ordered cubic structure (either *B2* or *D03*) and an hcp structure.

A characteristic diffraction pattern for a shot in the solid phase is shown in Figure 4.5 and a plot of the d-spacing as a function of pressure for all shots shocked into the solid state is shown in Figure 4.7. Due to the texture of the sample, absence of an expected diffraction peak does not rule out a crystal structure, as the crystal may simply be rotated out of the diffraction condition. Therefore, absence of the diffraction peaks that distinguish *D03* from *B2* due to different ordering of silicon

atoms on *bcc* lattice sites cannot be used to determine the structure. Furthermore, the peaks which differentiate between the *D03* and *B2* structures have low intensity and are difficult to detect in these experiments. While we cannot determine if the structure is *D03* versus *B2*, the presence of the  $(010)_{\text{cubic}}$  diffraction peak implies an ordering of the silicon atoms as the  $(010)$  family of peaks is absent in disordered body centered cubic structures due to destructive interference. Since we cannot distinguish the order of the structure on the basis of our diffraction data, we will simply refer to the structure as *bcc*.

At 282(24) GPa we observe a weak diffuse liquid scattering signature in coexistence with the textured solid diffraction indicating incipient melt on the Hugoniot. At 313(29) GPa we observe complete melting indicated in the diffraction data by the loss of intense sharp diffraction associated with the crystalline order of a solid and the onset of diffuse liquid scattering, as well as the complete loss of texture associated with crystallographic orientation. This bounds complete melting between 282(24) GPa and 313(29) GPa on the Hugoniot. The progression from solid to molten can be seen by comparing the diffraction data shown in Figures 4.5 and 4.6.

The temperature on the Hugoniot is calculated using a model of the heat capacity and 3rd order Birch-Murnaghan equation of state to approximate the principal isentrope (Fischer, Campbell, Caracas, Reaman, Dera, et al., 2012). A Debye model is used as an upper limit to the heat capacity and a model of the electronic contribution to the heat capacity acts as a lower limit (Brown and McQueen, 1986). Error bars for the temperature calculation were estimated based on uncertainties in the equation of state model parameters (Fischer, Campbell, Caracas, Reaman, Dera, et al., 2012). The latent heat associated with the observed phase change from the ambient structure to the *hcp* structure is not included in the calculation. The latent heat of melting is taken to be equivalent to pure iron (Ma et al., 2004).

## 4.4 Discussion

### Texture Relationship

While the measured Bragg angles are consistent with the equilibrium *B2* and iron rich *hcp* phase assemblage, the observed texture allows alternative interpretations. The texture of the shocked sample suggests a microstructure with large grains or alternatively a preferred orientation. While we do not have enough data to fully constrain the orientation relationship between the *bcc* and *hcp* structures (which has three free parameters), we can calculate the angle between the  $(011)_{\text{bcc}}$  and

$(011)_{hcp}$  planes from the observed Bragg angles and the difference in azimuthal angles. Across four observations we determine the angle between the observed diffraction planes is  $4(2)^\circ$ , indicating that the planes are nearly parallel (Table 4.2). This observation is consistent with Burgers correspondence for the *bcc* to *hcp* transformation (Srivastava, Banerjee, and Ranganathan, 2004). The principal of minimum atomic displacement would have a  $\{001\}_{bcc}$  plane (plane of maximum atomic density) parallel to the  $(001)_{hcp}$  close packed plane and the close packed  $[1\bar{1}1]_{bcc}$  and  $[\bar{1}11]_{bcc}$  directions parallel to close packed  $\langle 110 \rangle_{hcp}$  directions. This principal constrains the orientation relationship so that one of the  $\{001\}_{bcc}$  planes not parallel to  $(001)_{hcp}$  will be parallel to a plane in the  $\langle 011 \rangle_{hcp}$  family (Srivastava, Banerjee, and Ranganathan, 2004).

We consider four potential alternative interpretations for the simultaneous observation of textured *bcc* and *hcp* peaks. First, the coexistence of *bcc* and *hcp* structures may be due to spacial inhomogeneity in silicon composition, with areas of low silicon concentration favoring the *hcp* phase and areas of high concentration favoring the *bcc* phase. This interpretation is not favored as EDS maps of the surface composition of a characteristic sample demonstrate compositional inhomogeneity of at most  $\pm 0.15$  weight percent silicon throughout an area on the order of the pinhole aperture.

The coexistence of *bcc* and *hcp* structures and the observed orientation relationship may be due to volume diffusion of silicon in the *bcc* lattice which nucleates areas of low silicon concentration. These areas of low silicon concentration then transform to an *hcp* structure through a martensitic process. This interpretation would require growth of (at minimum) nanometer sized grains on nanosecond timescales implying volume diffusivities on the order of  $10^{-6} \text{ m}^2 \text{ s}^{-1}$ . Therefore, diffusion limited growth would require a diffusivity that is considerably larger than characteristic diffusivities within iron alloys of  $10^{-13} \text{ m}^2 \text{ s}^{-1}$  at these temperatures (Yunker and Van Orman, 2007), but can be consistent with the observed phases and texture.

The observation of an orientation relationship between the *bcc* and *hcp* structures may be explained as a single component phase change where the parent phase is underdriven. This interpretation would imply that the material immediately downstream of the shock front is the *bcc* structure corresponding to compression of the ambient phase. Farther downstream, the material is *hcp* corresponding to the time required for the change of phase to occur. This interpretation is not completely satisfying as the parent phase remains underdriven across the entire pressure range

that we observed, whereas one would expect the kinetics for the transformation to speed up and the parent phase to eventually be overdriven at higher pressures.

Alternatively, the observation of diffraction peaks at nearly the same azimuthal angle may be due to both  $Ly_\alpha$  and  $He_\alpha$  diffraction from the same crystal plane. Due to the texture of the shocked sample, the relative number of  $He_\alpha$  versus higher energy photons cannot be used as an argument to constrain the ionization energy from which diffraction is occurring. It follows that the peak previously indexed as  $He_\alpha$  diffraction from the (011) *bcc* plane may instead be  $Ly_\alpha$  diffraction from the (011) *hcp* plane as shown in Figure 4.8. This explanation, however, does not fully explain the data set. In shot 22562 and 22564 we observe textured diffraction peaks consistent with  $Ly_\alpha$  diffraction from the (011) *hcp* plane with no evidence of the corresponding  $He_\alpha$  peak or any of the other *hcp* peaks. Furthermore, we do not observe  $Ly_\alpha$  diffraction from the (010) or (002) *hcp* planes in any shots. Both of these observations suggest diffraction from a *bcc* structure and not  $Ly_\alpha$  diffraction from the (011) *hcp* plane.

### **Hugoniot Melting**

Incipient melting observed at 282(24) GPa appears to correspond to melting point depression relative to the melting temperature of pure iron which is expected due to entropy of mixing. However, larger uncertainties in the heat capacity contribute to large uncertainties in the estimated shock temperature which do not allow us to estimate the impact of silicon on melt. We do not observe incongruent melting of the *hcp* and *bcc* phases as we observe both crystal structures in the diffraction pattern at the highest pressure where we observed solid diffraction (Figure 4.5) and neither structure in the diffraction pattern at the lowest pressure where we observed significant liquid diffuse scattering (Figure 4.6). This observation supports but does not confirm the interpretation of the solid diffraction data that we have a martensitic transformation from the compressed ambient structure to *hcp* (single component system) and not phase segregation (multicomponent system) since incongruent melting may occur over a smaller pressure window than resolved in this set of experiments.

### **4.5 Conclusions**

The kinetic limitations imposed by the experiment timescale give important insight into the approach to equilibrium for materials that undergo chemical decomposition. While deformation pathways to lower energy single component phases are available on short timescales, the timescale required for equilibrium may be governed by

the self-diffusion of silicon in the *D03* lattice. Future experiments are needed to resolve the ambiguity in the interpretation of the solid diffraction data. This is critical to understanding whether Fe-15Si acts like a single component material due to kinetics associated with the timescale of the experiment or whether we observe chemical segregation, which would indicate a silicon diffusivity considerably larger than expected.

The following suite of experiments would help to understand the kinetic processes that could potentially occur for this material on dynamic compression timescales. Diffraction experiments on a finely grained poly-crystal may help to distinguish the *D03* versus *B2* structures through observation of the higher order diffraction peaks. This technique is limited, however, in that it relies on the absence of a diffraction peak to signify the presence of phase segregation. Shock recovery experiments analogous to the laser heated diamond anvil cell recovery experiments may also be used to look for compositional variations upon recovery which would suggest phase segregation in the shock state (Lin, Heinz, et al., 2002). The need to determine the local order of the phase or phase assemblage makes this material a prime candidate for Extended X-ray Absorption Fine Structure (EXAFS) studies. Successful proof of concept dynamic compression experiments have been done on pure iron, so study of this more complicated system is a logical next step for the diagnostic (Torchio et al., 2016). Diffraction experiments conducted on a plate impact facility such as the Dynamic Compression Sector would also provide valuable insight into the approach to equilibrium for this material by comparing results across multiple timescales.

Shot	Energy (J)	$u_{\text{interface}}$ ( $\text{km s}^{-1}$ )	P (GPa)	bcc (011)	hcp (010)	hcp (002)	hcp (011)
22561 EP	741.1	3.56(18)	166(14)	-	-	1.809	1.709
22562 EP	968.6	3.89(20)	189(15)	1.760	-	-	-
22564 EP	1397.2	4.57(23)	241(20)	1.727	-	-	-
22566 EP	996.2	3.93(20)	192(16)	1.757	-	1.794	-
81661 $\Omega$	70.3	3.95(20)	193(16)	-	-	1.799	-
81663 $\Omega$	99.8	4.59(23)	243(20)	1.721	1.896	1.789	1.671
81664 $\Omega$	107.2	5.06(26)	282(24)	1.700	1.870	1.756	1.658
81666 $\Omega$	153.0	5.64(30)	335(29)	-	-	-	-
81668 $\Omega$	129.8	5.40(30)	313(29)	-	-	-	-

Table 4.1: **Summary of experimental data.** Tabulation of the laser drive energy, measured interface velocity from VISAR, the shock pressure from the impedance match calculation, and observed d-spacing for experiments on the omega extended pulse laser (EP) and the omega 60 beam laser ( $\omega$ ). The uncertainty in the interface velocity includes 5% uncertainty in VISAR phase as well as the uncertainty associated with wave unsteadiness. D-spacings are determined by Gaussian fit to lineouts of the de-warped image plates. Each peak was assigned to a crystal plane in either the *bcc* or *hcp* structure. Due to the texture of the sample, absence of a diffraction peak is not evidence for absence of the structure. The dominant source of error in the d-spacing is the uncertainty in the location along the pinhole from where the diffraction is occurring. This introduces an error of roughly  $0.1^\circ$  in the  $2\theta$  diffraction angle, which we use as our reported error (Rygg et al., 2012).

Shot	$(011)_{bcc}$		$(011)_{hcp}$		$\angle(011)_{bcc}, (011)_{hcp}$ ( $^{\circ}$ )
	$2\theta$ ( $^{\circ}$ )	$\phi$ ( $^{\circ}$ )	$2\theta$ ( $^{\circ}$ )	$\phi$ ( $^{\circ}$ )	
81663	65.979	-58.919	67.407	-64.324	4.7(2.0)
81663	64.805	42.703	66.366	46.306	3.5(2.0)
81663	64.935	-19.64	67.668	-13.514	5.4(2.0)
81664	65.846	-31.532	68.448	-33.694	3.6(2.0)

Table 4.2: **Orientation relationship for *bcc* and *hcp* structures.** Tabulation of the textured diffraction data that indicates an orientation relationship between the *bcc* and *hcp* phases. Columns 2 and 3 denote the polar and azimuthal angles where diffraction from the  $(011)_{bcc}$  crystal plane was observed. Columns 4 and 5 denote the polar and azimuthal angles where diffraction from the  $(011)_{hcp}$  crystal plane was observed. Column 5 tabulates the calculated angle between the  $(011)_{bcc}$  and  $(011)_{hcp}$  crystal planes implied by the observed diffraction angles. The planes are nearly parallel, consistent with Burgers correspondence between *bcc* and *hcp* structures.

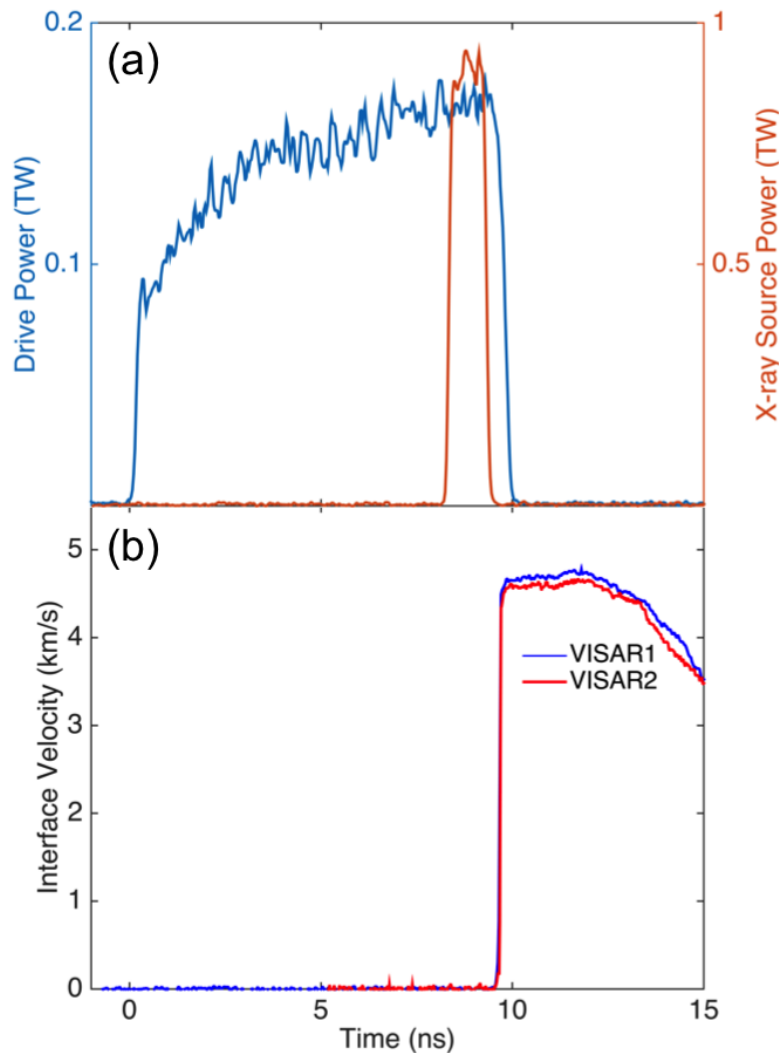


Figure 4.1: **Timing of shock compression experiment.** Panel (a) shows a characteristic EP laser pulse shape from shot 22564 for the beam that drives the sample (left axis) and EP laser pulse shape for the beam which illuminates the Cu or Fe foil used as an x-ray source (right axis). The ramping of intensity in the laser drive pulse shape compensates for adiabatic cooling due to expansion of the plasma plume which would otherwise generate a decaying shock. Panel (b) shows a characteristic VISAR trace from shot 22564 for shock compression experiments. The wave velocity following shock breakout is used in the impedance match calculation to determine the shock pressure in the sample. The decrease in particle velocity at 12 ns is due to the laser shut off. The difference in velocity observed in VISAR 1 and VISAR 2 is consistent with the assumed phase uncertainty of 5%. The x-ray source laser (panel (a)) turns off prior to the shock releasing into the LiF (panel (b)) at 10 ns so that release states are not probed by x-rays.

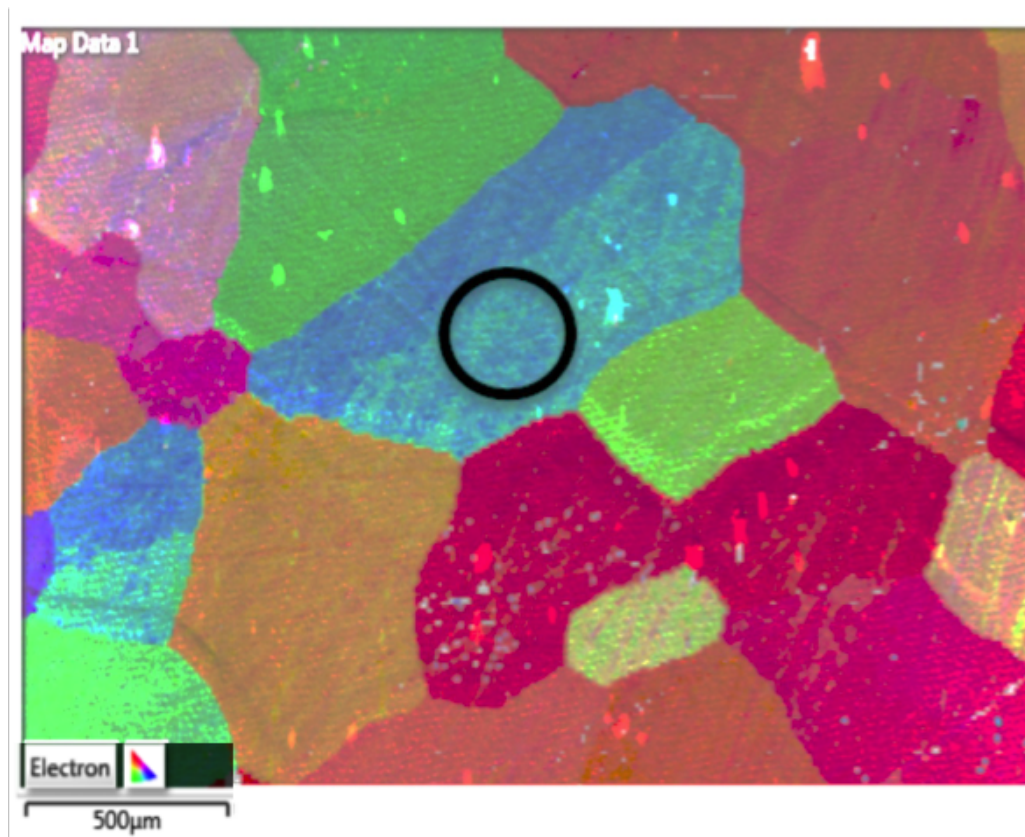


Figure 4.2: **Electron Backscatter Diffraction (EBSD) characterization of the Fe-15Si starting material.** Grain map of a characteristic Fe-15Si sample indicating a grain size on the order of 500  $\mu\text{m}$ . The 300  $\mu\text{m}$  pinhole aperture is shown as a black circle (in an arbitrary location) for relative scale which indicates that the sample is highly textured under the pinhole aperture.

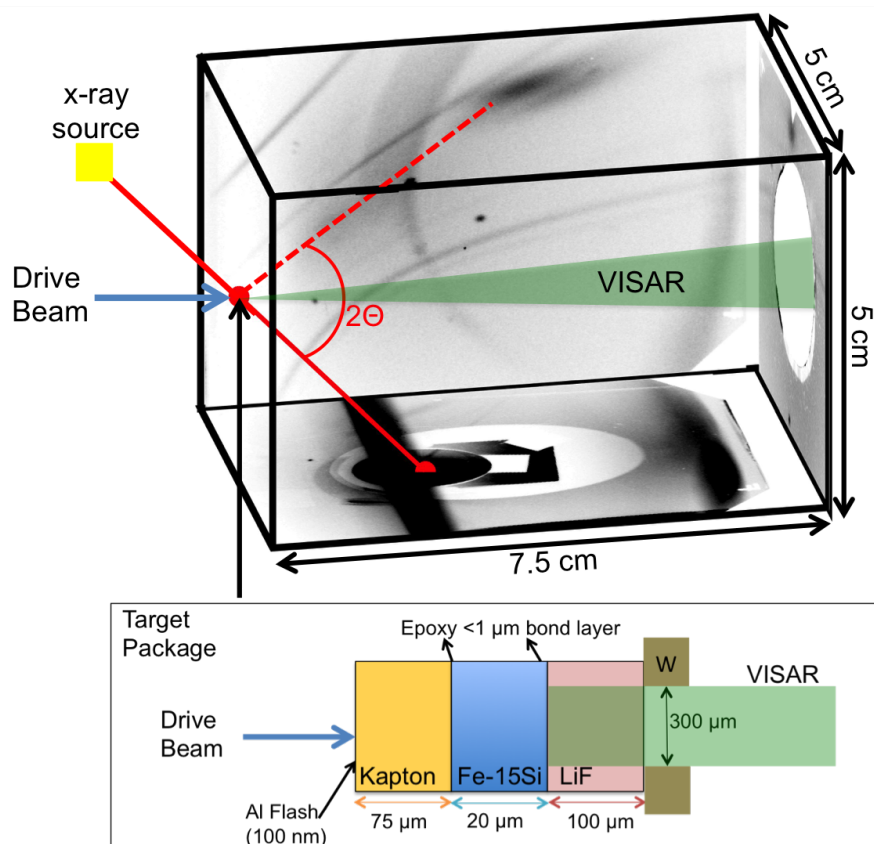


Figure 4.3: **Experimental setup and target geometry.** Top: Schematic diagram of the diffraction detector (PXRDIIP box) where x-rays are detected on image plates that line five sides of a  $5 \times 5 \times 7.5 \text{ cm}^3$  box. Solid red lines show the direct beam x-ray path and the dashed red line shows schematically the path of reflected x-rays from the shocked sample. The path of the VISAR laser is down range of the sample. Bottom: Schematic diagram of the target package consisting of an Fe-15Si foil sandwiched between a kapton ablator and LiF window held together by a thin (< 1  $\mu\text{m}$  thick) layer of epoxy. The VISAR is incident upon the Fe-15Si/LiF interface. A 150  $\mu\text{m}$  thick W pinhole with 300  $\mu\text{m}$  diameter aperture is used to collimate the x-rays and calibrate the detector geometry.

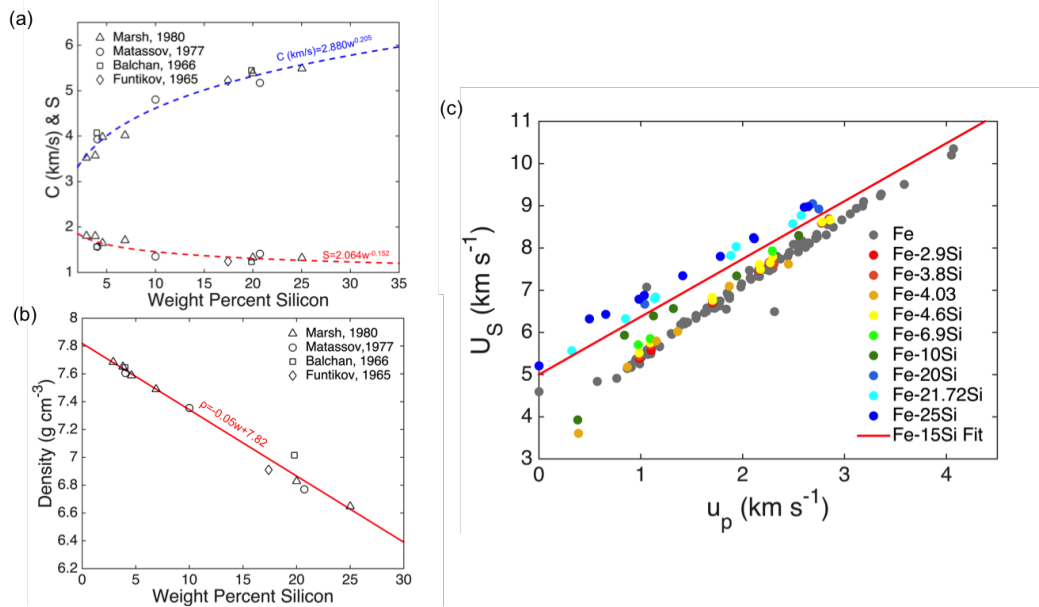


Figure 4.4: **Iron Silicide Hugoniot Parameters.** Top: power law fit to the linear Hugoniot parameters ( $C$  and  $S$ ) as a function of composition in weight percent. The fit was used to determine the Hugoniot parameters for iron silicide at 15 weight percent silicon. We assumed a 5% uncertainty in the fit parameters determined from the mean residual squared error of the power law fit. Bottom: linear fit to the ambient density as a function of composition in weight percent. The density measured in this work (plotted as an asterisk) shows good agreement to the power law fit to available data.

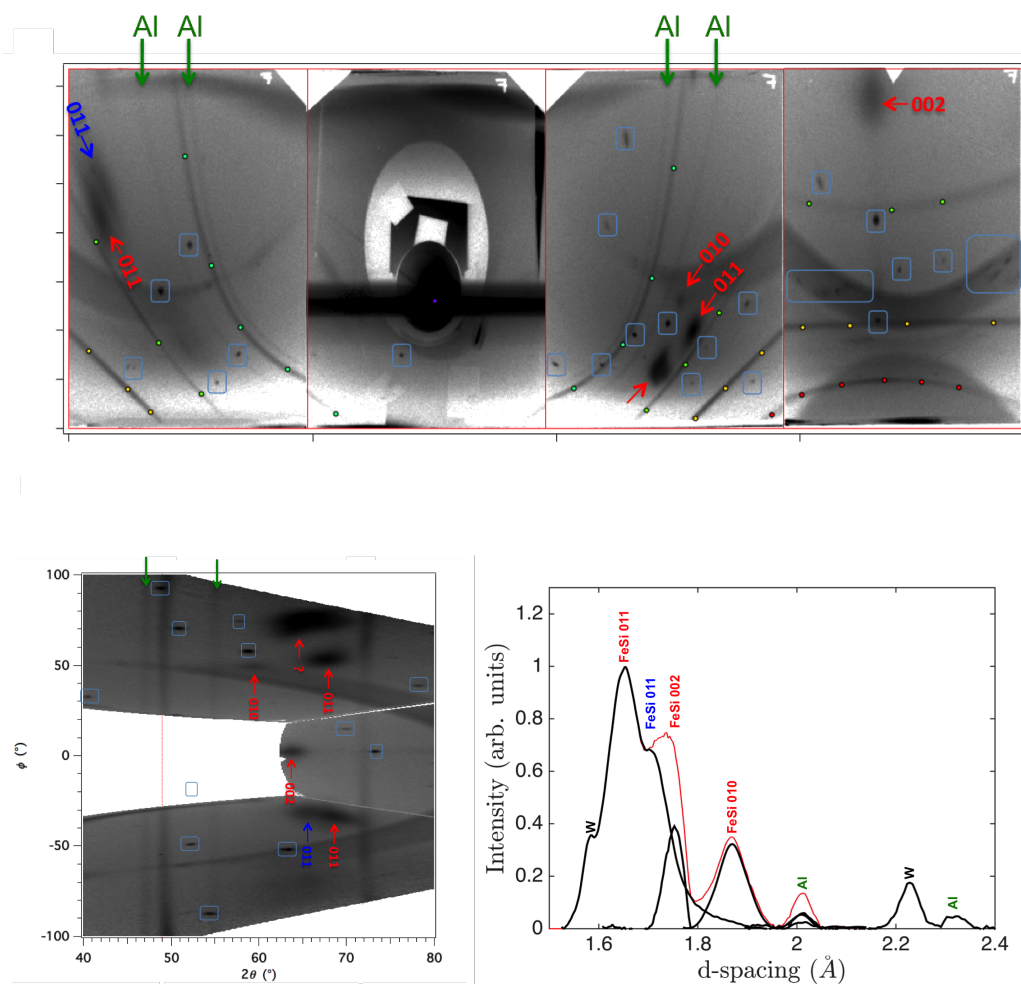


Figure 4.5: **X-ray diffraction patterns for solid samples.** Characteristic x-ray diffraction data for samples shocked into the solid Hugoniot regime. Each peak is attributed to either diffraction from the sample, W pinhole, Al layer, or LiF single-crystal like peaks. Top: Raw diffraction data for shot 81664. The peaks assigned to the *hcp* and *bcc* structures are indicated in red and blue respectively. The curves labeled with green, yellow, and red points correspond to powder diffraction from the W pinhole used to calibrate the detector geometry and de-warp the image into  $2\theta - \phi$  space. The diffraction signatures encircled in cyan come from LiF single-crystal like diffraction and indicated in green come from polycrystalline Al. Left: De-warped image plates. Right: Composite lineout showing the integrated  $\phi$  data as a function of d-spacing. The black correspond to individual lineouts taken over each individual diffraction peak and the red curve corresponds to the summation of each curve.

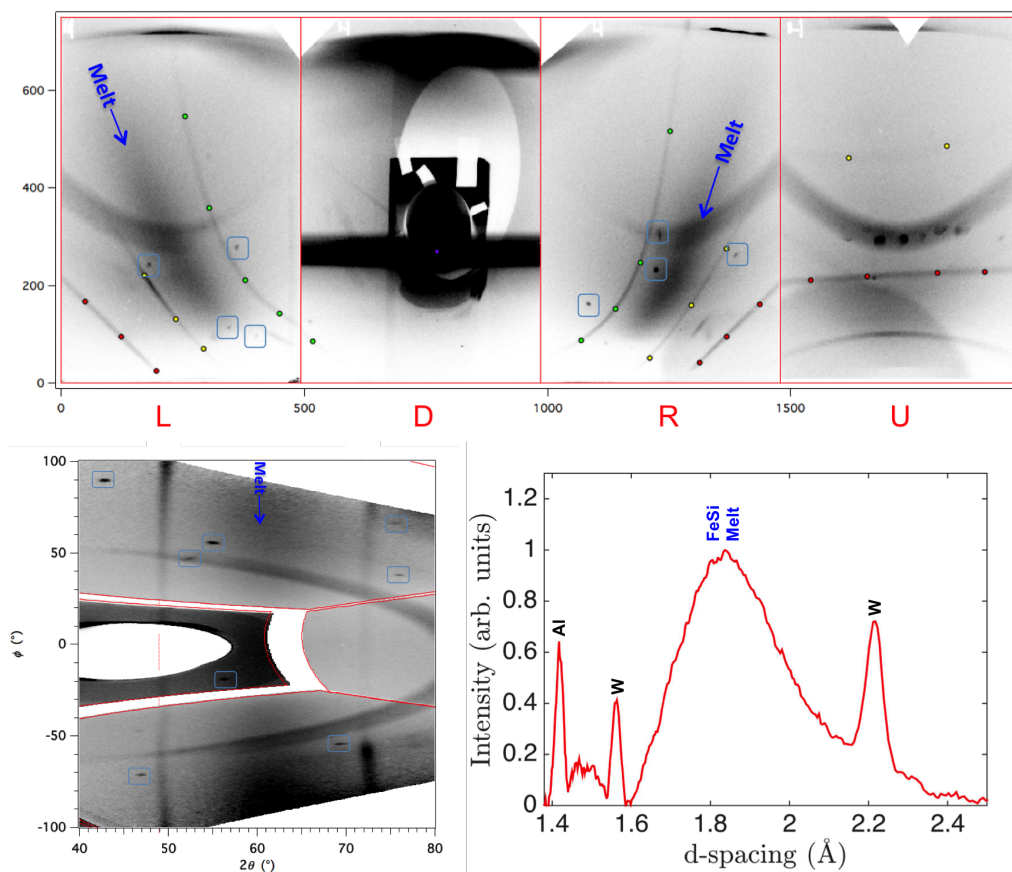


Figure 4.6: **X-ray Diffraction patterns for molten samples.** At 313(29) GPa we observe shock melting indicated by the loss of texture associated with crystallographic orientation and the onset of liquid diffuse scattering indicated in blue on the diffraction panels and lineout. Top: Raw diffraction data where the peaks encircled in cyan correspond to single crystal diffraction from the LiF window, the intense powder peaks correspond to diffraction from the W pinhole, and the diffuse signature corresponds to diffraction from the molten Fe-15Si.

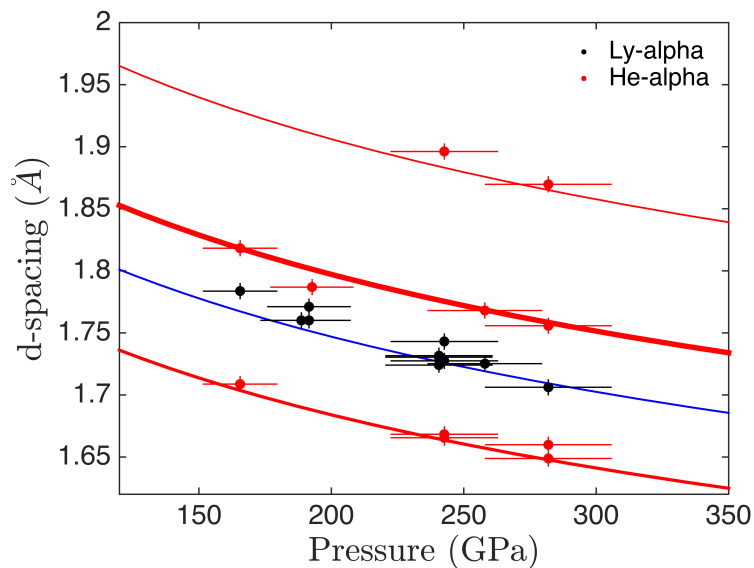


Figure 4.7: **d-spacing versus pressure** Observed d-spacing versus pressure are plotted against their theoretical values for *hcp* with an ideal *c/a* ratio and ordered cubic structures at the Fe-15Si Hugoniot density. Relative expected peak intensities are indicated by line width. The in situ x-ray diffraction data are consistent with a cubic (plotted in black) and *hcp* (plotted in red) structure in coexistence from 166(14) GPa to 282(24) GPa.

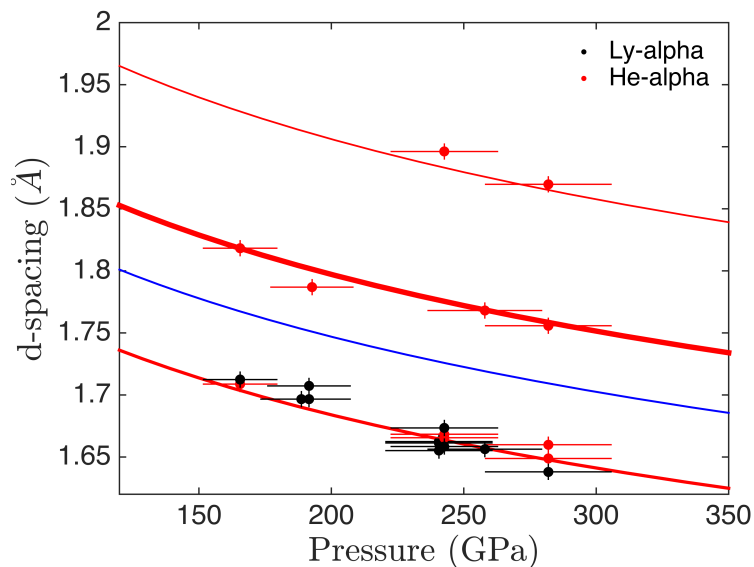


Figure 4.8: **d-spacing versus pressure for  $\text{Ly}_\alpha$  and  $\text{He}_\alpha$  energies** Observed d-spacing versus pressure assuming that peaks previously indexed as *bcc* are actually  $\text{Ly}_\alpha$  diffraction from the  $(011)_{hcp}$  plane.

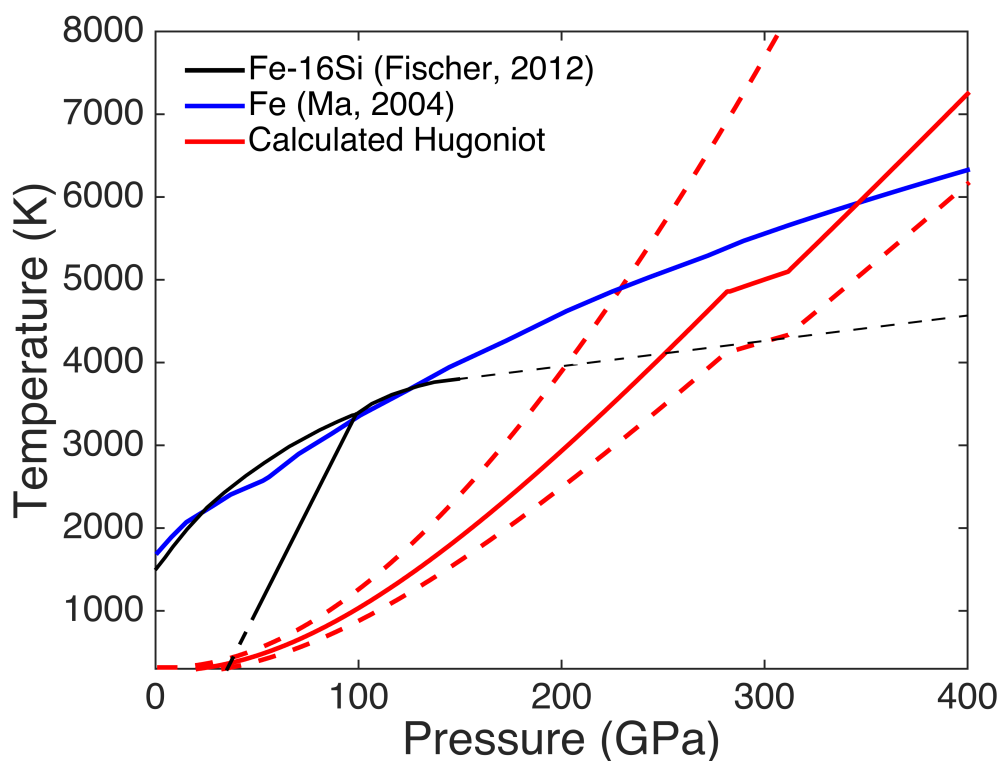


Figure 4.9: **Calculated Hugoniot temperatures for Fe-15Si.** Hugoniot temperatures for Fe-15Si calculated using a 3rd order Birch-Murnaghan equation of state and Debye and electronic model of the heat capacity (Fischer, Campbell, Caracas, Reaman, Heinz, et al., 2014; Brown and McQueen, 1986). The highest pressure where we observe solid diffraction and the lowest pressure where we observe only liquid scattering are 282(24) GPa and 313(29) GPa respectively. The upper bound corresponds to the limit where there is no latent heat associated with melting and no electronic contribution to the heat capacity. The lower bound includes a latent heat and electronic heat capacity taken to be equivalent to pure iron. We find that incipient melting observed at 282(24) GPa corresponds to melting point depression relative to the melting temperature of pure iron, which is expected due to entropy of mixing (Ma et al., 2004). The melt boundary from literature for Fe-16Si is plotted in solid black and extrapolation of the data to higher pressure is plotted as a dashed black line.

## References

- Asanuma, H., E. Ohtani, T. Sakai, H. Terasaki, S. Kamada, N. Hirao, et al. (2011). “Static compression of Fe 0.83 Ni 0.09 Si 0.08 alloy to 374 GPa and Fe 0.93 Si 0.07 alloy to 252 GPa: Implications for the Earth’s inner core”. In: *Earth and Planetary Science Letters* 310.1, pp. 113–118.
- Asanuma, H., E. Ohtani, T. Sakai, H. Terasaki, S. Kamada, T. Kondo, et al. (2010). “Melting of iron–silicon alloy up to the core–mantle boundary pressure: implications to the thermal structure of the Earth’s core”. In: *Physics and Chemistry of Minerals* 37.6, pp. 353–359.
- Asanuma, H., E. Ohtani, T. Sakai, H. Terasaki, S. Kamada, et al. (2008). “Phase relations of Fe–Si alloy up to core conditions: Implications for the Earth inner core”. In: *Geophysical Research Letters* 35.12.
- Balchan, A. and G. Cowan (1966). “Shock compression of two iron-silicon alloys to 2.7 megabars”. In: *Journal of Geophysical Research* 71.14, pp. 3577–3588.
- Balluffi, Robert W, Sam Allen, and W Craig Carter (2005). *Kinetics of materials*. John Wiley & Sons.
- Barker, L. and R. Hollenbach (1972). “Laser interferometer for measuring high velocities of any reflecting surface”. In: *Journal of Applied Physics* 43.11, pp. 4669–4675.
- Bhadeshia, HKDH (2001). “Geometry of crystals”. In: *Institute of Materials, London*.
- Birch, F. (1952). “Elasticity and constitution of the Earth’s interior”. In: *Journal of Geophysical Research* 37, pp. 227–286.
- (1964). “Density and composition of mantle and core”. In: *Journal of geophysical research* 69.20, pp. 4377–4388.
- Brown, M. and R. McQueen (1986). “Phase transitions, Grüneisen parameter, and elasticity for shocked iron between 77 GPa and 400 GPa”. In: *Journal of Geophysical Research: Solid Earth* 91.B7, pp. 7485–7494.
- Celliers, P. et al. (2013). “Line-imaging Velocimetry for Shock Diagnostics (VISAR)”. In: *CLEO: Applications and Technology*. Optical Society of America, ATu3M–2.
- Duffy, T. (2005). “Synchrotron facilities and the study of the Earth’s deep interior”. In: *Reports on Progress in Physics* 68.8, p. 1811.
- Fischer, R., A. Campbell, R. Caracas, D. Reaman, P. Dera, et al. (2012). “Equation of state and phase diagram of Fe–16Si alloy as a candidate component of Earth’s core”. In: *Earth and Planetary Science Letters* 357, pp. 268–276.
- Fischer, R., A. Campbell, R. Caracas, D. Reaman, D. Heinz, et al. (2014). “Equations of state in the Fe–FeSi system at high pressures and temperatures”. In: *Journal of Geophysical Research: Solid Earth* 119.4, pp. 2810–2827.

- Fischer, R., A. Campbell, D. Reaman, et al. (2013). “Phase relations in the Fe–FeSi system at high pressures and temperatures”. In: *Earth and Planetary Science Letters* 373, pp. 54–64.
- Funtikov, A. (2007). “Shock compression of iron-silicon alloys with reference to the possible concentration of silicon in the Earth’s core”. In: *Izvestiya. Physics of the Solid Earth* 43.7, p. 554.
- Gleason, A et al. (2015). “Ultrafast visualization of crystallization and grain growth in shock-compressed SiO<sub>2</sub>”. In: *Nature communications* 6.
- Hawreliak, J et al. (2007). “High pressure nano-crystalline microstructure of shock compressed single crystal iron”. In: *Physical Review B* 78. UCRL-JRNL-237258.
- Hirao, N. et al. (2004). “Equation of state of iron–silicon alloys to megabar pressure”. In: *Physics and chemistry of minerals* 31.6, pp. 329–336.
- Hirose, K., S. Labrosse, and J. Herlund (2013). “Composition and state of the core”. In: *Annual Review of Earth and Planetary Sciences* 41, pp. 657–691.
- Kormer, S. and A. Funtikov (1965). “Shock Compression of Ferrosilicon and the Possible Composition of the Earth’s Core”. In: *Izv. Akad. Nauk SSSR, Fiz. Zemli* 5, p. 1.
- Larsen, J. and S. Lane (1994). “HYADES—A plasma hydrodynamics code for dense plasma studies”. In: *Journal of Quantitative Spectroscopy and Radiative Transfer* 51, pp. 179–186.
- Lin, J.-F., A. Campbell, et al. (2003). “Static compression of iron-silicon alloys: Implications for silicon in the Earth’s core”. In: *Journal of Geophysical Research: Solid Earth* 108.B1.
- Lin, J.-F., D. Heinz, et al. (2002). “Iron-silicon alloy in Earth’s core?” In: *Science* 295.5553, pp. 313–315.
- Ma, Y. et al. (2004). “In situ X-ray diffraction studies of iron to Earth-core conditions”. In: *Physics of the Earth and Planetary Interiors* 143, pp. 455–467.
- Marsh, Stanley P (1980). *LASL shock Hugoniot data*. Vol. 5. Univ of California Press.
- Matassov, G. (1977). *Electrical conductivity of iron–silicon alloys at high pressures and the earth’s core*. Tech. rep. California Univ., Livermore (USA). Lawrence Livermore Lab.
- Morard, G. et al. (2014). “Properties of iron alloys under the Earth’s core conditions”. In: *Comptes Rendus Geoscience* 346.5, pp. 130–139.
- Poirier, J.-P. (1994). “Light elements in the Earth’s outer core: a critical review”. In: *Physics of the earth and planetary interiors* 85.3-4, pp. 319–337.
- Rigg, P. et al. (2014). “Determining the refractive index of shocked [100] lithium fluoride to the limit of transmissibility”. In: *Journal of Applied Physics* 116.

- Rygg, R. et al. (2012). “Powder diffraction from solids in the terapascal regime”. In: *Review of Scientific Instruments* 83.
- Sakai, T. et al. (2011). “Stability field of the hcp-structure for Fe, Fe-Ni, and Fe-Ni-Si alloys up to 3 Mbar”. In: *Geophysical research letters* 38.9.
- Srivastava, D., S. Banerjee, and S. Ranganathan (2004). “The crystallography of the BCC to HCP (orthohexagonal) martensitic transformation in dilute Zr-Nb alloys: Part I: Lattice strain and lattice invariant shear”. In: *Transactions of the Indian Institute of Metals* 57.3, pp. 205–223.
- Swift, D. and G. Kraus (2008). “Properties of plastic ablaters in laser-driven material dynamics experiments”. In: *Physical Review E* 77.6.
- Tateno, S. et al. (2010). “The structure of iron in Earth’s inner core”. In: *Science* 330.6002, pp. 359–361.
- Torchio, R. et al. (2016). “Probing local and electronic structure in Warm Dense Matter: single pulse synchrotron x-ray absorption spectroscopy on shocked Fe”. In: *Scientific reports* 6.
- Yunker, M. and J. Van Orman (2007). “Interdiffusion of solid iron and nickel at high pressure”. In: *Earth and Planetary Science Letters* 254.1, pp. 203–213.
- Zhang, Feiwu and Artem R Oganov (2010). “Iron silicides at pressures of the Earth’s inner core”. In: *Geophysical Research Letters* 37.2.

*Chapter 5*

## CONCLUSIONS AND FUTURE WORK

Shock compression techniques have traditionally been used to measure high temperature and high pressure regions of phase space and the equation of state surface. However, until recently the tools available to probe material properties in the shock state have been limited to a small suite of diagnostics including timing pins to observe shock transit times, velocimetry to observe wave speeds, and pyrometry to observe temperatures (Mosenfelder, Asimow, and Ahrens, 2007; Lyzenga and Ahrens, 1980). Given these diagnostic limitations coupled with the short timescale of dynamic compression platforms, the nature of the state behind the shock front, whether equilibrium or metastable, was uncertain.

To avert these diagnostic limitations researchers have relied upon recovery techniques to look for signatures of the phase or phases present in the shock state (Syono et al., 1981; Jeanloz, 1980). However, these techniques assume that the release process does not eclipse the material response in the shock state. In this thesis, we rely on in situ powder diffraction to subvert these previous diagnostic limitations and directly probe the shock state.

For single component materials, such as pure iron, the material response may proceed rapidly and equilibrium behavior can readily be observed on dynamic compression timescales (J. Nguyen, 2004; Wang et al., 2013). However, to correctly model the interior structure and dynamics of terrestrial planets, geologists are interested in studying multi-component systems (Birch, 1952; Birch, 1964; Asimow, 2017; De Koker, Karki, and Stixrude, 2013). Such systems are complicated by Gibbs' result that the number of compositionally distinct phases that can coexist in equilibrium increases with each chemically-independent constituent of a system. Achieving an equilibrium state from an initially compositionally homogeneous material may be a slow process, rate-limited by ionic diffusion to produce chemically-distinct compounds.

In this thesis we evaluate the approach to equilibrium for two materials that are known to chemically segregate at elevated pressure and temperature: forsterite and iron silicide. In chapter 1, we determined that solid state diffusion in forsterite is insufficient to nucleate and grow the equilibrium phase assemblage of periclase and

perovskite on microsecond timescales. This result bounds the solid state diffusivity of finely grained polycrystalline forsterite below  $1 \text{ nm}^2 \mu\text{s}^{-1}$ . We show that on the microsecond timescale of the experiment, the metastable forsterite III structure observed statically at 300 K and pressures up to 90 GPa remains metastable at the elevated temperatures on the Hugoniot (Finkelstein et al., 2014).

In chapter 2, we showed that chemical separation is possible on nanosecond timescales. In forsterite shocked above 140 GPa, we observe the equilibrium phase assemblage of periclase in coexistence with liquid. This is possible for forsterite due to the topological constraint that the metastable extension of the forsterite melt curve ( $\text{Mg}_2\text{SiO}_4 \text{ (s)} \rightarrow \text{Mg}_2\text{SiO}_4 \text{ (L)}$ ) is cooler than the stable eutectic reaction ( $\text{Pe+Bd} \rightarrow \text{Mg}_2\text{SiO}_4 \text{ (L)}$ ). Extrapolation of the melt curves to the pressure range of interest suggests that the following two step reaction is thermodynamically possible:



The second step can occur on the nanosecond timescale of laser driven shock experiments, as the kinetics for nucleation and growth of periclase are driven by the kinetics of the liquid phase. Our result validates the diffusivities of  $\text{Mg}_2\text{SiO}_4$  liquid at high pressure calculated from first principles (De Koker, Stixrude, and Karki, 2008).

For materials with different topology, metastable melting and growth of the equilibrium phase assemblage may not be accessible on the principal Hugoniot. To this end, we developed and tested a novel dynamic compression technique to probe high pressure states in the solid by following pathways to equilibrium that are rate limited by the kinetics of the liquid phase. In these experiments, we used an initial shock wave to melt the sample and a subsequent tailored ramp wave to re-solidify the sample. We were able to observe the equilibrium sub-liquidus phase assemblage and thereby successfully demonstrated the value of this new technique as a worthwhile tool to add to the dynamic compression toolbox.

In chapter 3, we looked at the nanosecond response of iron silicide upon shock compression to pressures between 166(14) GPa and 335(29) GPa. This work bounds the complete Hugoniot melting pressure between 282(24) GPa and 313(29) GPa through direct observation of liquid diffuse scattering and loss of texture in the diffraction pattern.

Different materials provide different challenges, and the results of this campaign were particularly puzzling. We observed both compressed *hcp* and *bcc* structures in the diffraction pattern consistent with the equilibrium phase assemblage. This result would indicate a minimum diffusivity of  $10^{-9} \text{ m}^2 \text{ s}^{-1}$ , 4 orders of magnitude greater than the most reasonable estimates for the solid diffusivity of iron (Yunker and Van Orman, 2007). Furthermore, the phase change induced by the shock appeared to preserve the texture of the starting material, an observation potentially inconsistent with a reconstructive phase transition.

This is an exciting time to be in the dynamic compression field as there is a lot of work to be done. Continued diagnostic development will be necessary to improve our understanding of the nature of the state behind the shock front (especially for materials that chemically segregate). An improved capability to deduce the precise geometry between the sample and detector, particularly on plate impact facilities where the sample may move a significant distance over the microsecond duration of the experiment, will be an important step to reducing the uncertainties in powder diffraction measurements. Furthermore, such advances are critical to being able to index diffraction peaks under Laue diffraction conditions, a worthwhile goal, as it would allow for the utilization of the full spectrum of the x-ray beam and thereby increase the number of useful photons by several orders of magnitude.

## BIBLIOGRAPHY

- Adjaud, O., G. Steinle-Neumann, and S. Jahn (2011). “Transport properties of  $\text{Mg}_2\text{SiO}_4$  liquid at high pressure: Physical state of a magma ocean”. In: *Earth and Planetary Science Letters* 312, pp. 463–470.
- Asimow, P. (2017). “A measure of mantle melting”. In: *Science* 355, pp. 908–909.
- Balchan, A. and G. Cowan (1966). “Shock compression of two iron-silicon alloys to 2.7 megabars”. In: *Journal of Geophysical Research* 71, pp. 3577–3588.
- Birch, F. (1952). “Elasticity and constitution of the Earth’s interior”. In: *Journal of Geophysical Research* 37, pp. 227–286.
- (1964). “Density and composition of mantle and core”. In: *Journal of geophysical research* 69.20, pp. 4377–4388.
- Brown, M., M. Furnish, and D. Boness (1987). “Sound velocities for San Carlos olivine”. In: *Shock Waves in Condensed Matter*, pp. 119–122.
- Brown, M. and R. McQueen (1986). “Phase transitions, Grüneisen parameter, and elasticity for shocked iron between 77 GPa and 400 GPa”. In: *Journal of Geophysical Research: Solid Earth* 91.B7, pp. 7485–7494.
- De Koker, N., B. Karki, and L. Stixrude (2013). “Thermodynamics of the  $\text{MgO-SiO}_2$  liquid system in Earth’s lowermost mantle from first principles”. In: *Earth and Planetary Science Letters* 361, pp. 58–63.
- De Koker, N., L. Stixrude, and B. Karki (2008). “Thermodynamics, structure, dynamics, and freezing of  $\text{Mg}_2\text{SiO}_4$  liquid at high pressure”. In: *Geochimica et Cosmochimica Acta* 72, pp. 1427–1441.
- Finkelstein, G. et al. (2014). “Phase transitions and equation of state of forsterite to 90 GPa from single-crystal X-ray diffraction and molecular modeling”. In: *American Mineralogist* 99.1, pp. 35–43.
- Fischer, R., A. Campbell, R. Caracas, et al. (2014). “Equations of state in the Fe-FeSi system at high pressures and temperatures”. In: *Journal of Geophysical Research: Solid Earth* 119.4, pp. 2810–2827.
- Fischer, R., A. Campbell, D. Reaman, et al. (2013). “Phase relations in the Fe-FeSi system at high pressures and temperatures”. In: *Earth and Planetary Science Letters* 373, pp. 54–64.
- Funtikov, A. (2007). “Shock compression of iron-silicon alloys with reference to the possible concentration of silicon in the Earth’s core”. In: *Physics of the Solid Earth* 43, pp. 554–558.
- Hennig, R. (2005). “Impurities block the  $\alpha$  to  $\omega$  martensitic transformation in titanium”. In: *Nature Materials* 4, pp. 129–133.

- J. Nguyen, et al. (2004). “Specifically prescribed dynamic thermodynamic paths and resolidification experiments”. In: vol. 706. 1. AIP, pp. 1225–1230.
- Jackson, I. and T. Ahrens (1979). “Shock-wave compression of single crystal forsterite”. In: *Journal of Geophysical Research* 84, pp. 3039–3048.
- Jeanloz, R. (1980). “Shock effects in olivine and implications for Hugoniot data”. In: *Journal of Geophysical Research: Solid Earth* 85.B6, pp. 3163–3176.
- Kormer, S. and A. Funtikov (1965). “Shock compression of ferrosilicon and the possible composition of the Earth’s core”. In: *Izv. Akad. Nauk SSSR*.
- Lin, J.-F. (2009). “Phase relations of Fe-Si alloy in Earth’s core”. In: *Geophysical Research Letters* 36, p. L06306.
- Lin, J.-F. et al. (2002). “Iron-silicon alloy in Earth’s core?” In: *Science* 295.5553, pp. 313–315.
- Luo, S.-N and T. Ahrens (2004). “Shock-induced superheating and melting curves of geophysically important minerals”. In: *Physics of the Earth and Planetary Interiors* 143, pp. 369–386.
- Luo, S-N, T. Akins J. and Ahrens, and P. Asimow (2004). “Shock-compressed Mg-SiO<sub>3</sub> glass, enstatite, olivine, and quartz: Optical emission, temperatures, and melting”. In: *Journal of Geophysical Research: Solid Earth* 109.B5.
- Lyzenga, G. and T. Ahrens (1980). “Shock temperature measurements in Mg<sub>2</sub>SiO<sub>4</sub> and SiO<sub>2</sub> at high pressures”. In: *Geophysical Research Letters* 7.2, pp. 141–144.
- Matassov, G. (1977). *Electrical conductivity of iron–silicon alloys at high pressures and the earth’s core*. Tech. rep. California Univ., Livermore (USA). Lawrence Livermore Lab.
- McDonough, W. (2003). “Compositional model for the Earth’s core”. In: *Carlson, R. W. (Ed.), Treatise of Geochemistry* 2, pp. 547–568.
- Mosenfelder, J., P. Asimow, and T. Ahrens (2007). “Thermodynamic properties of Mg<sub>2</sub>SiO<sub>4</sub> liquid at ultra-high pressures from shock measurements to 200 GPa on forsterite and wadsleyite”. In: *Journal of Geophysical Research: Solid Earth* 112.
- Porter, D., K. Easterling, and M. Sherif (2009). *Phase transformations in metals and alloys*. Boca Raton, FL, USA: CRC Press.
- Presnall, D. et al. (1998). “Liquidus phase relations in the system MgO–MgSiO<sub>3</sub> at pressures up to 25 GPa—constraints on crystallization of a molten Hadean mantle”. In: *Physics of the Earth and Planetary Interiors* 107.1, pp. 83–95.
- Solomatov, V. (2007). “Magma oceans and primordial mantle differentiation.” In: *Treatise on Geophysics* 9.
- Syono, Y. et al. (1981). “Dissociation reaction in forsterite under shock compression”. In: *Science* 214.4517, pp. 177–179.

- Wang, J. et al. (2013). “Ramp compression of iron to 273 GPa”. In: *Journal of Applied Physics* 114.2.
- Wett, J. and T. Ahrens (1983). “Shock compression of single-crystal forsterite”. In: *Journal of Geophysical Research: Solid Earth* 88.B11, pp. 9500–9512.
- Yunker, M. and J. Van Orman (2007). “Interdiffusion of solid iron and nickel at high pressure”. In: *Earth and Planetary Science Letters* 254.1, pp. 203–213.